EFFECT OF WEATHER CONDITIONS ON PERFORMANCE OF SOLAR ENERGY SYSTEMS

by

Shadi H. Shehadeh

Submitted in partial fulfilment of the requirements
for the degree of Doctor of Philosophy

at

Dalhousie University
Halifax, Nova Scotia
March 2018

This thesis is dedicated to the memory of my beloved

grandparents

Zuhdi, Ramadan, Fatima and Rabeha

TABLE OF CONTENTS

LIST OF TABLES

LIST OF FIGURES

ABSTRACT

Solar energy is increasingly in demand as a clean, sustainable source of energy without a carbon footprint. This thesis examines the effect of weather conditions on the performance of photovoltaic (PV), photovoltaic thermal (PVT), and thermal solar energy applications. The aim is to maximize the utilized energy, to reduce the costs of energy and emissions. The analysis is conducted by using a dataset of weather conditions in a North American city over a period of one year.

First, the effect of weather conditions on the generation of harmonics in PV systems is investigated. A PV model, including the inverting stage, is considered. Three converter techniques, which form the basis for the majority of converters, are used to validate the proposed approach: A square-wave inverter with 60Hz switching, a square-wave inverter with blanking angle and 60Hz switching, and pulse width modulation (PWM). Probability density functions and probability distribution models are determined as aids for improving the quality of the power generated. The long-term effects of weather conditions on harmonics produced by PV inverters are considered. The results show the variability in the amplitude of each harmonic component, the boundaries of each harmonic component, and which harmonic magnitudes occur more frequently.

Secondly, the effect of weather conditions on the PV cell ratio of a PVT system is analyzed. The maximum overall thermal energy (OTE) and the CO_2 emission reduction of the PVT system is obtained for an entire year. Constant and variable flow rate values are applied in the simulated study for different time spans over a year. To validate the proposed work, three-time span levels are evaluated: A macro level (annual), meso level (seasonal) and micro level (monthly). Simulated models are developed to obtain the appropriate PV coverage area to maximize the OTE.

Thirdly, global solar radiation (GSR) prediction models are proposed which achieve improved performance in terms of error values and structural simplicity. The proposed models are based on the weather conditions of the specific location. Finally, a practical application is developed on the basis of the proposed GSR predictions, which help to maximize the utilized energy.

LIST OF ABBREVIATIONS AND SYMBOLS USED

AC	*Alternating Current*
AI	*Artificial Intelligence*
ANN	*Artificial Neural Network*
CES	*Community Energy Storage*
cc	*Cloud-cover*
CHP	*Combined Heat and Power*
CO_2	*Carbone dioxide*
CSI	*Current Source Inverters*
d	*the day*
D	*Day*
d_s	*Sunshine duration*
DC	*Direct Current*
DIC	*Double Inductor*
DNI	*Direct Normal Irradiation*
DSM	*Demand Side Management*
EMI	*Electro-Magnetic Interference*
FDM	*Fuzzy logic Decision Maker*
FF	*Fill Factor*
FL	*Fuzzy Logic*
GSR	*Global Solar Radiation*
GSR_{1D}	*Daily global solar radiation of the first stage of the second proposed model*
GSR_{1H}	*Hourly global solar radiation of the first stage of the second proposed model*
GSR_D	*Daily global solar radiation*
GSR_H	*Hourly global solar radiation*
GSR_e	*Difference between predicted and measured GSR*
h	*Hour*
HF	*High Frequency*

hu	*Relative humidity*
L_{al}	*Altitude*
L_{la}	*Latitude*
L_{lo}	*Longitude*
LC	*Low Current*
LF	*Low Frequency*
LLI	*Linear Ladder Inverter*
MAPE	*Mean Absolute Percentage Error*
MBE	*Mean Bias Error*
MPE	*Mean Percentage Error*
MPP	*Maximum Power Point*
MPPT	*Maximum Power Point Tracking*
MSE	*Mean Square Error*
NNLI	*Natural Number Ladder Inverter*
nRMSE	*Normalized Root Mean Square Errors*
OTE	*Overall Thermal Energy*
PCBs	*Printed Circuit Boards*
PCU	*Power Conditioning Unit*
PDF	*Probability Density Function*
PV	*Photovoltaic*
PVT	*Photovoltaic Thermal*
PWM	*Pulse Width Modulation*
R	*Pearson Coefficient*
R^2	*Coefficient of determination*
R_{SH},	*Shunt resistance*
R_s	*Series resistance*
SIC	*Single Inductor*
SLNN	*Single -layer Neural Network*
T	*Air temperature*
T_{max}	*Maximum air temperature*
TES	*Thermal Energy Storage*

THD	*Total Harmonic Distortion*
VSI	*Voltage Source Inverters*
w_s	*Wind-speed*
WNN	*Wavelet Neural Network*
ZCS	*Zero Current Switching*
ZCT	*Zero Current Transition*
ZVS	*Zero Voltage Switching*
ZVT	*Zero Voltage Transition*

ACKNOWLEDGEMENTS

My unreserved gratitude and praise are for Allah, the Most Compassionate and the Most Merciful. He has blessed me with his bounties, and he has given me the strength and courage to reach my goals during this journey.

First, I would like to thank my research supervisor, Dr. Mohamed El-Hawary, and my co-supervisor Dr. Hamed Aly, for their guidance, help and support throughout the research for this thesis and associated publications.

I gratefully acknowledge the funding received in support of my PhD from my supervisor Dr. El-Hawary and the Killam Trusts Scholarship.

I wish to thank Dr. William Phillips and Dr. Jason Gu for serving on my supervisory committee, and Dr. Md Azizur Rahman for serving as the external examiner.

I also thank Dr. Timothy Little, Dr. William Phillips Dr. George Jarjoura, and our department secretaries Nicole Smith, Mary Little and Shelly Landry for their help and support during my studies. Also, I would like to thank Mohamed Eldlio for introducing me to the *LyX* document processor, with which this thesis was written.

I would also like to thank Ashraf AbuSharekh, Abidalrahman Mohammad and Dang Anh, post-doctoral research associates, for numerous fruitful discussions and useful suggestions for my work.

Thanks also go to my friends and colleagues, without whom I could not have succeeded in my endeavors, in particular, Dr. Montasir Qasymeh, Omar Qatami, Amar Sharif and Rashaydeh's brothers.

I am also very grateful to all those in the Power group. Bader Alluhaidah especially provided great assistance, spending many late nights in discussions with me to help me organize my thoughts regarding this research.

My deep appreciation goes out to the family who hosted me and welcomed me to Halifax: Colleen Walsh and her children. I would also like to express my thanks to my uncle Medhat Esmat and his family, for their help and support during my life in Halifax.

Special thanks go to my family, especially my brothers, Mohammad and Moath, my sister, Suhad, my uncles and my aunts whom I have missed during the many years of being away from home.

I would especially like to thank the person who has endured the hardship of my absence and has been patient with my constant urgency to complete my work. I express heartfelt, unending gratitude to my wife, Beverly MacDonald, the mother of my children, Mohammad, Abdurrahman and Mariam, for being a pillar of support and for standing firm beside me throughout this journey.

Finally, I would like to express my sincere love and gratitude to my parents, Hazzem and Mariam. Notwithstanding my academic achievements, I owe them more than anyone could possibly imagine. I thank them for their love and infinite care, which has made the person I am today. Words cannot express the gratitude I feel for the nurturing and support that my parents have provided throughout my life. It is my sincere hope that they are as proud of their son as their son is of them.

CHAPTER 1 INTRODUCTION

As a clean source of energy, solar and other types of renewable energy are important for meeting future energy needs, especially in rural areas. Costs associated with the use of solar energy still present a challenge. While photovoltaic (PV) systems comprise one of the most important renewable energy resources in terms of global installed capacity, hybrid photovoltaic thermal (PVT) systems increase system efficiency by using a combination of PV and solar thermal collectors. This work focuses on PV, hybrid PVT and thermal systems as a renewable source of energy. Problems involved with the use of this type of energy include efficiency, power fluctuations, and harmonics. Much research has been directed toward harmonic estimation and power fluctuations, to reduce the impact of these factors. In addition, many studies have been done on maximizing the efficiency of these systems. The present work focuses on weather conditions and their effects on solar energy applications and systems. Because weather conditions are among the most significant factors affecting these issues, this study is important in terms of the overall cost of renewable energy integration, and the quality and security of renewable power systems.

1.1 THESIS OBJECTIVES

The primary objectives of this research are to investigate the effect of weather conditions, mainly temperature and solar radiation, on the generation of harmonics in PV systems, and to examine the PV cell ratio in photovoltaic thermal (PVT) systems to propose models that maximize the utilized energy. Another goal is to introduce solar radiation prediction models which achieve improved performance in terms of error values and structural simplicity compared to the similar works that have been done on this field. The final

objective is to develop a program based on the proposed solar radiation predictions, to assist in maximizing the utilized solar energy.

1.2 THESIS CONTRIBUTION

In this work, the relationship between weather conditions over the long term and the generation of harmonics in PV systems is investigated. Most earlier work has focused on varying either the radiation or the temperature and determining the effect on the maximum power point. This thesis utilizes real data that has different radiation and temperature values in a given time span. It is found that the amplitudes of the fundamental and harmonic components decrease when the radiation decreases, and the temperature increases and verse versa. However, the variation in weather conditions does not affect the ratio of each harmonic to the fundamental components of the output. In addition, probability distribution models are determined for each fundamental and harmonic component of the signal, for the different converting techniques. This study will help to construct a filtering system to mitigate harmonics.

The relationship between weather conditions over a one-year period and the PV cell ratio in PVT systems is studied to help maximize thermal energy, in order to increase savings and reduce emissions. Most previous work has focused on a constant fluid flow rate of the PVT system, different PV coverage areas with discrete, limited percentages (e.g. 25%, 50%, 75% and 100%) and a short time span during the year. The present thesis utilizes real data which contain different values of solar radiation, wind speed, flow rate, temperature of the input water, and temperature of the air, for one year. Furthermore, variable water flow rates and different percentages of PV coverage are used to calculate the monthly and seasonal OTE.

Three Global Solar Radiation (GSR) models are proposed to improve performance and accuracy of the solar prediction. For this study, the data inputs for the GSR prediction model are the ambient temperature, relative humidity, cloud cover, wind speed, time of day in hours (1 to 24), and day of the year (1 to 365). The data were recorded in Halifax, Nova Scotia, Canada, between 2000 and 2005. For this study, hourly and daily GSR (GSR_H and GSR_D) are predicted from the models. cc (cloud cover), hu (relative humidity), and T (air temperature) are found to be the best individual weather variables to use as inputs for both GSR_H and GSR_D prediction. Using maximum GSR_H and GSR_D gives each hour and day at a specific location a distinctive identity, by eliminating the effect of weather variables on GSR. This helps to process the effect of each individual weather variable on GSR. In addition, using maximum GSR helps to decrease the number of weather variables needed for prediction.

Wavelet Neural Network (WNN) is used for GSR error (GSR_e)prediction. A number of mother wavelet functions (Morlet, Mexican Hat (Mexihat), Haar and Gaussian) are used as transfer functions for the hidden layer in the network, for GSR_e prediction.

Moreover, a load management application called SmartSaver, is developed to maximize utilization of the solar boiler system through the scheduling of household activities. This application uses the second proposed model for GSR_H and GSR_D prediction, and is fed the weather variables directly from a weather website. In the first step in developing the application, live weather data are provided from a weather website. In the second step, the GSR_H and GSR_D are predicted for ten days. The cumulative hourly energy is then calculated for ten days. In addition, the cumulative daily energy, and optimal days in the ten-day period are obtained. The next step is to add household activities which consume hot water,

such as dish washers, using the washing machine, and taking a shower or bath. The next step is to find the optimal savings obtainable by scheduling the activity. These results have been published and submitted [1]-[10].

1.3 THESIS OUTLINE

This thesis is organized as follows.

Chapter 2 presents a brief overview of renewable and solar energy and its development history. Chapter 3 provides an overview of PV and PVT systems, including the structure, models and mathematical analyses of the systems. In addition, the modeling, simulation, analysis and discussion of the effect of weather conditions on the PV cell ratio in PVT systems are presented. Chapter 4 briefly reviews solar radiation forecasting via artificial neural networks (ANN) and wavelet neural networks (WNN), and presents applications and structures of ANN and WNN. A literature review of solar radiation prediction and the evaluation of prediction models is also provided. Moreover, new models for global solar radiation (GSR) prediction are introduced and compared with existing ones in the field. Chapter 5 reviews harmonics and their causes and effects, as well as metrics used in the measurement of harmonic levels. A literature review concerning the generation of harmonics in PV systems is also presented. Furthermore, the modeling, simulation, analysis and discussion of the effect of weather conditions on the generation of harmonics is presented. Chapter 6 briefly reviews and defines the concept of load management, and provides a literature review in this field. In addition, a new load management application is presented which could be valuable for maximizing cost savings and reducing emissions through the use of thermal systems. Finally, Chapter 7 presents the conclusions of the research and proposes suggestions for future endeavours in this field.

CHAPTER 2 RENEWABLE AND SOLAR ENERGY

In this chapter, a brief overview of renewable and solar energy is presented [10].

2.1 INTRODUCTION

Since its advent, electricity has become a critically important element of human life, forming the basis for the lifestyle of the modern era. In light of rapid technological advancement, the rise of new technologies, and exponential population growth worldwide, there is an urgent need for enhanced methods of power generation.

Particularly in recent years, global electricity requirements have been the focus of a multitude of studies and high-profile research spanning many fields. Several factors have contributed to the increasing focus on worldwide energy consumption needs. One of the most striking is the environmental damage which has occurred and continues to occur from the burning of hydrocarbon fossil fuels. Although debated, the concept of global warming as a threat to humanity has served to spur interest in examining our current energy consumption patterns and energy sources, with the aim of finding more efficient and sustainable alternatives. Significant instability in regions of the world that are largely responsible for the production and export of crude oil, a basic staple of fossil fuel energy, has caused concern, especially in conjunction with the deepening worldwide energy crisis [11].

2.2 RENEWABLE ENERGY

A combination of environmental awareness, evolving economic and foreign policies, and public opinion on such issues has led world's governing bodies to engage actively in

fostering and subsidizing research, and in promoting renewable energy on a much larger scale in the past decade than ever before [12].

The increase in demand for renewable energy resources, as opposed to burning of hydrocarbon fossil fuels, is understandable because it is inexhaustible, cleaner and produces virtually no pollution [13], [14].

Research in renewable energy is focused particularly on geothermal, wind, marine, and solar energy, with the aim of developing improved methods of generating electricity and its integration into the existing grid infrastructure for distribution to users. The basic principle is to extract energy from sustainable sources via mechanical or reaction methods.

2.3 SOLAR ENERGY

In wind, wave and tidal current energy extraction mechanical force is used to rotate a turbine which drives an electric generator that generates electricity. Geothermal energy is harnesses heat from the Earth, to produce steam which then powers a turbine-generator set to generate electricity. Solar energy, which is the focus of this thesis, can be used in many different ways for power extraction.

In the first method, mirrors are used to concentrate heat as a means of heating water. This produces steam, which is then used to drive a turbine generator to produce electric power [15]. This method is used in solar thermal power plants. One such plant in the Mojave Desert has a total capacity of 392 megawatts (MW) [15], [16].

The second method uses photovoltaic (PV) cells, which are placed in an array on large panels that are positioned so that they are exposed to a maximum amount of sunlight. The materials from which the cells are constructed, such as silicon or other semiconductor

materials, undergo electron excitation. This process results in the direct conversion of sunlight to electricity, which can then be stored or otherwise integrated into an existing distribution grid infrastructure [15]. The third method, is a hybrid of PV and thermal systems, which has the capability of generating electricity, hot air and hot water by using air and water combined as cooling media [17], [18]. Chapter 3, will discuss this method further.

The promise offered by solar energy technology has been significant since it was first developed in 1860 as a heating method. In the 1950s, solar panels were used to power satellites in orbit, and continue to be used for that purpose today. Solar energy applications are diverse, ranging from simple solar heaters and cookers to complex PV power generation stations. Solar energy research has greatly intensified recently as a result of global interest and increased government funding, particularly within the European Union [19], [20].

Within the last decade, power generated by means of solar technology has vastly increased. For example, as of December 2016, the solar PV capacity amounted to more than 303 GW worldwide, the capacity for concentrating solar thermal power totaled 4.8 GW, and the solar hot water capacity was 456 GW. This represents a meaningful increase in the amount of thermal energy and electricity being generated by solar energy collection [21]. Global electricity produced by renewable energy at the end 2016 is shown in Figure 2-1. The top five countries by the end of 2016, in terms of investment, capacity and production, are shown in Table 2.1 [21].

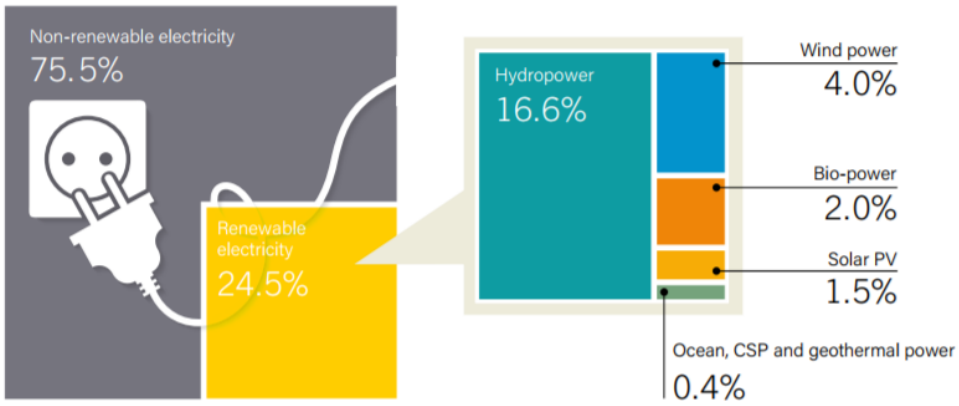

Figure 2-1 Global electricity produced via non-renewable and renewable energy at the end 2016 [10].

Table 2.1:Top five countries in terms of investment, capacity and production [10]

	1	**2**	**3**	**4**	**5**
Solar PV	China	USA	Japan	India	UK
Concentrating solar thermal power	South Africa	China	-	-	-
Solar hot water	China	Turkey	Barazil	India	USA

Solar energy is also much more accessible than traditional consumable fuels and other modern renewable energy sources, because energy from the sun is readily available during daylight hours at every location on the planet. This means that light and heat energy from the sun can be collected anywhere, even in landlocked or isolated locations. In the case of tidal and wind energy, although power can be supplied to remote areas via a distribution grid, far fewer sites suitable for power generation are available than is the case with solar energy.

Analysis regarding the technical potential of concentrating solar power (CSP) was carried out in Europe in the REACCESS project. The study used annual direct normal irradiation (DNI) data provided by NASA to assess the feasibility of placement of solar energy gathering arrays as shown in Figure 2-2.

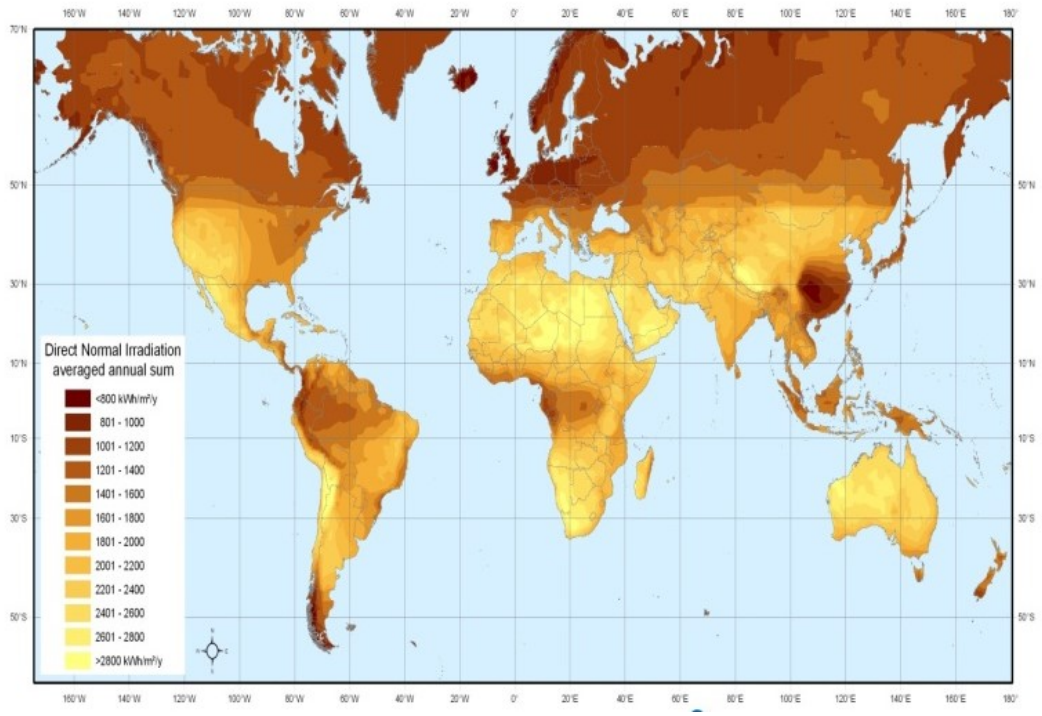

Figure 2-2 Direct normal irradiation [22]

One of the challenges involved with the widespread implementation of solar power generation is the cost of the components. Fortunately, costs have fallen dramatically in recent years, mainly because of the increase in both public and government interest in renewable energy sources. Economies of scale have played a significant role in lowering the costs associated with the production of solar cell panels and inverters. Increased demand and expanded production have also led to greater expertise and efficiency in the manufacture of the various components required to harness solar energy. Ultimately this has also served to reduce costs [13], [23].

CHAPTER 3 PHOTOVOLTAIC AND PHOTOVOLTAIC THERMAL SYSTEM

In this chapter, a brief overview of PV and PVT Systems are introduced. As well as the effect of weather conditions on the PV cell ratio of the PVT system is analyzed [4]-[6], [8], [9].

3.1 PHOTOVOLTAIC

3.1.1 Introduction

Depending on the application, PV systems include several interconnecting components, designed to perform specific tasks, ranging from the powering of small, portable devices, to providing power on a much larger scale, for example by feeding electricity into a main distribution grid. PV systems can be designed to provide power in the form of either alternating current (AC) or direct current (DC). They are also designed to be integrated into a wide variety of configurations. For instance, they can be integrated with other power sources, storage systems, or grid interactive production/utilization monitoring equipment. Because the applications to which PV systems can be applied effectively are varied and wide-ranging, numerous configurations exist, and classifications depend upon the application for which the system is required [11].

3.1.2 Classification

Two primary types of PV system are commonly available on the market, as shown in Figure 3-1. These systems are classified as those which connect to the grid, and those which are isolated, off-grid systems. Off-grid systems in turn can be divided into three categories: Stand-alone systems with or without storage capacity, and hybrid systems [24], [25].

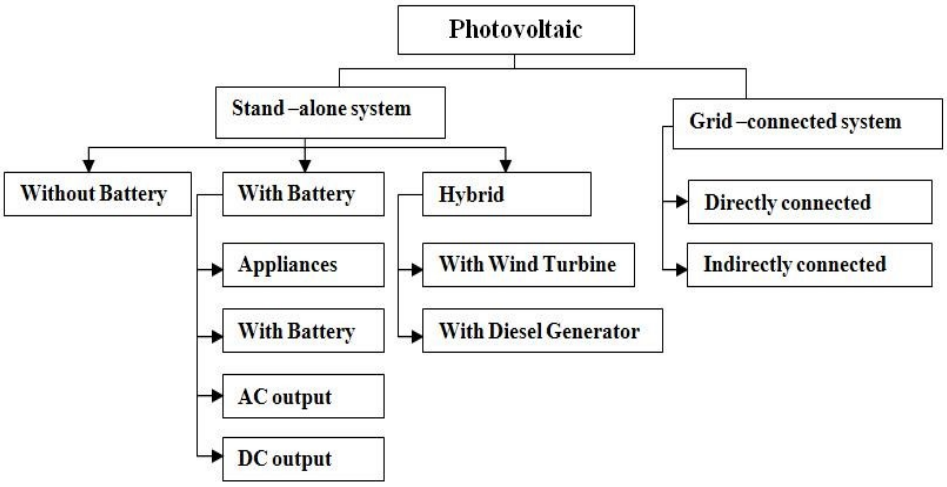

Figure 3-1 PV system classification

PV systems have recently seen expansive growth in grid-connected developments, particularly installations which produce over 200 kW and operate as centralized power plants. Europe has become a major centre for the development of such applications. A significant increase in the implementation such installations has also taken place in the United States [26]. Although off-grid systems were initially popular, beginning with the commercialization of solar energy solutions in the 1970s, as technology advanced and viewpoints have evolved to be more in favour of mass sustainability, the focus has shifted to systems which are integrated with the grid [27].

3.1.2.1 Stand-Alone Systems

Stand-alone, or off-grid PV systems, are generally preferred when the location of the application makes connection to the grid difficult or impossible. In addition, stand-alone systems are frequently employed to power small devices such as watches, calculators, and flashlights. These small-scale applications have stand-alone PV systems with no energy storage capacity, because the appliances are typically run directly from the power being produced by the solar cell [28].

Other off-grid PV systems store solar energy in batteries, for later use. Such systems are generally employed for applications with a large, prolonged demand for power. PV systems that store energy are also useful when energy is required at times when direct solar power is unavailable, such as at night, or when irradiation from the sun is obscured. Off-grid systems with storage are often employed in rural areas where various appliances have power requirements, but there is no access to the grid [29]. This is often the case with cottages, or houses that are built in areas which are not yet developed and are lacking in municipal infrastructure. Off-grid PV systems that store energy are also important for other applications. In recent years, it has become the practice of governments when planning infrastructure, to consider stand-alone PV systems along highways to power nighttime lighting, signage and traffic control lighting, or in rural areas for applications such as small- to medium-scale water pumping stations and purification systems, as shown in Figure 3-2 . This technology has also enabled telecommunications companies to overcome significant challenges, especially since the advent of mobile communications, in providing power to tower and transmitter installations in rural areas where there is no access to the grid [30]-[32]. The use of PV systems to provide power for transmission base stations and repeater arrays has permitted rapid growth of wireless communications infrastructure.

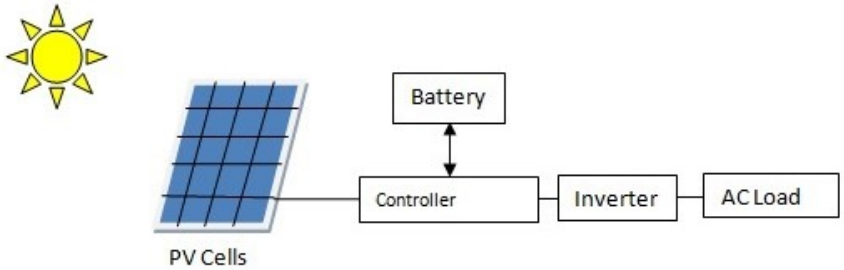

Figure 3-2 Stand- alone System

Hybrid stand-alone PV systems combine PV technology with either another renewable energy generating technology, or a source which uses more traditional power generation methods, such as a diesel or gas-powered generator [33], [34]. In this way, two technologies, working together, produce the energy required for a given application. Such hybrid systems are often used in order to conserve resources or reduce costs [35], [36]. For example, powering a rural summer cottage with a diesel generator alone can involve significant costs, in continually sourcing diesel fuel to operate the generator. This is particularly the case in recent years, since fossil fuels have become more expensive. By investing in a PV system, after the initial investment, which is becoming more economical as the technology advances, the owner of such a cottage would be able to reduce energy costs by having decreased dependence on diesel fuel, and harnessing solar energy to meet part of the total energy requirements. A hybrid system can provide power around the clock more economically and efficiently than would be possible if only traditional, non-renewable energy sources were used. In addition, diesel or gas-powered generators and other mechanical means of power generation with moving parts require lubrication and maintenance, which also have associated costs. PV energy solutions are more economical in this respect, following the initial investment to acquire the components and install them. Thus, a hybrid system can also reduce costs by decreasing the maintenance requirements of mechanical systems [37].

Although large stand-alone systems can and have been employed for such purposes, hybrid PV systems are often designed as a means of providing power to small rural communities, as shown in Figure 3-3 . When such communities are located far from a conventional grid infrastructure, hybrid power systems can offer convenience, cost effectiveness, and

efficiency. Such solutions have been used for communities in industrialized as well as developing nations. PV power systems can also play an important role in providing power for the agricultural needs of rural farming communities, such as electric fencing and water pumping for irrigation.

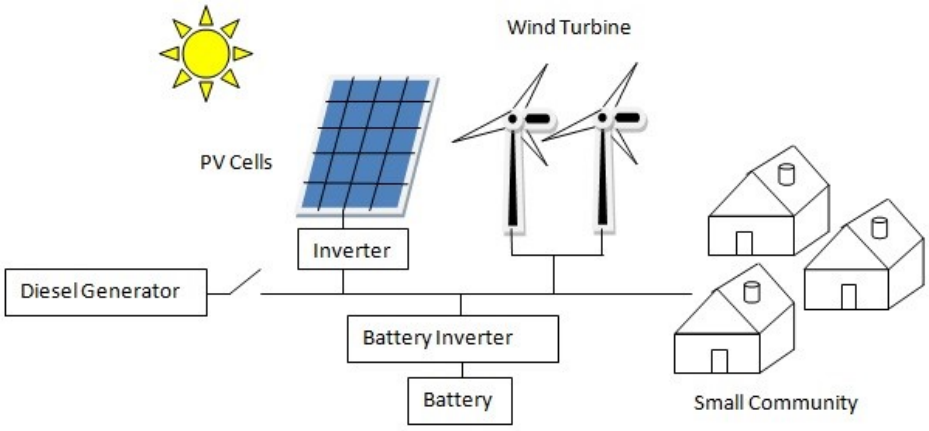

Figure 3-3 Hybrid PV system

3.1.2.2 Grid Connected Systems

Grid-connected, centralized PV systems, as shown in Figure 3-4, have been a particular focus of attention in recent years. In this type of application, a PV system with or without battery storage is connected to a distribution grid by means of a power inverter. Grid-connected systems must be synchronized with the grid to which they are connected in terms of both voltage and frequency. Such systems vary in size, ranging from small-scale, roof-mounted systems in residential neighbourhoods, to large-scale PV power generation stations that generate enough power to service an entire area [38], [39].

The primary advantage of a grid-connected system is that when power is not available from the PV system, it can be drawn from the connected central distribution grid. In turn, PV systems connected to the grid can help to improve the grid voltage and overall reliability.

The emphasis on overall sustainability and reliability, and the desire to achieve a cost-effective integration with current infrastructure in order to facilitate a smoother transition to renewable energy, accounts for the increasing use of grid-connected PV systems. In Germany, an early adopter of large-scale PV power solutions, more than 1 GW of power was generated via grid-connected PV systems in 2004 [40].

An important component of grid-connected PV systems is the inverter, or power conditioning unit (PCU). The PCU converts the DC power produced by the PV panels into AC power that is compatible with the local grid in terms of voltage, frequency, and power quality, as specified by the utility provider [41]. In addition, the PCU has switching functions that prevent power from being shunted to the grid when the grid is not energized. The PCU is incorporated into the system via a bi-directional interface between the PV system with its AC output circuits and the utility grid network. This is usually achieved by a distribution patch panel or a service entrance demarcation. This integration permits the PV system to supply power to either the grid or the locality. When on-site demand is lower than the output from the PV system, the excess power produced can be fed to the grid. Conversely, when on-site power consumption exceeds what the local PV system is capable of providing, power can be drawn from the grid. This most often occurs at night, when the sun is below the horizon. This bi-directional capability, which is a required feature for grid-connected systems, ensures that the PV system does not continue to feed power to the distribution grid if the grid is not in service [41].

Overall, grid-connected PV systems are regarded as being beneficial to the grid to which they are connected, because they can reduce power losses and improve the voltage profile of the utility grid. However, it should be noted that there can also be negative effects

associated with grid-connected PV systems. This is particularly the case if there is a high penetration of grid-connected PV systems. These negative impacts include power and voltage fluctuations, and harmonic distortion. The failure of protective devices can also result in overloading or under-loading of the grid feeders [42].

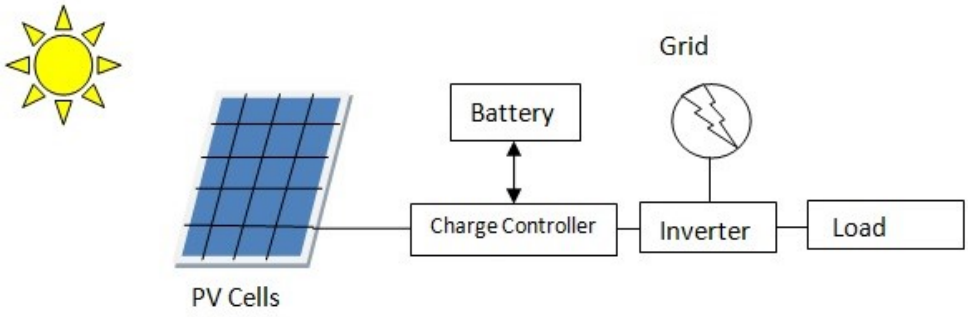

Figure 3-4 Grid- Connected System

3.1.3 PV System Component Structure and Modeling

PV systems, depending on their intended application and the specifics of their expected functionality for any given installation, are comprised of several components which interconnect to create a fully functional off-grid or grid-connected PV system, as shown in Figure 3-5. Regardless of the type of system, the primary component of any PV system is the solar panel. Secondary to the solar panel is the inverter/converter unit, which is also referred to as a power conditioning unit (PCU). This device serves to convert DC power to AC power, and then condition the power to the proper frequency and voltage to service the load. Depending on the configuration, there may also be battery or capacitance banks in use, for storage of the energy produced. Finally, various types of mounting hardware are required to mount the panels in an optimal location for the collection of light quanta at the particular installation location. Rooftop and pole mounting are common. It is also possible to set up a panel array on the ground [43].

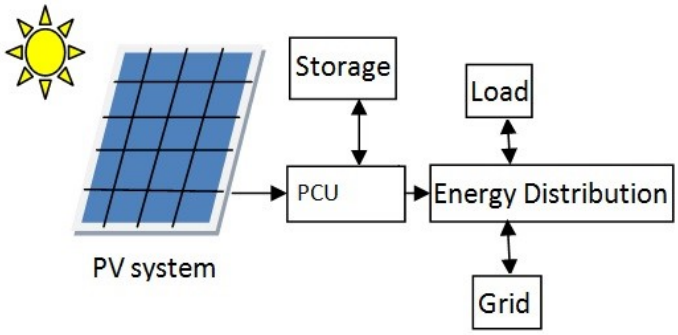

Figure 3-5 PV system components

It is important to note that the power output of a PV module depends upon the intensity of the light from the sun to which the module is exposed, and upon the temperature of the semiconductor-based cells which make up the larger panels. For this reason, the power must be conditioned via a power conditioning unit (PCU), to stabilize the output in order to deliver it in a form suitable for the grid, batteries, or end load. It is also important to point out that not all systems require conversion of the DC power originally produced by the system into AC power. Small applications such as watches, calculators, flashlights, and small panel kits sold for powering camping or hiking gear are only required to produce DC power similar to the dry cell alternative. Larger installations, including those which supplying loads of a residential, commercial or industrial nature, usually require inverters to facilitate the conversion to AC power. In grid-connected solutions, additional components that are part of the PCU serve to obtain the proper frequency cycle, and to ensure that the flow of power is bi-directional as required, depending upon peak/off-peak hours, the rate of consumption versus the power produced by the local system, and compensation for power fluctuations due to meteorological conditions [44].

3.1.3.1 PV Cell

The smallest functional unit of a PV system is the solar cell. Types of solar cell include mono-crystalline silicon, poly-crystalline silicon, amorphous silicon, and thin film silicon cells. Experiments and research are also being done on other semiconductor materials. Copper-indium selenide, cadmium telluride, gallium arsenide, and many other organic and inorganic polymers are among the alternative semiconductor materials being used to produce PV cells. At present, approximately 90% of the PV cell technology prevailing in the market is divided between mono- and poly-crystalline types [45].

PV cells use a photovoltaic effect to produce electricity. This effect is a quantum-mechanical process. The basic structure of a PV cell is that of a p-n junction in the silicon semiconductor material, similar to a diode, as shown in Figure 3-6. An electric field is formed at the junction by means of impurity doping, which uses p-doping on one side and n-doping on the other. Essentially, when the cell is irradiated with light quanta, the photons create charge carriers, which are separated across the electrical field. This creates a depletion region, which exists between the p and n sides of the junction. As a result, a voltage is generated across the external contacts, which in turn creates current flow through to the load, if the circuit is completed [46], [47]. The photocurrent flowing from the solar cell is proportional to the irradiation intensity of the sunlight.

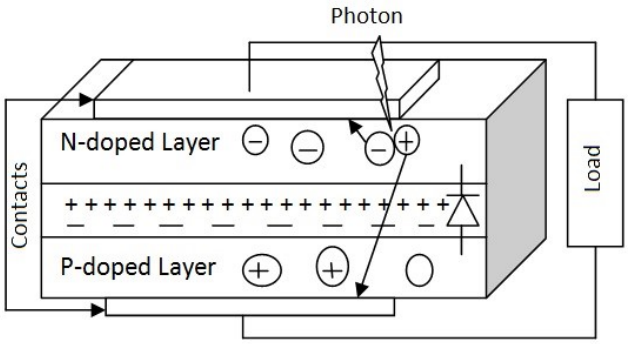

Figure 3-6 PV cell structure

As shown in Figure 3-7, a PV cell equivalent circuit is comprised of a current source paired with a parallel diode. The presence of parasitic resistance should be noted: The series resistance, R_s , normally has a small value; and the shunt resistance, R_{SH}, is relatively large. R_s is primarily influenced by material factors such as the bulk resistance offered by the semiconductor material, metallic contacts and interconnections. R_{SH} is attributable to non-idealities and impurities present at the p-n junction.

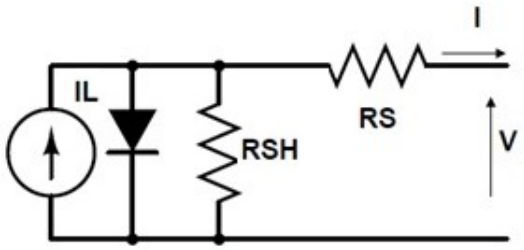

Figure 3-7 PV cell equivalent circuit

A generalized equation for the diode current of the PV cell is given by [48]-[52]:

$$I = I_L - I_o \left(\exp\left[\frac{q(V + IR_{s)})}{nkT}\right] - 1\right) - \frac{V + IR_s}{R_{SH}} \tag{3.1}$$

$$I_L = I_{L,ref} \frac{G}{1000}(1 + \alpha(T - T_{ref}) \tag{3.2}$$

$$R_s = R_{s0} - \frac{nkT}{qI_o} \exp(\frac{-qV_{oc}}{nkT}) \quad (3.3)$$

$$R_{SH} = R_{SH0} \quad (3.4)$$

where *I* is the overall diode current produced by the cell, I_L, is the current generated by the incident light quanta arriving at the cell (which is directly proportional to the level of solar irradiation), I_o is the reverse saturation current of the diode, q is the electron charge ($1.60217646\ x10^{-19}\ C$), *n* is the ideality factor, *k* is the Boltzmann constant ($1.3806503\ x\ 10^{-23} J/K$), *T* is the temperature of the PV cell (more specifically the temperature at the p-n junction) measured in Kelvin, T_{ref} is the reference temperature, *G* is the solar irradiance, *V* is the voltage across the cell, R_{SH0} is the slope of the I-V curve at the (0, short-circuit current) point, and R_{s0} is the slope of the I-V curve at the (open-circuit voltage, 0). The values of, R_s and R_{SH} are determined under varying environmental conditions.

PV cells are characterized by several important parameters, which are briefly discussed below. In general, the short-circuit current (I_{sc}), open-circuit voltage (V_{oc}), fill factor (*FF*) and cell efficiency *(η)* are specific parameters that are determined via the I-V curve of a PV cell, as shown in Figure 3-8.

The variable I_{sc} represents the current passing through the PV cell when the voltage across the cell is zero, i.e., when the cell is short-circuited.

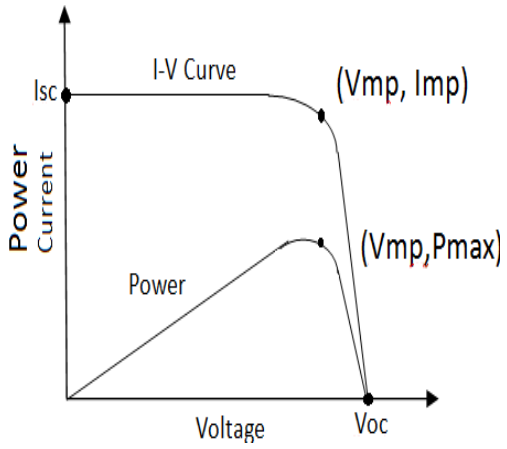

Figure 3-8 The I-V curve of a PV cell

The short-circuit current is caused by the generation and accumulation of light-generated carriers. An ideal PV, operating with the most modest resistive loss mechanisms, has a short-circuit current equal to the light-generated current. Thus, the short-circuit current is the maximum possible current that can be drawn from a PV cell.

The variable V_{oc} represents the greatest possible voltage available from a PV cell. This voltage is achieved when the cell has zero current flow. The open-circuit voltage is proportional to the amount of forward bias on the PV cell, as a result of the bias of the p-n junction with light-generated current. $V_{oc}$is depicted in the I-V curve, and is given by [48]:

$$V_{oc} = \frac{nkT}{q} In(\frac{I_L}{I_o} + 1) \tag{3.5}$$

The short-circuit current and the open-circuit voltage are the maximum possible current and voltage, respectively, for a PV cell. However, it should be kept in mind that when either of these states is achieved, the power from the cell is zero. In conjunction with the short-circuit current and the open-circuit voltage, the fill factor (*FF*) specifies the greatest possible power draw from a PV cell. The *FF* is the ratio of the maximum power from the

PV cell to the product of the short-circuit current and the open-circuit voltage, and is given by [48]:

$$FF = \frac{V_{MP} I_{MP}}{V_{OC} I_{SC}} \tag{3.6}$$

where V_{MP} is the maximum-power voltage and I_{MP} is the maximum-power current.

PV efficiency is the parameter most commonly used to compare one model of PV cell with another. Efficiency is defined as the ratio of the energy output by the PV cell to the energy input by the sun. It is important to note that the efficiency rating of a PV cell does not merely represent the performance of a PV cell in itself, but also depends on the spectrum and intensity of the irradiation by incident sunlight, as well as the temperature of the PV cell at the p-n junction. Thus, the conditions under which efficiency is measured must be handled with care in order to achieve a meaningful comparison between PV cells. PV cells intended for terrestrial use, at the surface of the Earth, are measured according to air mass 1.5 (AM1.5) conditions, at a temperature of 25^o C. PV cells designed to be used in space are measured at AM0 conditions. The efficiency of a PV cell is calculated as the fraction of incident power which is converted into electrical power, and is given by [48]:

$$P_{max} = V_{oc} I_{sc} FF \tag{3.7}$$

$$\eta = \frac{V_{oc} I_{sc} FF}{P_{in}} \tag{3.8}$$

Where P_{in} is the incident power of solar radiation per unit area of PV cell.

Resistive effects in PV cells reduce the cell efficiency by lowering power output, because power dissipates in the resistances presented. The types of parasitic resistance most

commonly encountered in PV cells are series resistance and shunt resistance. In most cases, the combined values of these parasitic resistances reduce the fill factor. The magnitude and effect of the series and shunt resistance depend upon the geometry of the PV cell at its operating point.

Series resistance in a PV cell has three primary causes: The movement of the current through the emitter and base of the PV cell, the contact resistance offered by the junction of the metal contact and the silicon semiconductor material, and the resistance inherent in the top and bottom metal contacts of the PV cell. Series resistance reduces the fill factor, and exceedingly high levels may also reduce the short-circuit current.

Noticeable power losses due to the presence of shunt resistance usually result from defects caused by poor manufacture, rather than from poor cell design. A low shunt resistance can cause power loss in PV cells by providing an alternative path for the flow of light-generated current. This diversion of the current reduces the amount of current flowing through the PV cell p-n junction, and reduces the voltage output of the solar cell.

Individual PV cells based on silicon semiconductors typically produce about half a volt. Because this output is so small, many cells are connected in series in a PV module. Many modules are then grouped together to form a PV panel, and PV panels are mounted and arranged to form PV arrays. All the cells in the array produce the power output that is utilized for end power conditioning by subsequent PV system components. The accompanying Figure 3-9 depicts the organization of PV collector components, from the simplest unit (the individual PV cell) to the most complex (the PV array) [53].

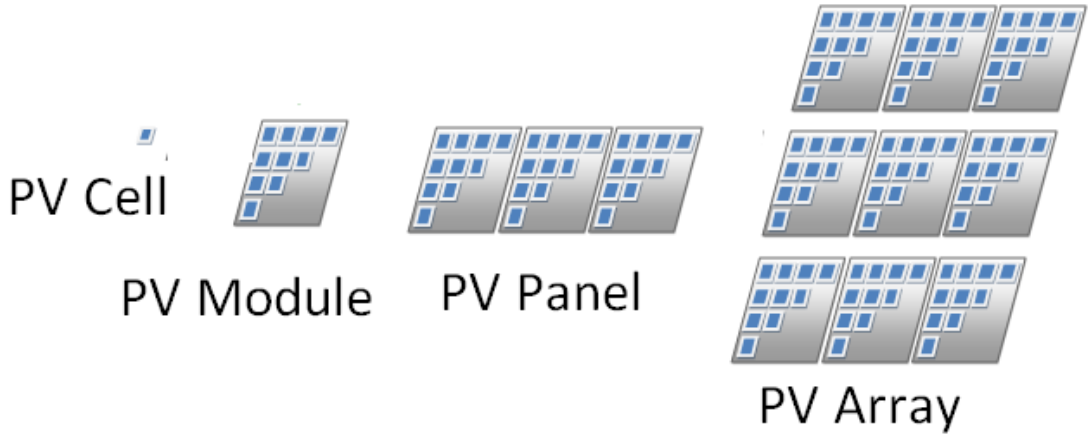

Figure 3-9 PV cell arrangement

3.1.4 PV Challenges

3.1.4.1 Fluctuation

Fluctuation is an important challenge, because it is a common issue that results from natural phenomena. Natural fluctuation in the irradiance of light from the sun is caused by the formation and movement of clouds. Such fluctuations give rise to operational problems and make it difficult to forecast the output power. Differing cloud patterns and cloud densities hinder the accurate calculation of potential outcomes. In addition, wind speed can affect the duration of fluctuations caused by cloud formations. Because wind speed is variable, present conditions can persist from a few minutes to several hours, and it is difficult to predict the length of time that fluctuations may last [54]. In view of these variables: Cloud type and size, wind speed, and topology and configuration of the PV array, it is clear that there is no universal solution that can be employed to deal with this problem. Clouds differ in size and type. Cloud types can be identified by comparing the apparent size of puffs of cloud to that of an outstretched hand. A cirrocumulus cloud has puffs of cloud that are small, comparable to a fingernail; an altocumulus cloud has puffs of cloud that are medium-sized, comparable to a thumb; and a cumulus cloud has puffs or cloud that

are large, comparable to a fist. The time of day most subject to wide power fluctuations is usually around noon, when the sun is at its zenith. At this time, the output of the PV system is potentially the highest, because irradiation from the sun falls most directly on the array, resulting in the highest level of electron excitation in the solar cells. If there are clouds at this time of day, there can be wide fluctuations in the power provided to the grid. Relatively high equipment costs also limit the solutions available to electrical utility companies, to reduce the negative impacts of such fluctuations [54].

3.1.4.2 Harmonics

While fluctuation is a problem which results from natural phenomena, there are also technology-based challenges that must be addressed to avoid problems in the grid and prevent damage to system loads. In particular, waveform harmonics are a significant concern. This issue arises from PCU conversion of the DC current produced by the solar panels to AC current. This is performed via a semi-conductor switching circuit; however, the AC wave resulting from this method of conversion is not a perfectly sinusoidal wave, because there is not a smooth transition between the switching phases. Modern PCUs employ methods which compensate for this imperfect waveform, but older devices with poor-quality, inefficient inverter circuits and components may generate serious harmonics during the conversion process [55]. It should be noted that the effects of waveform harmonics are cumulative and can result in significant undesirable impacts on the grid, such as excessive voltages and currents due to series and parallel resonance. Harmonics can also impair the functionality of attached appliances and cause component damage [55]. Research in the area of inversion waveform harmonics has found that the odd numbered

harmonics are the most problematic with regard to the severity of the distortion produced. Thus, the 3rd, 5th, 7th, etc., harmonics are the ones which are of primary concern [56]

The complete elimination of waveform harmonics is not achievable via current technology, however, modern PCUs are designed to limit harmonics and perform waveform smoothing, similarly to any modern inverting power supply. One solution for managing harmonics is pulse width modulation (PWM) [57]. PWM serves to control the voltage by manipulating the interval and the width of the pulse, so that the average voltage output equals that of the required fundamental waveform. After PWM is employed, in an additional step, the low line current distortion produced by the modulation process is filtered out.

LCL filters are commonly used in many topologies. These filters achieve excellent attenuation with relatively inexpensive components, and are suitable for high power applications. In other words, good power quality can be obtained with a low component cost [58]-[60].

3.1.4.3 Cost of PV Systems

The overall cost of PV system implementation continues to be relatively high in comparison to the cost of other renewable energy production systems. However, increased demand has caused prices to decline. For continued improvements to be made, public research funding is needed to facilitate new research and enhance existing study efforts. In addition, increased public awareness of renewable energy and PV systems is required. In 1992, the cost per watt of energy produced by a PV crystalline cell was approximately $4.23. Ten years later, that amount had fallen to $1.72 [61]. The price continues to fall as the volume of production increases with demand. The accompanying figure illustrates the

general trend of solar energy production costs. It should be noted that the Chinese company SUN-TECH, the largest producer of PV cells and panels worldwide, forecast that manufacturing costs would decrease by the end of 2017 to approximately $0.32 per watt [62].

3.2 PHOTOVOLTAIC THERMAL SYSTEM

3.2.1 Introduction

Hybrid systems consisting of PV and thermal modules may be the best choice to minimize costs and equipment, and increase overall efficiency. The photovoltaic thermal (PVT) model produces both thermal and electrical energy at the same time. PVT systems uses the same frames for the PV and thermal modules [63].

Kern and Russell introduced the concept of the first PVT collector [64], [65]. Hendrie and Florschuetz introduced the theoretical (Hottel-Whillier) PVT model, by using conventional thermal plane concepts [65], [66].

3.2.2 Classification

A PVT system can generate electricity, hot air and hot water, by using air and water combined as a cooling substance. The system performance can be evaluated under indoor weather conditions [17]. A solar air heater with a compound parabolic concentrator has been investigated with a varying mass air flow rate [18].

In general, glazed PVT water collectors are more suitable for thermal energy applications, and unglazed PVT water systems are better for electrical energy applications [67].

3.2.3 PVT System Model

The water flowing underneath the absorber is heated by solar radiation that is transferred through the PV cells to the absorber. The water flows from the bottom of the collector toward the top. The water output from the part of the collector that is covered by PV cells is input to the part that is not covered, as shown in Figure 3-10 [65].

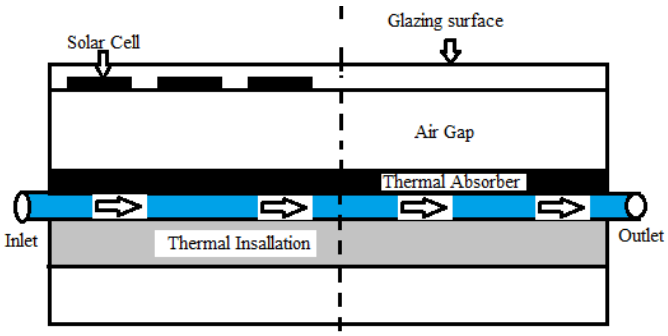

Figure 3-10 Cross-section of PVT collector

3.2.3.1 Mathematical Thermal Analysis

PV cells can be placed on the upper or lower portion of a PVT collector. In this research, the lower portion of the collector was covered by PV cells, because more thermal and electrical energy can be gained there than in the upper portion [68].

Energy balance equations have been derived for a quasi-steady state. The ohmic losses and heat capacity of PVT collectors are neglected. The energy balance equations providing the thermal parameters of PVT water collectors are [65], [68]:

$$T_c = \frac{(\alpha\tau)_{1,eff} I(t) + U_{t\,c,a} T_a + h_{c,p} T_p}{U_{t\,c,a} + h_{c,p}} \tag{3.9}$$

$$T_p = \frac{(\alpha\tau)_{2,eff} I(t) + PF_1 (\alpha\tau)_{1,eff} I(t) + U_L T_a + h_{p,f} T_f}{U_{t\,c,a} + h_{c,p}} \tag{3.10}$$

$$(\alpha\tau)_{1,eff} = (\alpha_c - \eta_c)\beta_c\tau_c \tag{3.11}$$

$$(\alpha\tau)_{2,eff} = \alpha_p(1 - B_c)\tau_g^2 \tag{3.12}$$

$$U_{t\,c,a} = 5.7 + 3.8V \tag{3.13}$$

$$U_{L1} = \frac{U_{t\,c,a}h_{c,p}}{U_{t\,c,a} + h_{c,p}} \tag{3.14}$$

$$PF_1 = \frac{h_{c,p}}{U_{t\,c,a} + h_{c,p}} \tag{3.15}$$

where$(\alpha\tau)_{eff}$ is the product of effective absorptivity and transmissivity, $I(t)$ is incident solar intensity (w/m^2), $U_{t\,c,a}$ is the coefficient for overall heat transfer from the solar cell to the ambient surrounding through the glass cover (w/m^2 K), T_a is the ambient temperature (K), $h_{c,p}$ is the solar cell-plate the solar cell-plate heat transfer coefficient (w/m^2), T_p is the plate temperature (K), PF_1 is the penalty factor due to the glass cover of the PV cells, U_{L1} is the coefficient for overall heat transfer t from the blackened surface to the ambient (w/m^2 K), $h_{p,f}$ is the plate-fluid heat transfer coefficient (w/m^2), and V is the wind speed (m/s). Values for $h_{p,f}, \alpha_c, \eta_c, \tau_c, \alpha_p$ and τ_g are given in [65], [68]. T_f is the average temperature of flowing water, given as:

$$T_f = \frac{T_{fin} + T_{fo2}}{2} \tag{3.16}$$

where T_{fin} is the inlet water temperature (k), T_{fo2} is the outlet water temperature of PVT system (k), given as [68]:

$$T_{fo2} = \left[\frac{(\alpha\tau)_{c,eff} I(t)}{U_{L,c}} + T_a\right]\left[1 - exp\left(-\frac{\acute{F} A_c U_{L,c}}{\dot{m}_f C_f}\right)\right] + \quad T_{fi2}\exp\left(-\frac{\acute{F} A_c U_{L,c}}{\dot{m}_f C_f}\right) \tag{3.17}$$

where $\acute{F}$ is the flat-plate collector efficiency factor, A_c is the collector area (m^2), $\dot{m}$ is the rate of flow of water mass (kg/s), C_f is the specific heat of water ($J/kg\ K$), $U_L$is the coefficient for overall heat transfer from blackened surface to ambient ($w/m^2\ K$), and T_{fi2} is the inlet temperature of water for remaining part of collector which is equal to T_{fo1}(k), given as as [68]:

$$T_{fo1} = \left[\frac{PF_2(\alpha\tau)_{m,eff} I(t)}{U_{L,m}} + T_a\right]\left[1 - exp\left(-\frac{\acute{F} A_m U_{L,m}}{\dot{m}_f C_f}\right)\right] + T_{fin}\exp\left(-\frac{\acute{F} A_m U_{L,m}}{\dot{m}_f C_f}\right) \tag{3.18}$$

$$PF_2 = \frac{h_{p,f}}{U_L + h_{p,f}} \tag{3.19}$$

$$U_{L,m} = \frac{U_L h_{p,f}}{U_L + h_{p,f}} \tag{3.20}$$

$$(\alpha\tau)_{m,eff} = PF_1\,(\alpha\tau\,)_{1,eff} + (\alpha\tau\,)_{2,eff} \tag{3.21}$$

where PF_2 is the penalty factor due to the absorber below PV module, glass to glass PV cells area and A_m is the area of PV cells (m^2).

The rate of useful thermal energy of PVT water collector is given in [65], [68], [69]:

$$\dot{Q}_u = \dot{m}_f C_f \left(T_{fo2} - T_{fi}\right)$$
$$= \left[A_m F_{Rm} PF_2 (\alpha\tau)_{m,eff} (1 - k_1) + A_c F_{Rc} (\alpha\tau)_{c,eff}\ \right] I(t) \quad (3.22)$$
$$- \left[A_m F_{Rm} U_{L,m} (1 - k_1) + A_{c1} F_{Rc} U_{L,c}\right] (T_{fi1} - T_a)$$

where $K_1 = \left[\frac{A_c F_{Rc} U_{L,c}}{\dot{m}_f C_f}\right]$.

The instantaneous thermal efficiency of PVT collector is a function of the solar radiation, the input fluid temperature , and the ambient temperature and is given as [65], [68]:

$$\eta_i = F_{Rm}(PF_2(\alpha\tau)_{m,eff} - \frac{U_{L,m}(\,T_{fin} - T_a)}{I(t)} \quad (3.23)$$

where $F_{Rm}(PF_2(\alpha\tau)_{m,eff}$ is the gain factor and $F_{Rm} PF_2 U_{L,m}$ is the loss factor.

3.2.3.2 Mathematical Electrical Analysis

The electrical energy and electrical system parameters are calculated via PV module simulations. A general equation for the current flowing out of the PV cell is [48], [70]:

$$I = I_L - I_s \exp\left[\frac{q\left(V + IR_{s)}\right)}{nkT} - 1\right] - \frac{V + IR_s}{R_{SH}} \quad (3.24)$$

$$I_L = \frac{I(t)}{I(t)_{ref}} \left(I_{Lref} + \alpha\left(T_c - T_{cref}\right)\right) \quad (3.25)$$

$$I_S = I_{Sref}\left(\left(\frac{T_c}{T_{c_{ref}}}\right)^3 exp\left(\frac{qE_g\left(\left(\frac{1}{T_{cref}} - \frac{1}{T_c}\right)\right)}{kn}\right)\right. \quad (3.26)$$

where *I* is the net output current produced by the cell (A), I_s is the reverse saturation current of the diode (A), I_{sref} is the reverse saturation current of the diode at reference condition

(A), q is the value of the electron charge ($1.6 \times 10^{-19} C$). n is the ideality factor, k is the Boltzmann constant $(1.38 \times 10^{-23} J/K)$. T is the temperature at the p-n junction of the cell (k), V is the output voltage of the cell. I_L is the current generated by the incident light arriving at the PV cell. I_{Lref} is the current generated by the incident light arriving at the PV cell at reference condition, and R_S is series resistance which primarily influenced by material factors such as bulk resistance offered by the semiconductor material, metallic contacts, and interconnections, and R_{SH} is shunt resistance, is due to non-idealities and impurities present in the p-n junction [48], [71].

3.3 PV COVERAGE RATIO FOR MAXIMUM OVERALL THERMAL ENERGY OF PVT SYSTEM

In this section, the effect of weather conditions on the PV cell ratio in PVT systems is presented, to increase system efficiency and reduce costs and emissions.

The annual energy performance and CO_2 emissions for different climate conditions have been studied in cold (London), warm (Shanghai) and hot (Hong Kong) areas [72]. Fully covered PVT collectors are suitable for applications with low temperatures, from 25^c to 40^c [73]. The temperature profile of the PV module was studied for cloudy and clear daytime conditions [74]. Thermal and electrical outputs are enhanced when the photovoltaic thermal flat-plate collector (PVT-FPC) is partially covered with PV modules [65], [75].

An analytical expression of useful energy was derived for N PVT flat-plate water collectors connected in series and partially covered with PV modules in the lower and upper portions [76], [77].

In various Indian cities, analyses of thermal and electrical energy have been conducted for different weather conditions, for series and parallel combinations of collectors with a constant mass flow rate. Annual thermal, electrical energy and total carbon credits earned by the PVT water heater system were calculated for New Delhi conditions [66]. For PVT systems with a constant mass flow of air, annual overall energy and exergy gains for three different configurations and weather conditions were evaluated [78].

Three different types of PVT air collector (unglazed, glazed, and conventional hybrid PVT air collectors) were studied. The annual overall thermal energy (OTE) and exergy gains for different types of PVT were investigated [79].

The overall thermal and electrical energy and overall exergy for N partially covered photovoltaic thermal compound parabolic concentrator (PVT-CPC) water collectors connected in series was investigated and calculated for two weather conditions in India, in January and June 2015 [65].

The OTE and exergy gains were evaluated for four different cases at a constant flow rate, for N PVT-CPC water collectors connected in series. The annual reduction of CO_2 emissions and amount of money saved were examined [80].

The reduction of CO_2 emissions was evaluated for four different cases, for a 20%, 40%, 60% and 80% PV coverage area, at a constant flow rate, for each month throughout the year. Two models were proposed to determine monthly reductions of CO_2 emissions and the PV coverage area ratio [6].

Most previous work has focused on a constant fluid flow rate, different PV coverage areas with discrete, limited percentages (e.g. 25%, 50%, 75% and 100%) and a short time span

during the year. The present work utilizes real data which contain different values of solar radiation, wind speed, flow rate, temperature of the input water, and temperature of the air, for one year. Furthermore, variable water flow rates (heat exchanger fluid flow rates) and different percentages of PV coverage are used to calculate the monthly and seasonal OTE [5]. This will assist in determining the appropriate ratio of the PV coverage area required to maximize the OTE, in order to maximize the overall system efficiency and minimize CO_2 emissions [4], [6].

3.3.1 PVT System and Data Description

For this study, a PVT system consisting of a single glazed flat-plate collector with an effective area of 2.156 m^2 is used for the simulation. The collector is covered with crystalline silicon solar cells. The area of each solar cell unit is 0.018 m^2. The number of cells is incremented by one, beginning in the lower portion of the collector, until full coverage with the cells is achieved, as shown in Figure 3-11. The system configuration of the PVT water collector, which includes thermal and electrical parameters, is given in [65], [68].

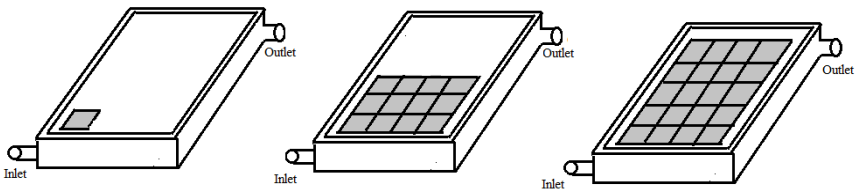

a) one cell b) partial coverage c) full coverage

Figure 3-11 PV coverage ratio for different cases

This work is based on a dataset for various environmental conditions in a North American city. The solar radiation, ambient temperature, wind speed, water flow rate and temperature

of the input water were measured every hour over a one-year time span, as shown in Figure 3-12. The dataset was obtained from a solar thermal system used for water heating, with measurements taken by a pyranometer, a wind speed meter and thermometers [81]. It has been assumed that an hourly dataset is sufficient to represent environmental fluctuations. Moreover, it is important to study the weather patterns over an entire year, since the weather patterns vary seasonally.

The data set could be represented in different scale levels using fuzzy c-mean clustering technique. This technique breaks a large dataset to smaller groups where each observation within every group is more similar to each other than it is to an observation in another group as shown in Figure 3-13 for radiation case. Two different groups of clustering for solar radiation are selected at 365 and 12. However, in this work, all real data are used to represent the actual system.

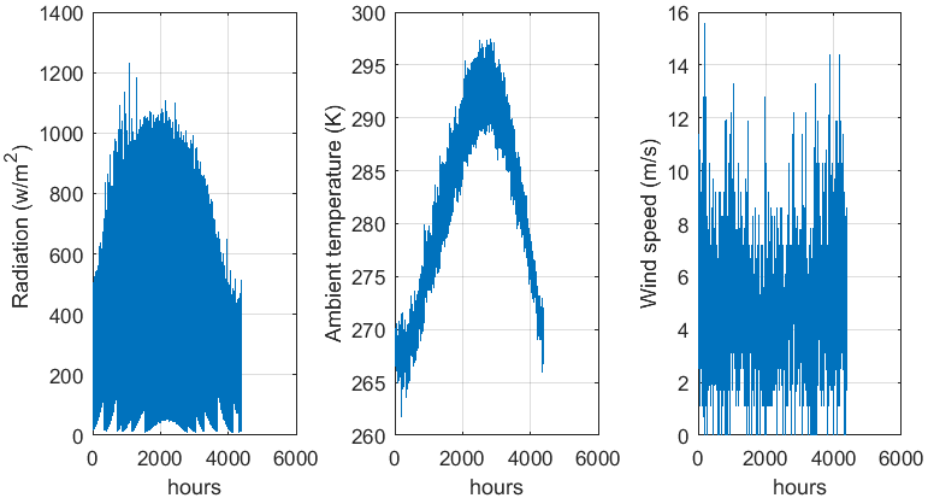

Figure 3-12 Solar radiation, ambient temperature and wind speed for one year

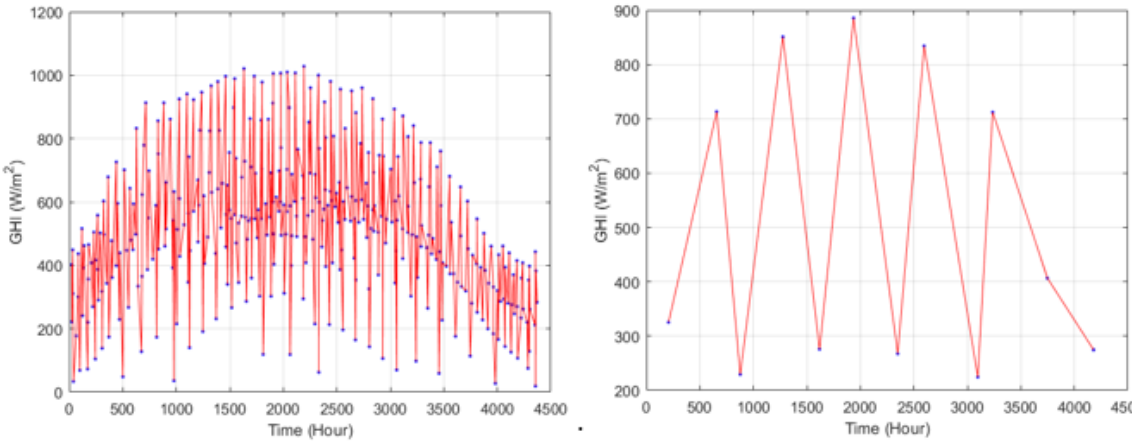

a) Number of clustering group=365 b) Number of clustering group=12

Figure 3-13 Solar radiation values at different clustering group numbers which are presented by the center of the cluster for one year

By selecting a specific day from Figure 3-12, hourly solar radiation, ambient temperature, and wind speed are obtained for a day in May, as shown in Figure 3-14. Hourly solar radiation, and ambient temperature increase until 2 pm and then they start declining. However, wind speed changes randomly during the day.

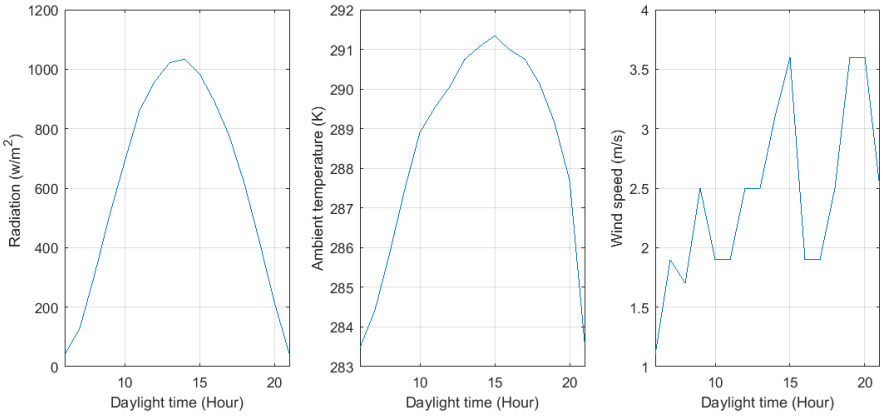

Figure 3-14 Hourly solar radiation, ambient temperature and wind speed for a day in May

The simulated PVT system used in this work is modeled using *MATLA B* ^{TM}. The weather dataset and water specifications are used as input parameters for the PVT system. The

output of the system is defined as the OTE, which includes the thermal and electrical output of the system as shown in Figure 3-15.

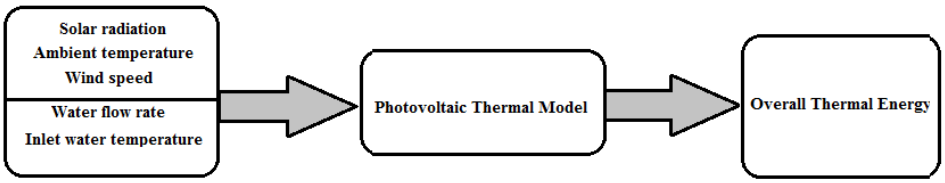

Figure 3-15 Simulated model of the PVT System

3.3.2 Simulation of the PVT System

Two cases are analyzed in this thesis, the first with a constant flow rate value (0.03 kg/s), and the second with flow rate values varying with time. For the second case, the different flow rate values applied are measured at a thermal system used for water heating. These flow rate values are controlled by a water pump driven by a PV system. Furthermore, these values reflect the effect of environmental parameters. The OTE rate of the PVT system is based on the first law of thermodynamics, and is given in [80]:

$$\dot{Q}_{u,total} = \sum \dot{Q}_{u,thermal} + \sum \frac{\dot{Q}_{u,electrical}}{C} \tag{3.27}$$

$$\dot{Q}_{u,electrical} = P_E \tag{3.28}$$

where C is the conversion factor for the thermal power plant. Its value depends upon the type of power plant. This coefficient varies from 38% to 44% for a steam turbine fuel oil power plant, and from 39% to 47% for a steam turbine coal fired power plant [80], [82].

As shown in Figure 3-16, for both cases, maximum thermal energy is obtained for the variable and constant flow rate cases. The output thermal energy exhibits the same trend of change, with a slight difference in the amount.

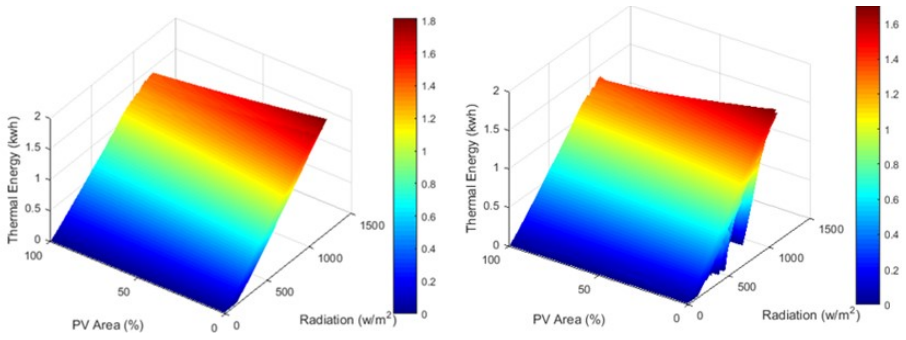

a) constant flow rate b) variable flow rate

Figure 3-16 Relation between hourly thermal energy, PV area coverage and solar radiation

From Figure 3-17 and Figure 3-18, it can be observed that in both cases, the maximum thermal energy changes with changes in the temperature and wind speed. From Figure 3-16 to Figure 3-18, it can be seen that the thermal energy of the PVT system is determined more by the solar radiation than by the temperature and wind speed.

From Figure 3-19, it can be observed that the electrical energy increases when the PV coverage area increases for both cases, with constant and variable flow rates. Figure 3-19 and Figure 3-20 show that the maximum electrical energy is obtained with low temperature and high solar radiation values. For the variable and constant flow rate cases, the electrical energy exhibits the same trend of change, with a slight difference in the amount. However, the effect of wind speed on the generation of electrical energy is less significant than the effect of solar radiation and temperature, as shown in Figure 3-21.

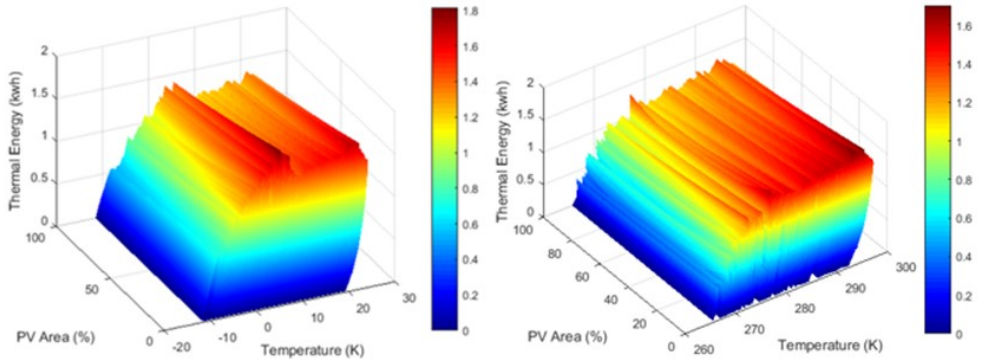

a) constant flow rate b) variable flow rate

Figure 3-17 Relation between hourly thermal energy, PV area coverage and area coverage and temperature

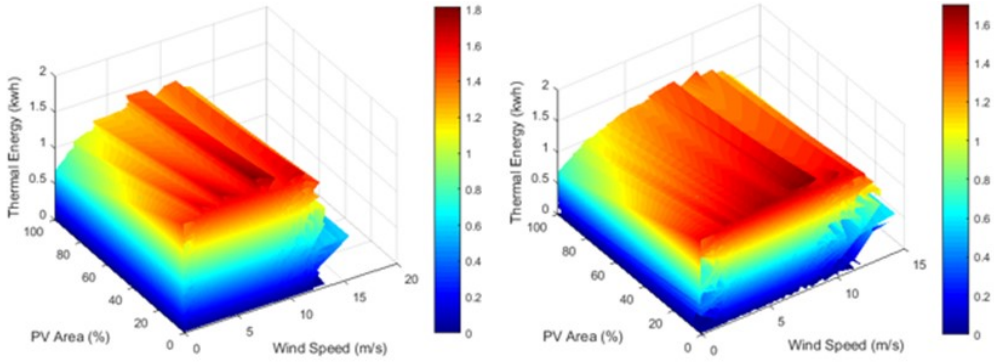

a) constant flow rate b) variable flow rate

Figure 3-18 Relation between hourly thermal energy, PV area coverage and wind speed

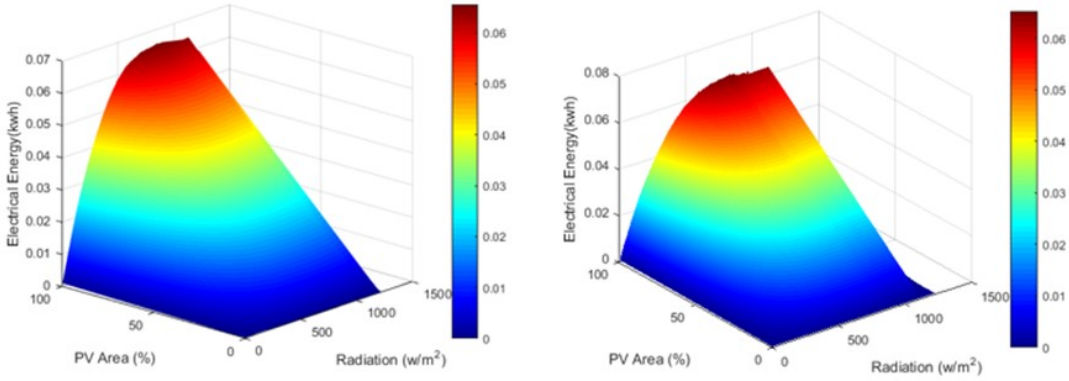

a) constant flow rate b) variable flow rate

Figure 3-19 Relation between hourly electrical energy, PV area coverage and solar radiation

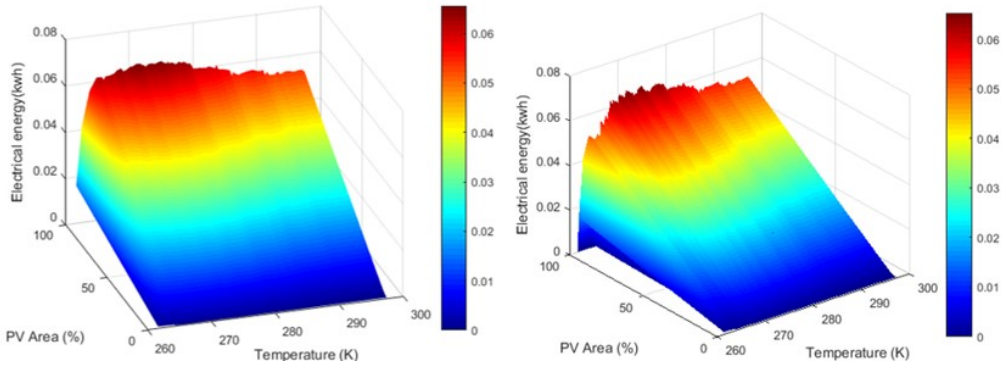

a) constant flow rate b) variable flow rate

Figure 3-20 Relation between hourly electrical energy, PV area coverage and temperature

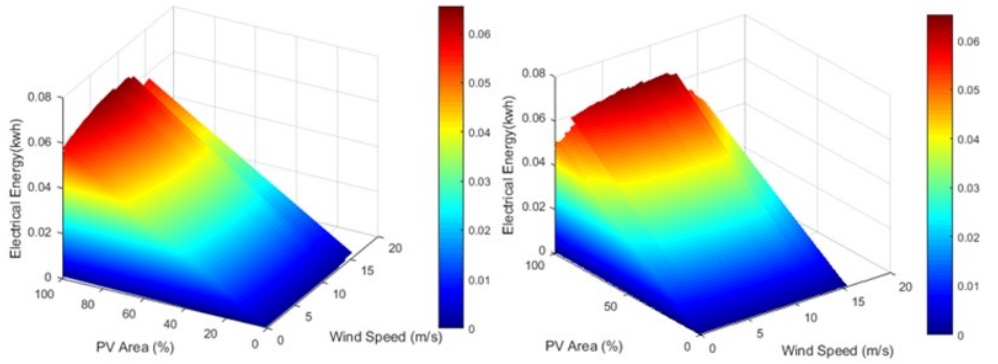

a) constant flow rate b) variable flow rate

Figure 3-21 Relation between hourly electrical energy, PV coverage area and wind speed

The maximum daily OTE of the PVT system is calculated for both flow rate cases, as shown in Figure 3-22. The maximum OTE between days 1 and 100, and days 270 and 365, occurred when the PVT system was substantially covered with PV cells, as shown in Figure 3-22a and Figure 3-22c. However, for the same period, the OTE is almost constant for the variable flow rate, shown in Figure 3-22c, as compared to the constant flow rate, shown in Figure 3-22a. The percentage of PV coverage area is between 20% and 30%, as indicated in Figure 3-22b. In contrast, the maximum OTE for the rest of the year, between days 100 and 270, occurred when the PVT system was not covered. However, it can be seen from

Figure 3-22a that the OTE is constant for a constant flow rate, as compared to the variable flow rate shown in Figure 3-22c for the same period. As shown in Figure 3-22b, the maximum OTE is higher in the first case than in the second case, illustrated in Figure 3-22d, due to the greater thermal energy obtained from the constant flow rate in the first case.

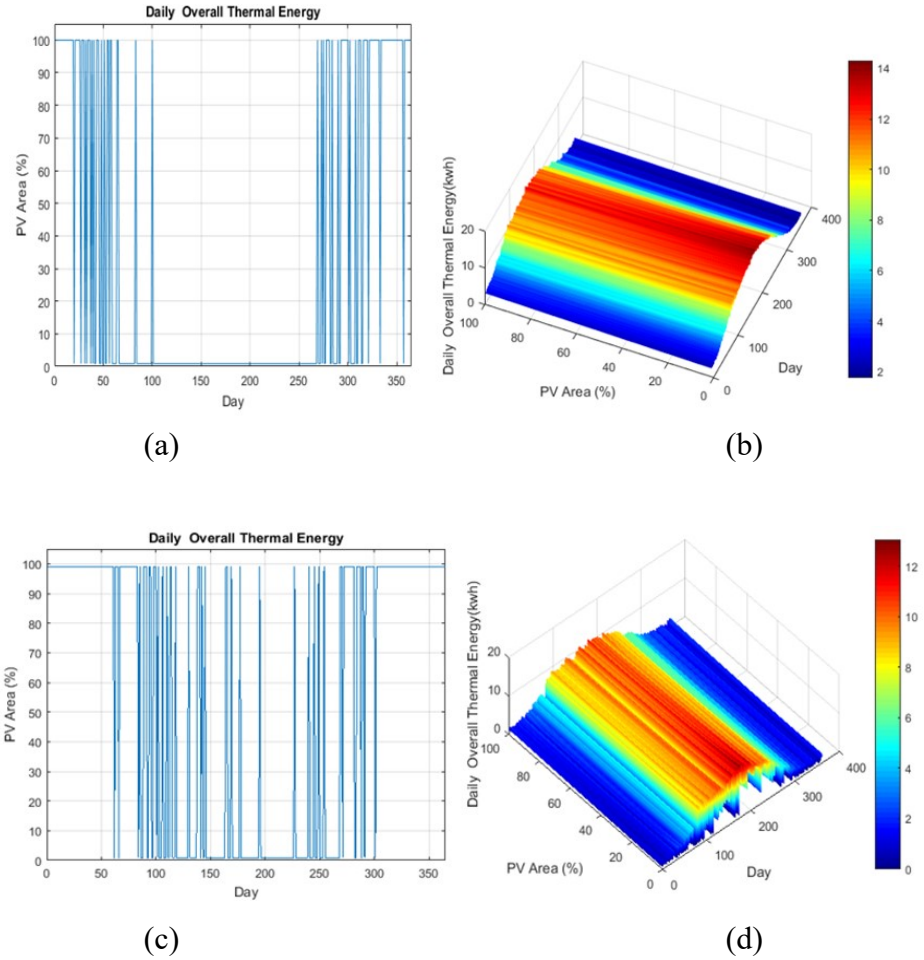

Figure 3-22 Relation between PV coverage area and maximum OTE for: a and b) constant and c and d) variable flow rate values

A larger sample is considered on a monthly basis (meso level). Figure 3-23a shows that the maximum OTE obtained during January, November, and December occurred when the collector was substantially covered with PV modules. In contrast, the maximum OTE

obtained during the rest of the year occurred when the portion covered by PV modules was small for the constant flow rate case. For the variable flow rate case shown in Figure 3-23c, the maximum OTE was obtained when the collector was substantially covered with PV modules during all months of the year except the period between April and September. Figure 3-23b, shows that the range of percentage values yielding the maximum OTE for a constant flow rate is up to 40%. Figure 3-23d shows that for a variable flow rate, the PV coverage area range is up to 20%. The amount of the energy gained is higher in the case of a constant flow rate.

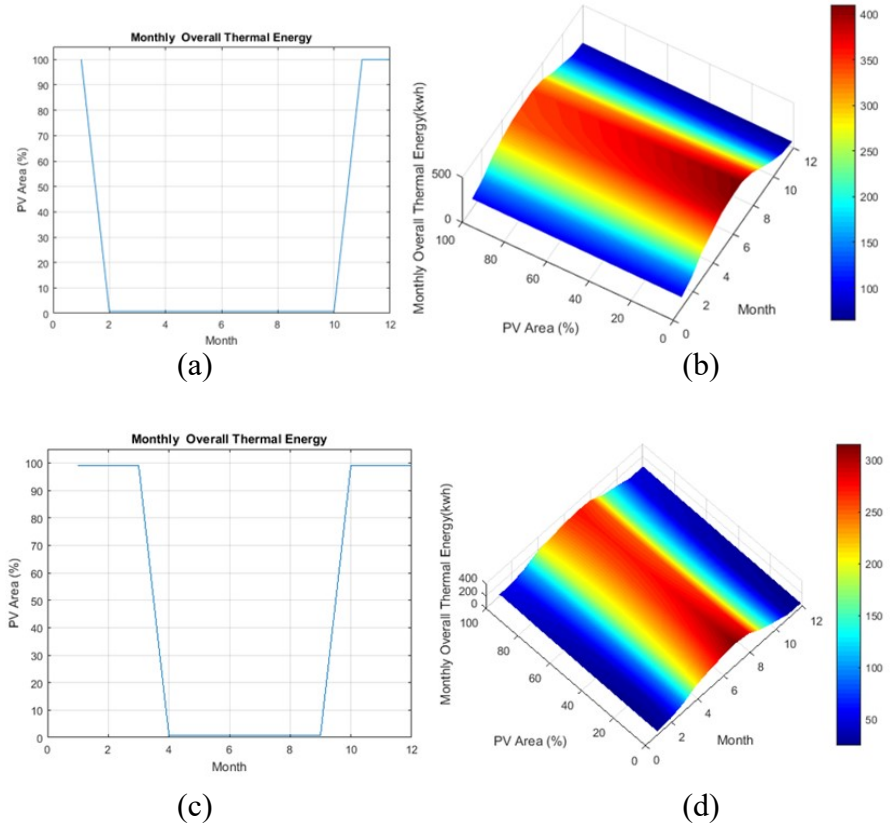

Figure 3-23 Relation between PV coverage area and maximum OTE for monthly change for one year, for constant and variable flow rat values

The relationship between PV coverage area and maximum OTE for each individual month is shown in Figure 3-24 and Figure 3-25, for case one and two consecutively. If a PV

coverage area of 20% is selected, as found in most previous work, the energy levels obtained during January, November and December are not the maximum. When the PV coverage area is around 80%, the maximum OTE is obtained for January, November and December in the case of a constant flow rate, and January, February, March, October, November and December in the case of a variable flow rate. Table 3.1 and Table 3.2 shows the percentage of energy lost with a 20% PV coverage area, as compared to 80%, for constant and variable flow rates.

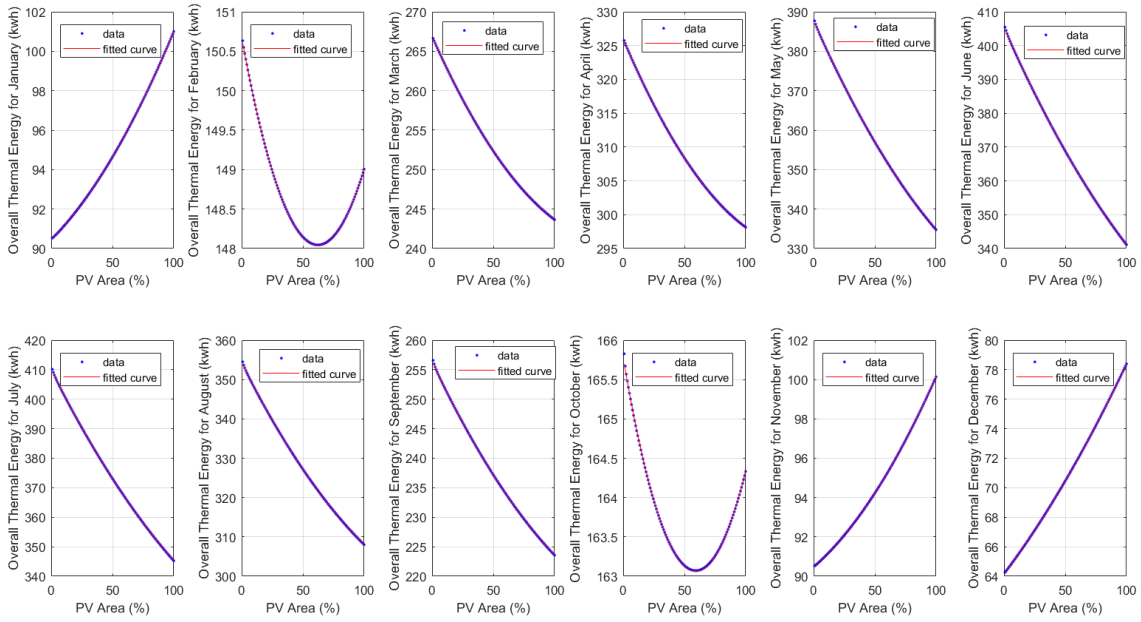

Figure 3-24 Relation between PV coverage area and maximum OTE for a constant flow rate month by month

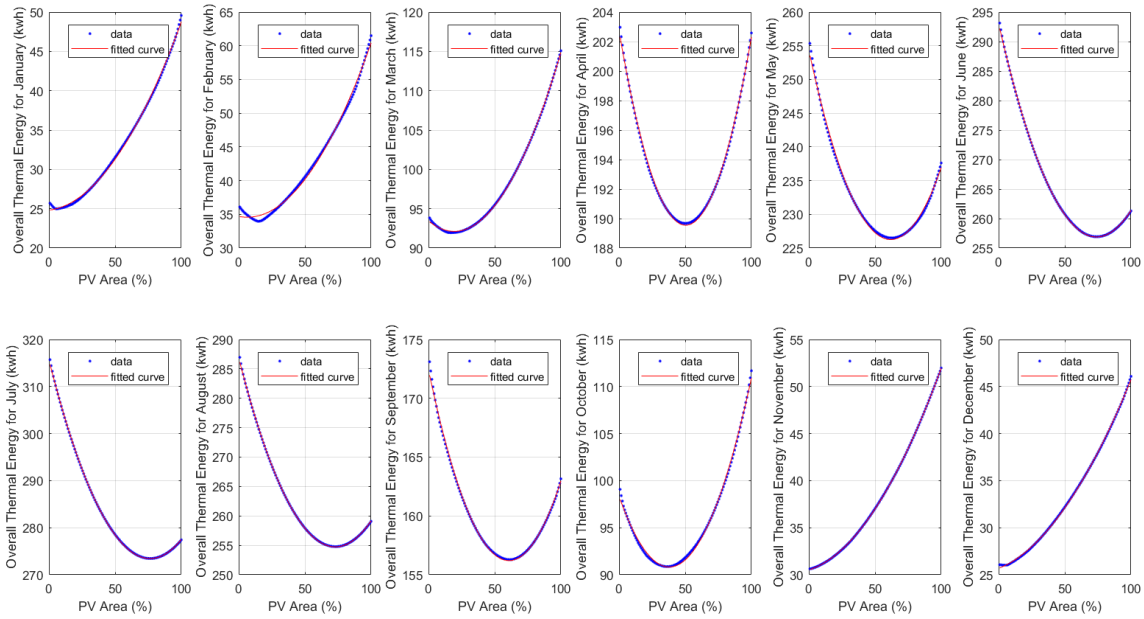

Figure 3-25 Relation between PV coverage area and maximum OTE for a variable flow rate month by month

Table 3.1 The percentage of energy lost with a 20% and 80% PV coverage area, for constant flow rate

	Constant flow rate case		
Month	Energy gained in (kwh)		% of Energy loss
	20% PV coverage	80% PV coverage	
Jan	91.75	98	6.4
Nov	91	97	6.2
Dec	66	75	12

Table 3.2 The percentage of energy lost with a 20% and 80% PV coverage area, for variable flow rate

	Variable flow rate case		
Month	Energy gained in (kwh)		% of Energy loss
	20% PV coverage	80% PV coverage	
Jan	25	40	37.5
Feb	33	50	34
Mar	92	105.5	12.8
Oct	92	100	8
Nov	32	45	28.9
Dec	27	39.5	31.6

It is clear from the previous discussion and from Figure 3-26 that the energy values calculated for a constant flow rate are not the same as those for variable flow rates. Variable flow rates yield more realistic results, because environmental conditions are taken into consideration. It can be seen that the energy gained for a variable flow rate differs from that for a constant flow rate, with same the PV coverage ratio, however the two cases follow a similar pattern.

The annual electrical, thermal, and overall thermal energy for different PV coverage areas, with constant and variable flow rates, are shown in Figure 3-27 and Figure 3-28. With a constant flow rate, the annual thermal energy and annual OTE decrease when the PV coverage area increases, as shown in in Figure 3-27. In contrast, the annual electrical energy increases when the PV coverage area increases. This means that the contribution of thermal energy to the OTE is high in comparison to that of electrical energy.

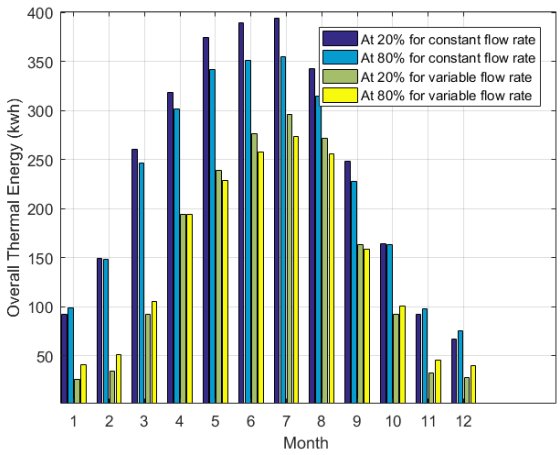

Figure 3-26 Monthly overall thermal energy with 20% and 80% coverage, for constant and variable flow rates

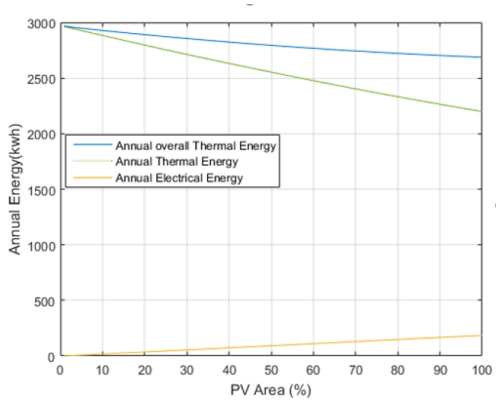

Figure 3-27 Annual electrical, thermal and overall thermal energy with differing PV coverage, for a constant flow rate

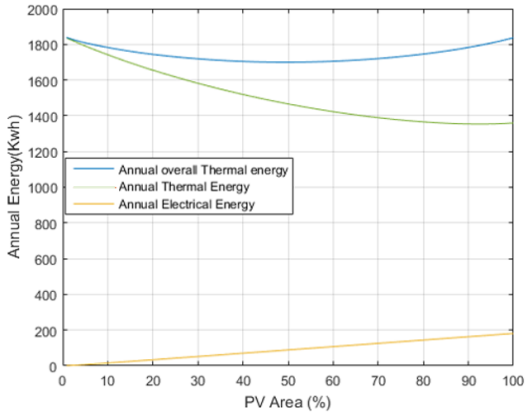

Figure 3-28 Annual electrical, thermal and overall thermal energy with differing PV coverage, for a variable flow rate

The trend of the annual OTE with a variable flow rate, shown in Figure 3-28, differs from that with a constant flow rate. In Figure 3-27, it can be seen that for a variable flow rate, the annual OTE is almost the same for PV coverage areas of 20% and 80%.

The monthly and daily studies are important, because the annual study does not give a complete picture in terms of the OTE. As shown in Table 3.1, the PV coverage area should be adapted monthly to maximize the annual OTE gain. Greater annual energy yields are obtained when different PV coverage ratio values are applied, as opposed to maintaining a fixed ratio throughout the year.

The OTE in different seasons was studied, for constant and variable flow rates. Table 3.3 summarizes different PV coverage area ratios, different time periods. At the micro level, a 80% PV coverage ratio is recommended for January, February, March, October, November, and December for case 1. For the rest of the year, a 20% PV coverage ratio is recommended. For variable flow rates, at the meso level, an 80% PV coverage ratio for fall and winter and a 20% coverage ratio for summer and spring are recommended.

Table 3.3 Percentage of PV coverage ratio for maximum energy at micro and mseo levels, for constant and variable flow rates

Month	Seasons	PV ratio coverage for max thermal energy (%)	
		Case 1	Case 2
Jan	Winter	80	80
Feb		40	80
Mar		20	80
Apr	Spring	20	20
May		20	20
Jun		20	20
Jul	Summer	20	20
Aug		20	20
Sep		20	20
Oct	Fall	40	80
Nov		80	80
Dec		80	80
	Winter		

3.3.3 Performance Model for PV Ratio of PVT

In this study, the PV coverage area ratio for the PVT system is varied from 20% to 80%. The first proposed model is based on the relationship between the PV coverage area ratio and the maximum monthly OTE, for constant and variable flow rates, as given by Figure 3-24 and Figure 3-25. This model is applied for each month of the year. The model inputs are the month and the PV coverage area ratio, and the output is the OTE gained. The proposed model has a second order polynomial equation with three coefficients for all

months, fitting the trend between the PV coverage area and the maximum monthly OTE as follows:

$$Maximum\ \ OTE = a * (PV\ ratio)^2 + b * PV\ ratio + c \tag{3.29}$$

where a, b, and c are the coefficients of the model. They are adapted for each month to reflect the change in weather conditions so as to obtain the maximum OTE. Table 3.4 summarizes different coefficients of the model for each month, for both constant and variable flow rates.

Table 3.4 Coefficient values of the first proposed model, for constant and variable flow rates

Month	Coefficients values					
	Constant flow rate case			Variable flow rate case		
	a	*b*	*c*	*a*	*b*	*c*
Jan	0.0004	0.0619	90.456	0.0022	0.0198	24.842
Feb	0.0007	-0.0845	150.67	0.0030	0.0380	34.696
Mar	0.0012	-0.3492	266.88	0.0035	-0.1362	93.445
Apr	0.0015	-0.4256	325.98	0.0052	-0.5230	202.73
May	0.0017	-0.7019	387.75	0.0073	-0.9075	254.33
Jun	0.0018	-0.8216	405.38	0.0066	-0.9780	293.03
Jul	0.0018	-0.8308	410.00	0.0072	-1.1052	315.62
Aug	0.0016	-0.6240	354.32	0.0060	-0.8814	286.88
Sep	0.0011	-0.4421	256.43	0.0044	-0.5336	172.41
Oct	0.0008	-0.0915	165.78	0.0052	0.39610	98.338
Nov	0.0004	0.0535	90.471	0.0017	0.04470	30.516
Dec	0.0003	0.1097	64.16	0.0014	0.05680	25.669

In Table 3.4, the sign of the b coefficient indicates the behaviour of the model. For example, when the value of the b coefficient is negative, the maximum OTE occurs with a PV

coverage area of 20%. Conversely, when the value of the b coefficient is positive, the corresponding PV coverage area is 80%.

The second model describes the relationship between the PV coverage ratio which generates the maximum OTE, and each month throughout the year. The model input is the month, and the output is the PV coverage ratio. The proposed model is derived by using a Fourier series. It has eleven coefficients, as follows:

$$\begin{aligned} PV\ ratio\ = \ & a_0 + a_1 * cos(xw) + b_1 * sin(xw) + a_2 \\ & * cos(2xw) + b_2 * sin(2xw) + a_3 * cos(3xw) \\ & + b_3 * sin(3xw) + a_4 * cos(4xw) + b_4 \\ & * sin(4xw) + a_5 * cos(5xw) + b_5 * sin(5xw) \end{aligned} \tag{3.30}$$

where x is the month and w is the frequency. The values are adapted for each month to reflect the change in weather conditions and obtain the best choice of PV ratio to maximize the OTE. Table 3.5 summarizes different coefficients of the model for each month, for both constant and variable flow rates.

Figure 3-29 and Figure 3-30 are based on the coefficient values of the second proposed model, for constant and variable flow rates. These figures show the relationship between the PV ratio that generates the maximum OTE and each month of the year, with fitted values. From Figure 3-29 and Figure 3-30, it can be seen that the PV coverage area ratio is weather sensitive, and is like a weather-dependent load model. Moreover, this phenomenon can be generalized to any location where the weather exhibits clear seasonal differences. However, different locations will have different PV ratio values and threshold months where the PV ratio changes from one state to another.

Table 3.5 Coefficient values of the second proposed model, for constant and variable flow rates

Coefficients	Constant flow rate case	Variable flow rate case
a_0	31.28	53.16
a_1	20.14	-36.88
b_1	5.915	-10.83
a_2	15.48	-4.796
b_2	9.951	-3.082
a_3	9.383	8.623
b_3	10.83	9.951
a_4	3.776	2.701
b_4	8.268	5.915
a_5	0.4431	-1.189
b_5	3.082	-8.268
w	0.5712	2.059

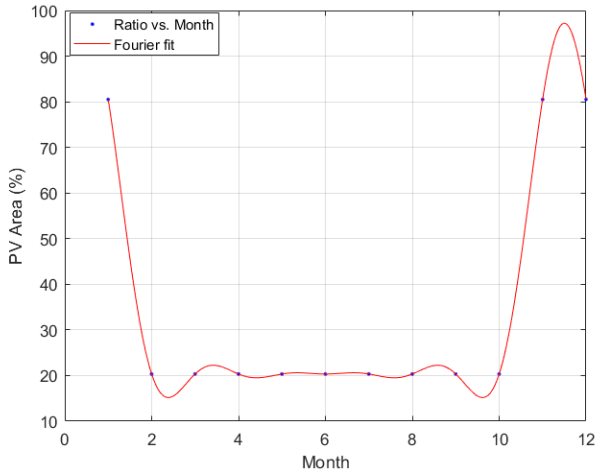

Figure 3-29 Output of the second proposed model compared to actual values, for constant flow rate case

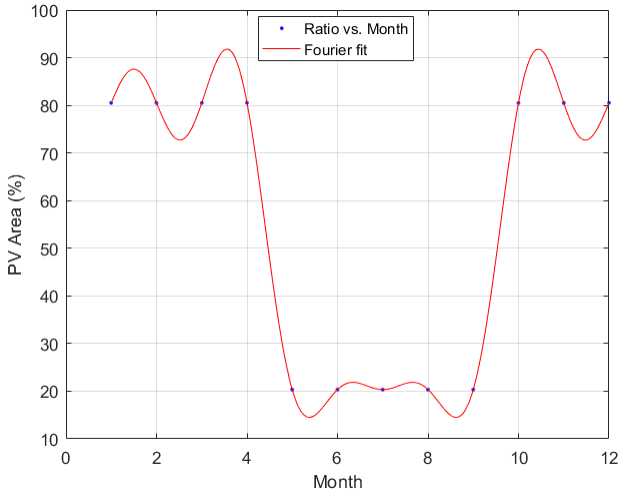

Figure 3-30 Output of the second proposed model compared to actual values, for variable flow rate case

3.3.4 CO_2 Emissions of Photovoltaic Thermal Model

The maximum annual reduction of CO_2 emissions is calculated for case two, for variable flow rates. To obtain the maximum annual reduction in CO_2 emissions, the maximum reduction for each month is taken for different PV coverage areas throughout the year, as shown in Figure 3-31. Hence, variable PV coverage area values are used. These variable PV coverage area values depend on the choice of the optimal PV coverage area size for minimizing CO_2 emissions, based on the available coverage areas. Four different cases are considered for each month. The best 12 cases out of 48 are chosen to minimize CO_2 emissions. The generation of 1 kWh of electricity by a local power plant results in 1.2 kg of CO_2 emissions [83].

Figure 3-31 shows the maximum monthly reduction of CO_2 emissions for different PV coverage area cases. Four cases are used in this study. A maximum reduction in CO_2 emission occurs with a PV coverage area of 80% in January, February and March. A maximum reduction in CO_2 emissions then occurs when the PV coverage area changes

from 80% to 20% during April, and from 20% to 80% during September. This change is carried out due to the environmental conditions discussed above. This indicates the PV coverage area ratio for each month that minimizes CO_2 emissions, as shown in green in Figure 3-31.

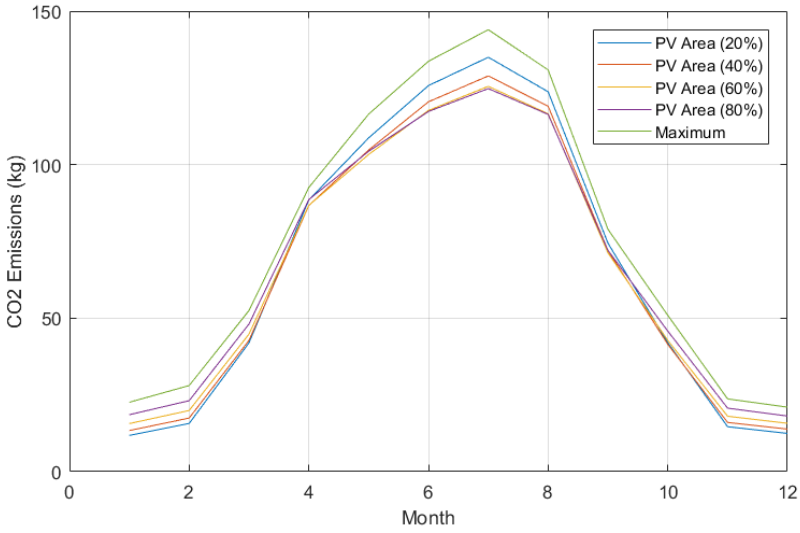

Figure 3-31 Maximum monthly CO_2 emission reductions for different PV coverage areas

The annual reduction in CO_2 emissions for different PV coverage area ratios (20%, 40%, 60%, and 80%) is shown in Figure 3-32. The maximum annual reduction in CO_2 emissions for a fixed PV coverage area occurs when the PV coverage area value is 80% of the PVT (the best scenario) for each month throughout the year. The amount of the reduction is 798 kg. However, by using variable PV coverage areas, the annual reduction of CO_2 emissions can be increased to 850 kg, which is calculated by accumulating the values shown in green in Figure 3-31. For the reduction of CO_2 emissions, the percentage difference between variable PV coverage areas and the best scenario for a fixed PV coverage area is:

$$CO_2\ Emission\ Reduction\ difference\ = \frac{(850-798)}{798} * 100 = 6.54\%$$

This investigation is conducted for a residential load, which is considered a small load. The percentage difference in the reduction of CO_2 emissions (6.54%) will amount to substantial reductions when large-scale systems such as commercial and industrial loads are considered. The increment percentage difference between annual CO_2 emission reductions for a fixed PV coverage area as compared to variable PV coverage areas for one year is shown in in Table 3.6.

Table 3.6 Increment percentage difference for annual CO_2 emission reductions

Case 1 (20%)	Case 2 (40%)	Case 3 (60%)	Case 4 (80%)
6.97 %	9.42%	9.25 %	6.54%

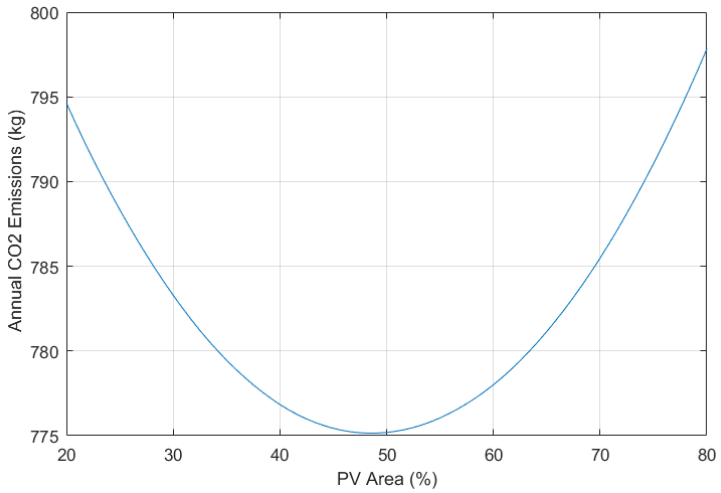

Figure 3-32 Relationship between PV coverage area ratio and annual CO_2 emission reductions in kg

3.3.5 Conclusions

The OTE of PV systems is obtained for cases with constant and variable flow rates. The variable flow rate values used in this study are associated with a thermal system used for water heating. These flow rate values are controlled by a water pump driven by a PV system.

The dataset used in this research was obtained for a North American city. Various environmental conditions such as solar radiation, ambient temperature, wind speed, water flow rate and temperature of input water were measured every minute over a period of a year.

In this work, the PV coverage ratio was varied from 1% to 100% to determine the maximum OTE of a PVT system. While previous work has been done at a macro level with a constant flow rate, here three different time span levels are analyzed: Macro, meso, and micro.

The maximum OTE is obtained at a different PV coverage ratio for each month. This contributes to maximizing the annual energy, as compared to previous work using a constant ratio for the whole year. Flow rates that vary with time are also used in this study, in comparison to constant flow rates studied in previous work. The results show that the PV coverage ratio which produces the maximum OTE for constant and variable flow rate cases differs, especially for the fall and winter seasons. For this reason, a variable flow rate is used, which is more suited to practical applications. Two different models based on two different cases of flow rate values are proposed in this work. The first model analyzes the OTE for each month based on the PV coverage area ratio. The second model obtains the best PV coverage ratio, to generate the optimal monthly OTE for each month.

One aspect of maximizing the OTE is reducing CO_2 emissions. Different PV coverage area values are analyzed to find the optimal case. Then, variable PV coverage area values are obtained for each month. The results show that constant PV coverage area values for a PVT

system during the year are not recommended for minimizing CO_2 emissions. Specific PV coverage area values are proposed for each month to minimize annual CO_2 emissions.

The results show that the optimal PV coverage area is 80% for January, February, October, November, and December and 20% for the rest of the year, to obtain the greatest reduction of CO_2 emissions. The percentage difference in the reduction of CO_2 emissions between the case studied and conventional PV coverage area values are calculated for different scenarios.

The simulated results show that CO_2 emissions can be reduced by an additional 6.54% if variable PV coverage area values for each month are used, in comparison to the best scenario for conventional PV coverage area values. This can result in very substantial emission reductions when large-scale systems are used.

CHAPTER 4 SOLAR RADIATION FORECASTING

In this chapter, a brief overview of different solar radiation forecasting methods is provided, and a review of the literature on solar radiation forecasting is presented [1].

4.1 INTRODUCTION

Today many renewable energy sources, especially solar and wind energy, are integrated with grid systems. As a result, electricity production and consumption can be affected by the intermittency of these sources, causing problems such as fluctuations, and issues related to power quality and stability [84]-[87].

Since the output of solar energy systems depends on solar radiation, forecasting solar radiation is essential for power grid operation and load management. In addition, several meteorological variables, including air temperature, humidity, atmospheric pressure, wind speed and cloud cover, can be measured easily with inexpensive devices, in comparison to solar radiation. On the other hand, missing solar radiation data in weather station databases could be recovered by solar radiation forecasting.

Solar radiation forecasting can be performed in various ways, such as cloud imagery combined with physical models, and artificial intelligence (AI) methods. Artificial intelligence methods used for solar radiation forecasting include artificial neural networks (ANNs), regression, machine learning, fuzzy logic (FL), and various hybrid systems [86], [87]. The performance of these methods depends on the dataset, time steps, and performance indicators [88], [89].

AI is used to find relationships between inputs and outputs, especially for complex problems. AI is used in many applications such as pattern recognition, classification problems, data mining and forecasting problems [90].

The ANN approach is an attractive tool for data analysis and prediction due to nonlinearity functions that have the ability to find relationships between inputs and outputs [91]. In addition, in recent decades, ANN has been used more frequently than other methods, as shown in Figure 4-1 [92].

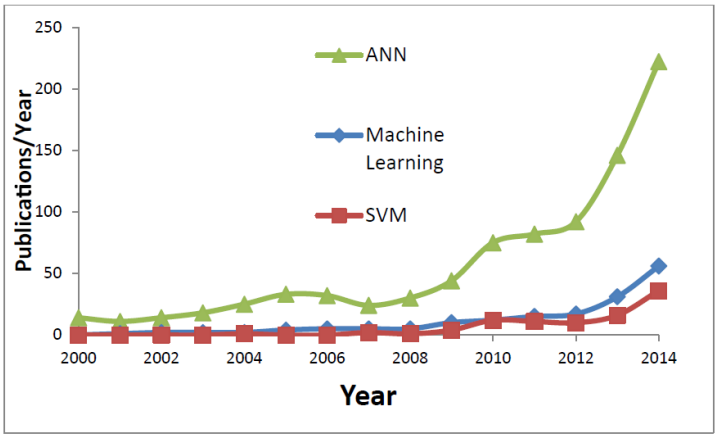

Figure 4-1 Frequency of use of ANN, machine learning and support vector machine (SVM) terms in original research articles [92]

4.2 ARTIFICIAL NEURAL NETWORKS

Artificial neural networks are networks which attempt to simulate the computations performed by neurons in the human brain. The human brain consists of approximately 1011 computing elements referred to as neurons. These neurons are interconnected, forming a very dense, interconnected electrical switching network. Each neuron has numerous inputs from adjacent neurons. A neuron is activated when the summation of these weighted inputs exceeds the neuron activation threshold. The objective of attempting to simulate the

operation of neurons is to achieve a level of computation similar to that performed by the human brain, in achieving tasks such as recognizing objects, understanding speech, and experiential learning. These tasks are not easily performed by modern computers or electrical networks [93].

4.2.1 ANN Applications

Artificial neural networks have a very broad range of applications, including pattern recognition, prediction, optimization, associative memory, control, classification, and function approximation. These ANN applications are discussed below.

- Pattern classification assigns an input pattern such as an audio waveform or image, which can be represented by a feature vector, to a specific, predefined class. The classes and feature vectors are predefined by the neural network designer. Applications of this technique include electroencephalogram (EEG) waveform classification, blood cell classification, and printed circuit board inspection [94].
- Clustering/categorization is used for unsupervised pattern classification. Clustering algorithms detect similarities between patterns, and place similar patterns in a cluster. Applications include data mining, data compression, and exploratory data analysis [94].
- In function approximation, data pairs (input/output) are used as inputs to the neural network, and a function is approximated which represents these data. This has very broad applications, because many engineering and scientific modeling problems require that functions be approximated based on known input/output data pairs [94].

- Predicting/forecasting uses input data pairs (input, output) where the input is time and output a function of time. It is the objective of this to make predictions of what the output will be in the next increment of time. Applications of this include stock market prediction or weather forecasting [94].
- Optimization algorithms attempt to maximize or minimize an objective function so that a number of constraints are met. Optimization problems can be formulated for numerous disciplines. Applications can include economic dispatch, and optimal power flow formulations.
- Content addressable memory permits the recall of content in memory, even if a partial or distorted input is used to access the memory. This is desirable for constructing multimedia information databases [94].

Classification is a significant application of neural networks. First raw data are measured, then these data are converted into a pattern, features are extracted from this pattern, and finally, based on these features, a classification is made. A general classifier is illustrated in Figure 4-2.

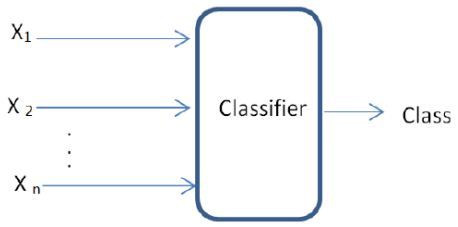

Figure 4-2 Block diagram of a classifier

To distinguish one pattern from another, a decision surface must be created which separates the two distinctly different patterns. This can be done by using discrimination functions. There are as many discrimination functions as there are classes which must be

distinguished. Each discrimination function is chosen so that for each class, a unique discrimination function yields a maximum value in the pattern space where that class exists. Thus, determining which discrimination function yields the largest value at a certain point in the pattern space will determine the class at that point. Classifiers can be designed in two ways, by designing discrimination functions, or by teaching the network. Designing discrimination functions can be quite cumbersome if the network is large. This makes the ability to train a network very valuable. With pre-knowledge of certain patterns and their corresponding classes, the network can be trained to recognize these patterns. This permits an iterative network training process, where the discrimination functions are evaluated. In the training process, all the patterns must be recycled iteratively, until they are all classified correctly. This form of classification thus requires supervised learning. Linearly separable classes require only a single layer of neurons, whereas nonlinearly separable classes require multiple layers of neurons.

4.2.2 Artificial Neural Network Structure

A model for an artificial neuron could be created by understanding neuron operation. Figure 4-3 provides a general network diagram for a single artificial neuron.

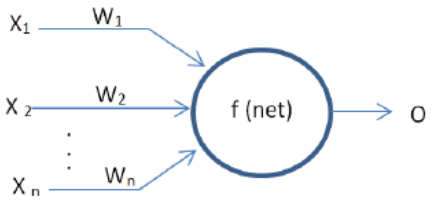

Figure 4-3 McCulloch-Pitts neuron model

This is the McCulloch-Pitts model for a neuron. The weights correspond to the adjacent neuron interconnections, the inputs represent the excitation coming from the adjacent

neurons, and the node corresponds to the neuron processing. The node processes the weighted summation of f(*wx*). This activation function determines if the neuron will activate or not based on the adjacent neurons weighted inputs. This activation function, f(*wx*), can be either discrete or continuous with x. Bipolar and Unipolar discrete and continuous activation functions are four types of functions commonly used in neural network design. These four activation functions are shown below in Figure 4-4.

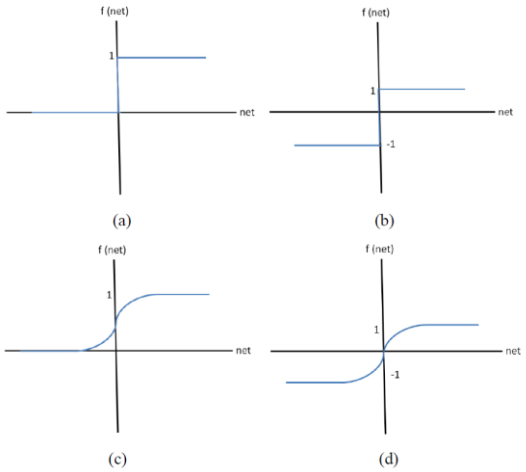

Figure 4-4 (a) Discrete Unipolar (b) Discrete Bipolar (c) Continuous Unipolar (d) Continuous Bipolar

There are two main categories of ANN: single-layer and multi-layer neural network.

4.2.2.1 Single layer Neural Network

A single-layer neural network (SLNN) consists of one layer of neurons, as shown in Figure 4-5 which is similar to the main ANN structure.

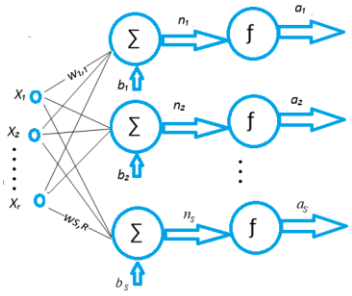

Figure 4-5 Single layer neural network

4.2.2.2 Multilayer Neural Networks

Multilayer feed-forward networks are neural networks that have an input, output, and hidden layers. The hidden layers permit more complex operations. For example, in the case of classification, they permit the classification of linearly non-separable objects. The network diagram for a multilayer neural network is shown in Figure 4-6.

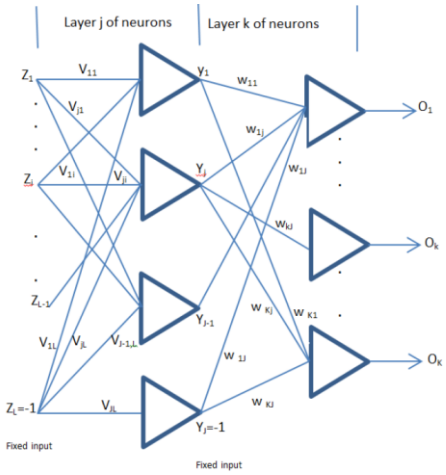

Figure 4-6 Multilayer neural network

The output from each layer is effectively mapping the previous input into a new domain. For example, the multiple layers can bring linearly non-separable objects and transfer it into a domain in which they become linearly separable. These neural networks again could be trained. For multilayer neural networks, the weighting coefficients in each layer can be varied in such a way that the global cascaded error is minimized.

4.2.3 ANN Learning Algorithm

Finding an error in the output and back propagating it through the neuron layers permits computation of the error in the corresponding layer. This allows adjustment of the weights so that the error is minimized. This training can be achieved by using the delta learning rule. It can also be performed with both continuous and discrete neuron activation functions. There are several issues involved in designing a feed-forward network. These include the required number of layers, the number of neurons per layer, how the network will perform with data that is not training data, and how large a training set should be. In practice, these parameters are found via a trial-and-error method. There are only loose guidelines for the selection of the parameters. There are several variants of a feed-forward neural network: Radial basis function networks, Kohonen self-organizing maps, adaptive resonance theory models, and Hopfield networks. These variants are discussed below.

Radial basis function networks are two-layer neural networks. The hidden layer of these networks employs radial basis functions as neuron activation functions. The Gaussian kernel is an example of a basis function that is commonly used. The positions and widths of the kernels are learned from the training patterns. In general, there are fewer kernels than training patterns. This approach can be used for function approximation. This is similar to the way the Fourier series approximates functions through a combination of basis functions. Typically, the learning algorithm for these networks requires fewer iterations to achieve the result. However, these networks often contain many hidden neurons, leading to longer run times [94].

Because they can be trained, neural networks are extremely flexible in their use. The training allows for adjustment of the weights, so that a desired output is achieved. There

are two main types of learning, supervised and unsupervised. Supervised learning is used when the desired output is known and provided to the system by the teacher. A comparison is made between the desired output and the network output. The error between the actual and desired outputs is used to adjust the network weights, so that the desired output is achieved by the network. Unsupervised learning is used when the desired output is unknown, and the network must learn to adjust the weights based on its responses to inputs. From these two learning philosophies, various algorithms can be created to train a neural network. Table 4.1 summarizes common learning algorithms used in neural network design [93].

Table 4.1 Summary of ANN learning algorithms [93]

Learning Rule	Weight Adjustment	Learning	Initial Weight	Activation Function
Perceptron	$c[d_i - sgn({w_i}^t x)]x_j$ $j = 1,2,\dots,n$	Supervised	Any	Discrete
Delta	$c(d_i - o_i)f'({w_i}^t x)x_j$ $j = 1,2,\dots,n$	Supervised	Any	Continuous
Widrow-Hoff	$c(d_i - {w_i}^t x)x_j$ $j = 1,2,\dots,n$	Supervised	Any	Discrete or Continuous
Outstar	$\beta(d_i - w_{ij})$ $i = 1,2,\dots,p$ For a layer of p neurons	Supervised	0	Continuous
Correlation	$cd_i x_j$ $j = 1,2,\dots,n$	Supervised	0	Discrete or Continuous
Hebbian	$co_i x_j$ $j = 1,2,\dots,n$	Unsupervised	0	Discrete or Continuous
Winner-take-all	$\alpha(x_j - w_{mj})$ $j = 1,2,\dots,n$ m is the winning neuron	Unsupervised	Random	Continuous

The values of c, α, and β are the learning constants. These constants are chosen by the designer during the design of a neural network.

4.3 WAVELET NEURAL NETWORKS

4.3.1 Wavelet Neural Network Structure

Wavelet neural networks (WNNs) have capabilities like those of ANNs, but use different activation functions in the hidden layer. Due to localized wavelet activation functions, WNNs have a more compact topology and faster learning speed than is the case with ANNs [95], [96]. WNNs are like feed-forward neural networks with one hidden layer, as shown in Figure 4-7. As proposed by Q. Zhang in 1992 [97], WNNs replace the sigmoid activation function with a wavelet function as the activation function.

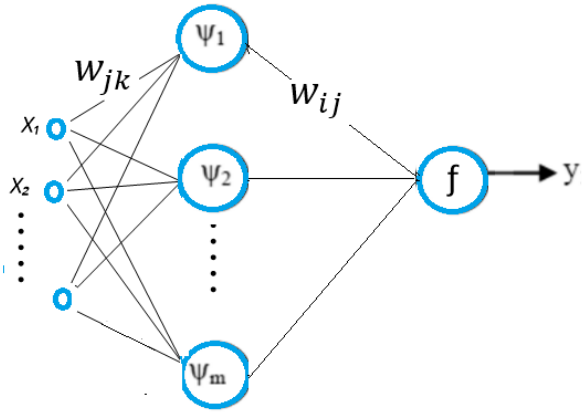

Figure 4-7 Multilayer WNN

The input layer consists of M nodes and the output layer consists of one neuron. The output is represented by the sum of weighted wavelets. w_{jk} represents the weight between the hidden unit j and input unit k, and w_{ij} represents the weight between the output and hidden unit j. The net of each hidden neuron j at time n is given by [97]

$$f_j(n) = \sum_{k=0}^{k=m} w_{jk}(n) * x_k(n) \tag{4.1}$$

where $f_j(n)$ is the sum of weighted inputs to the j^{th} hidden neuron, $x_k(n)$ is the k^{th} input. The output of each hidden neuron is given by [97]

$$\psi_{a,b}(f_j(n)) = \psi[(f_j(n) - b_j(n))/a_j(n)] \tag{4.2}$$

where ψ is the wavelet function, $a_j(n)$ represents the scaling, and $b_j(n)$ is the translation coefficients of the wavelet function for the hidden neuron. The input $f(n)$ and output $y(n)$ of the output neuron are given by [97]

$$f(n) = \sum_{k=0}^{k=m} w_{ij}(n) * \psi_{a,b}(f_j(n)) \tag{4.3}$$

$$y(n) = \sigma[f(n)] \tag{4.4}$$

4.3.2 WNN Learning Algorithm

The connection weights between the input, hidden and output layers of WNN, and the parameters of the wavelet function for the hidden neuron are adjusted with a gradient method, by finding the minimum sum square error. The sum square error at time n is given by [98]

$$E(n) = \frac{1}{2} e^2(n) = \frac{1}{2} [\hat{y}(n) - \mathrm{y}(n)]^2 \tag{4.5}$$

where $\hat{y}(n)$ is the predicted output, $\mathrm{y}(n)$ is the observed data.

The weights w_{jk}, w_{ij} and the wavelet function parameter are updated by [98]

$$w_{jk}(n+1) = w_{jk}(n) + \Delta w_{jk}(n+1) \tag{4.6}$$

$$w_{ij}(n+1) = w_{ij}(n) + \Delta w_{ij}(n+1) \tag{4.7}$$

$$a_j(n+1) = a_j(n) + \Delta a_j(n+1) \tag{4.8}$$

$$b_j(n+1) = b_j(n) + \Delta b_j(n+1) \tag{4.9}$$

where $\Delta w_{jk}(n+1)$, $\Delta w_{ij}(n+1)$, $\Delta a_j(n+1)$ and $\Delta b_j(n+1)$ are obtained by [98]

$$\Delta w_{jk}(n+1) = -\eta * \frac{\partial E(n)}{\partial w_{jk}(n)} \tag{4.10}$$

$$\Delta w_{ij}(n+1) = -\eta * \frac{\partial E(n)}{\partial w_{ij}(n)} \tag{4.11}$$

$$\Delta a_j(n+1) = -\eta * \frac{\partial E(n)}{\partial a_j(n)} \tag{4.12}$$

$$\Delta b_j(n+1) = -\eta * \frac{\partial E(n)}{\partial b_j(n)} \tag{4.13}$$

where η is the learning rate which is determined using various values that minimize the error.

4.3.3 WNN Wavelet Functions

Different wavelet functions are used as activation functions in the hidden layer, as shown in Table 4.2 [98].

Table 4.2 Summary of neural network learning algorithms [98]

Wavelet functions	Formula
Haar wavelet function	$\psi\left(f_j(n)\right) = \begin{cases} 1, & 0 \le f_j(n) < 0.5 \\ -1, & 0.5 \le f_j(n) \le 1 \\ 0, & other \end{cases}$
Gaussian wavelet function	$\psi\left(f_j(n)\right) = \frac{f_j(n)}{\sqrt{2\pi}} \exp(\frac{-t^2}{2})$
Mexican Hat wavelet function	$\psi\left(f_j(n)\right) = \frac{2}{\sqrt{3}} \pi^{-0.25} (1 - \left(f_j(n)\right)^2) \exp(\frac{-t^2}{2})$
Morlet wavelet function	$\psi\left(f_j(n)\right) = \cos(1.75 f_j(n)) \exp(\frac{-t^2}{2})$

4.4 EVALUATION OF MODEL PERFORMANCE

It is difficult to compare different ANN models for many reasons, including different forecast time horizons, the time scale of the predicted data, and differing meteorological conditions at each site [92].

Comparisons between ANN models are based on the error between the predicted and observed data. Many statistical error concepts, such as the mean absolute percentage error (*MAPE*), mean percentage error (*MPE*), mean bias error (*MBE*), mean square error (MSE), root mean square error (*RMSE*), normalized root mean square error (*nRMSE*), Pearson coefficient (R), and coefficient of determination (R^2) are widely used to evaluate the accuracy of ANN models, and are given by [92]

$$MBE = \frac{1}{N} \sum_{i=1}^{N} (\hat{y}(i) - y(i)) \tag{4.14}$$

$$MAE = \frac{1}{N}\sum_{i=1}^{N}|\hat{y}(i) - y(i)| \tag{4.15}$$

$$MAPE = \frac{1}{N}\sum_{i=1}^{N}|\frac{\hat{y}(i) - y(i)}{y(i)}| \tag{4.16}$$

$$MSE = \frac{1}{N}\sum_{i=1}^{N}(\hat{y}(i) - y(i))^2 \tag{4.17}$$

$$RMSE = \sqrt{MSE} = \sqrt{\frac{1}{N}\sum_{i=1}^{N}(\hat{y}(i) - y(i))^2} \tag{4.18}$$

$$nRMSE = \frac{\sqrt{\frac{1}{N}\sum_{i=1}^{N}(\hat{y}(i) - y(i))^2}}{\bar{y}} \tag{4.19}$$

where N is number of observations, y is actual value, $\hat{y}$ is predicted value and $\bar{y}$ is mean of observed data.

nRMSE and R^2 are used to evaluate each solar radiation forecasting model. *nRMSE* is used to show the difference between the actual and predicted data, and to determine the goodness of fit of the model. R^2 shows the relationship between the measured and predicted values.

4.5 LITERATURE REVIEW

Several meteorological and geographical variables have been used as ANN model inputs for solar radiation prediction. These include maximum temperature (T_{max}), average temperature (T_{avg}), relative humidity (hu), wind speed (W_s), sunshine duration (d_s), cloud cover (cc), latitude (L_{al}), longitude (L_{lo}), and altitude (L_{al}) [99]. Hourly and daily global solar radiation (GSR_H, GSR_D) predictions are carried out in this research.

As mentioned previously, numerous researchers have used ANN techniques for solar energy forecasting. The ANN model proposed by Moustris et al. (2008) [100] uses latitude, longitude, altitude, sunshine hours, cloud cover, hourly air temperature data, and relative humidity data as inputs. This model was used to predict hourly global and diffuse solar radiation for different locations in Greece. The model was trained in warm and cold seasons by using a back-propagation learning algorithm. Average R was used to evaluate the performance of the model, and was found to be 0.99, 0.98 and 0.7 for the maximum, average, and minimum GSR_H, radiation, respectively.

Another ANN model, proposed by Alam et al. (2009) [101], used latitude, longitude, altitude, time, months of the year, air temperature, relative humidity, rainfall, wind speed, and net long wavelength data as inputs. Different combinations of inputs were evaluated. The models estimated the hourly and daily diffuse solar radiation for 10 different locations in India, and used three feed-forward layers, with a back-propagation algorithm. The coefficient of determination R^2 and n*RMSE* were used to evaluate the performance of the model, and were 0.85 and 8.8% respectively, for hourly diffuse solar radiation.

An ANN model proposed by Mellit et al. (2010) [102] used hourly solar irradiance, air temperature, and hours as inputs. The model predicted solar radiation 24 hours in advance for the city of Trieste, Italy. The model consists of four layers, and uses multilayer perceptron (MLP) feed-forward, with a back-propagation training algorithm and different numbers of neurons. n*RMSE* and *R* were used to evaluate the performance of the model. *nRMSE* values were from 13% to 67% for sunny days, and from 54% to 85% for cloudy days. R values were from 98% and 99% for sunny days, and from 94% to 96% for cloudy days.

Another ANN model was proposed by Deng et al. (2010) [103]. This model used latitude, longitude, altitude, sunshine duration, air temperature, rainfall, relative humidity, atmospheric pressure, and day of the year as inputs, with twelve different combinations of inputs. The model was used to estimate the daily solar radiation for different locations in China. This model consists of three layers of feed-forward neural network, with a back-propagation training algorithm and different numbers of neurons for each layer. It was found that sunshine duration was the most significant variable, and that using all input variables yielded the best results. *RMSE* and R^2 were used to evaluate the performance of the model, and were 1.915 MJ/m^2 and 93% respectively.

Another ANN model was proposed by Wang et al. (2011) [104]. It used diffused radiation, temperature, relative humidity, and time as inputs. This model was used for short-term solar radiation prediction in Golden, CO, USA. Different combinations of ANN layers and neurons were evaluated. The best model was found to be ANN with four layers, with 24, 18, 13 and 24 neurons, respectively. n*RMSE* and R^2were used to evaluate the performance of the model, and were 4.5% and 96.4% respectively.

Another ANN model was proposed by Angela et al. (2011) [105]. It used sunshine duration as an input. This model was used to estimate the monthly average daily global solar radiation in Kampala, Uganda, and used feed-forward back propagation neural networks. Different numbers of neurons were tested. It was found that the best model had one hidden layer with 65 neurons. n*RMSE* and R^2 were used to evaluate the performance of the model, and were 52.1% and 96.3% respectively.

Another ANN model was proposed by Rani et al. (2012) [106]. This model used temperature, humidity, and the day and month of the year as inputs. The model was used to estimate the daily global solar radiation under clear skies in India, and used a back-propagation feed-forward neural network. Different combinations of ANN inputs and layers were evaluated. The best model was found to consist of three layers, with 10 neurons in the hidden layer. In addition, the model which used all the variables performed a better estimation of solar radiation. *MAPE* was used to evaluate the performance of the model, and was 9.175%.

A back propagation neural network was proposed by Hasni et al. (2012) [107]. This model used the month, day, hour, temperature and relative humidity values as inputs. The model was used to predict hourly solar radiation in Algeria. The model exhibited good results in terms of *nRMSE*, *MAE* and R^2 which were 17.20%, 2.9971 and 99% respectively.

Another ANN model was proposed by Alharbi, et al. (2013) [108]. It used temperature, humidity, and a daily date code as inputs. The model was used to estimate daily global solar radiation in Riyadh, Saudi Arabia, and used a back-propagation feed-forward neural network. Different combinations of ANN inputs were tested. The best model was found to consist of three layers, with 80 neurons in the hidden layer. In addition, the model which used all the variables performed a better estimation of solar radiation. *nRMSE* and *R* were used to evaluate the performance of the model, and were 7.5% and 98.6% respectively.

Another ANN model was proposed by Bader, et al. (2014) [109]. It used cloud cover, relative humidity, air temperature, wind speed, wind direction, pressure and vapor as inputs. This model was used to estimate average daily global solar radiation in Riyadh,

Saudi Arabia, and used a back-propagation feed-forward neural network. Different combinations of ANN inputs and numbers of neurons for the hidden layer were tested. The best model was found to consist of three layers, with 75 neurons in the hidden layer. In addition, the model that used the combination of variables air temperature, humidity, and the day performed a better estimation of daily solar radiation. *nRMSE,* R^2 and *MAPE* were used to evaluate the performance of the model, and were 4.75%, 98.02%, and 3.66% respectively.

Shaddel, et al. (2016) [110] used ANN with a back-propagation feed-forward perceptron net, with Levenberg-Marquardt (LM) as the learning algorithm. Four variables, the declination angle, extraterrestrial solar radiation, solar altitude angle, and solar horizontal radiation, were used as inputs. This model was used to estimate hourly global solar radiation on tilted absorbers in Mashhad, Iran. The metrics R^2, *MAE*, and *nRMSE* were used to evaluate the performance of the model for 45 tilted planes, and were 93.02%, 0.0269, and 5.49% respectively.

A three-layer feed-forward back propagation artificial neural network (BP-ANN) model with a LM training algorithm was used by Maamar, et al. (2017) [111] to predict solar radiation on tilted surfaces. The variables used as inputs for the model were the latitude of the site, mean temperature, relative humidity, Angstrom coefficient, extraterrestrial solar radiation, solar radiation data measured on horizontal surfaces (SRH), and solar zenith angle. The best model was found to have 5 inputs, 35 neurons for the hidden layer, and 1 neuron for the output layer. *RMSE* and R^2were used to evaluate the performance of the model, and were 5.75 wh/m^2 and 99.12% respectively.

Two different ANN structures were designed by Masoud, et al. (2017) [112]. Both structures used MLP-ANN to predict total daily solar radiation in Tehran, Iran. Different numbers of input parameters, numbers of neurons, layers and functions were tested to obtain optimal structures. The air temperature, wind speed, and particulate matter in the air were used as inputs for the models. *nRMSE*, and R^2 were used to evaluate the model performance, and were 5% and 99% respectively.

4.6 SOLAR RADIATION FORECASTING VIA NEURAL NETWORKS

A global solar radiation (GSR) model was simulated with the aid of artificial neural network (ANN) and wavelet neural network (WNN) modeling in *MATLA* B^{TM}. For this study, the data inputs for the GSR prediction model were the ambient temperature, relative humidity, cloud cover, wind speed, time of day in hours (1 to 24), and day of the year (1 to 365). The data were recorded in Halifax, Nova Scotia, Canada, between 2000 and 2005. This type of dataset was selected due to the widespread availability on weather websites of such measurements, which are commonly used as inputs for GSR predictions for different locations. For this study, hourly and daily GSR (GSR_H and GSR_D) were predicted from the models [1].

In the first step, different GSR prediction models were evaluated by using different combinations of weather variables as inputs. In the second step, weather variables were selected that led to the best GSR predictions. In the third step, three proposed GSR models were constructed by using the weather variables that led to the best GSR predictions. Finally, the proposed models were compared with other work related to this field, as shown in Figure 4-8.

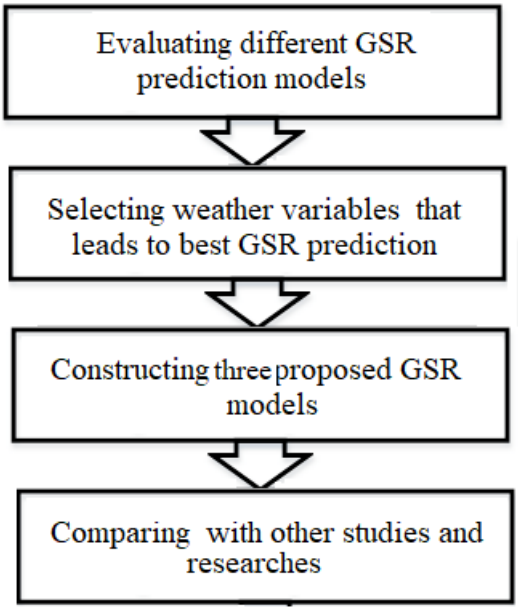

Figure 4-8 Flowchart for constructing the proposed GSR prediction models

4.6.1 Effect of Weather Variables on GSR Prediction

Different GSR prediction models were evaluated by using different combinations of weather variables as inputs. At the beginning, individual weather variables were selected with the day (D) (1-365) as inputs to predict GSR_D, and with hours (h) (1-24) and the day (D) to predict GSR_H, as shown in Figure 4-9.Hourly weather data were used for GSR_H predictions, and average daily weather data were used for GSR_D predictions. These models consist of three layers: The input, hidden, and output layers.

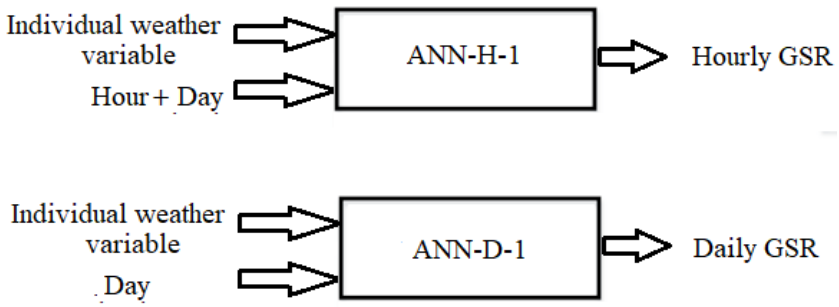

Figure 4-9 ANN-1 model structure

Twelve different combinations of transfer functions for each hidden layer and output layer, twelve different combinations of training functions, and different numbers of neurons were used for each model. This yielded 13824 results in total for each case, for GSR_H and GSR_D. The best GSR_H and GSR_D results for each case with an individual weather variable were selected based on *nRMSE* and adjusted R^2(adj- R^2), as shown in Table 4.3. The value of adj- $R^2$is very close to R^2, due to the large number of samples. The predicted GSR_H and GSR_D were compared with measured GSR_H and GSR_D values for 2005, as shown Figure 4-10 and Figure 4-11 respectively, to find the best predicted GSR_H (ANN-H-1.1) and GSR_D (ANN-D-1.1). In addition, Figure 4-12 and Figure 4-13 illustrate the fit between the predicted GSR_H and $GSR_D$and the actual measured GSR_H and GSR_Dvalues. Different curve- fitting models are determined as shown in Figure 4-12 and Figure 4-13. All curve fitting models are approximately identical and have same R^2 value for GSR_H and GSR_D cases. The curve fitting models and their equation are given in Table 4.4 and Table 4.5. For simplicity, Polynomial of first degree equation is chosen for all GSR_H and GSR_D cases.

Table 4.3 Performance of GSR_H and GSR_D prediction, with one weather variable

	GSR_H				
Model	Input	Neuron	$nRMSE(\%)$	R^2	adj-R^2
ANN-H-1.1	D, h, cc	125	31.124	0.84157	0.84154
ANN-H-1.2	D, h, hu	100	38.058	0.77729	0.77725
ANN-H-1.3	D, h, T	150	42.293	0.72659	0.72654
ANN-H-1.4	D, h, w_s	150	44.134	0.71708	0.71702
	GSR_D				
Model	Input	Neuron	$nRMSE(\%)$	R^2	adj-R^2
ANN-D-1.1	D, cc	125	16.114	0.91258	0.91254
ANN-D-1.2	D, hu	25	19.143	0.88702	0.88697
ANN-D-1.3	D, T	150	30.564	0.76612	0.76601
ANN-D-1.4	D, w_s	150	31.578	0.74841	0.74829

As shown in Table 4.3, *cc* (cloud cover), *hu* (relative humidity), and *T* (air temperature) were found to be the best individual weather variables to use as inputs for both GSR_H and GSR_D prediction. These variables were selected based on lower *nRMSE* and higher *adj-* R^2 values. These inputs are the dominating weather variables that affect the GSR prediction process for this location. The evaluation showed that the ANN models performed better for GSR_H and GSR_D prediction.

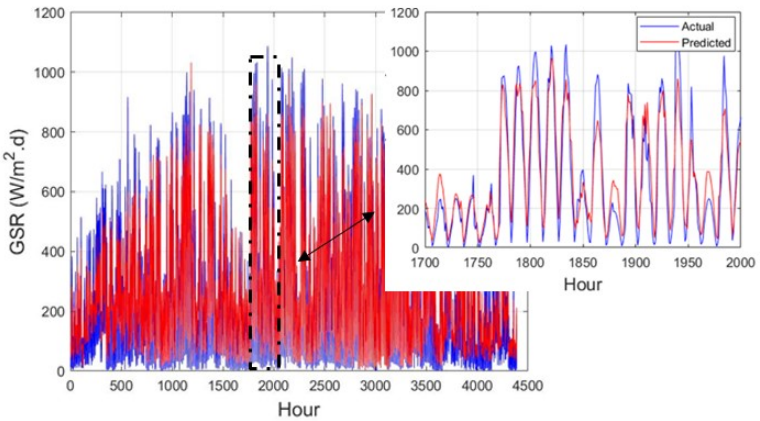

Figure 4-10 Actual and predicted GSR_H values for 2005, for ANN-H-1.1

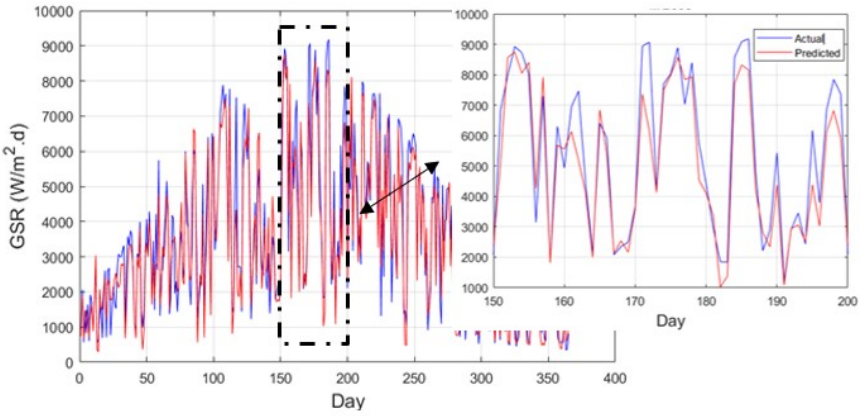

Figure 4-11 Actual and predicted GSR_D values for 2005, for ANN-D-1.1

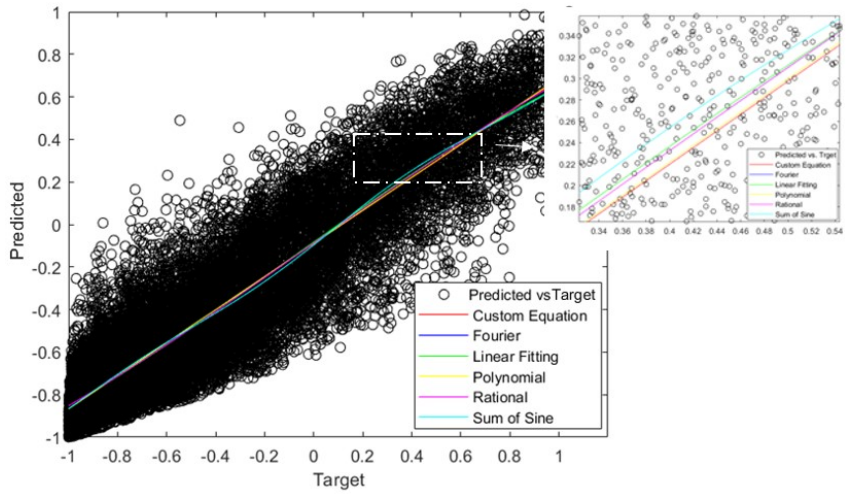

Figure 4-12 The fit between actual and predicted GSR_H values for 2005, for ANN-H-1.1

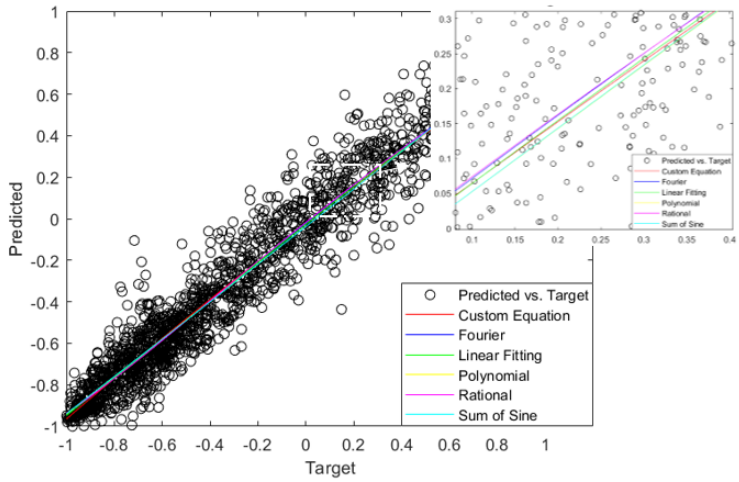

Figure 4-13 The Fit between actual and predicted GSR_D values for 2005, for ANN-D-1.1

Table 4.4 Equation of fitted curves for different models for ANN-H-1.1

Curve-Fitting model	Equation of fitted curve	Coefficient values		
Custom Equation	$a * \exp(-bx) + c$	a= -159.5	b= 0.00486	c= 159.4
Fourier	$a_0 + a_1\cos(xw) + b_0\sin(wx)$	a_0=0.112 a_1=0.02463	b_0=1.337	w=0.6056
Linear Fitting	$a(sin(x - pi)) + b((x - 10)^2) + c$	a= -0.4294	b= -0.0194	c= 1.86
Polynomial	$ax + b$	a= 0.7778	b= -0.08916	
Rational	$\frac{(a_1x + a_2)}{(x^2 + b_1x + b_2)}$	a_1=12.65 a_2=-1.369	b_1= 0.1833 b_2=15.630	
Sum of Sine	$a * \sin(bx + c)$	a= 1.704	b= 0.4712	c= -0.0537

Table 4.5 Equation of fitted curves for different models for ANN-D-1.1

Curve-Fitting model	Equation of fitted curve	Coefficient values		
Custom Equation	$a * \exp(-bx) + c$	a= -8.782	b=0.1017	c= 8.758
Fourier	$a_0 + a_1\cos(xw) + b_0\sin(wx)$	a_0= -0.344 a_1=0.3242	b_0=1.543	w=0.6056
Linear Fitting	$a(sin(x - pi)) + b((x - 10)^2) + c$	a= -0.1808	b= -0.0366	c= 3.636
Polynomial	$ax + b$	a= 0.9033	b= -0.03762	
Rational	$\frac{(a_1x^2 + a_2x + a_3)}{(x^2 + b_1x + b_2)}$	a_1=4.116 a_2=9.891 a_3=-0.186	b_1= 5.479 b_2=10.84	
Sum of Sine	$a * \sin(bx + c)$	a= 5.425	b= 0.167	c= -0.0069

In the next step, as shown in Figure 4-14, different combinations of two of the weather variables *hu*, *cc* and *T* were used with *h* and *D* as inputs for GSR_H and GSR_D prediction. For each case, as shown in Table 4.6, the best results for two weather variables with *h* and *D* were selected, based on *nRMSE* and *adj-* R^2. The predicted GSR_H and GSR_D were compared with the measured values for 2005, as shown in Figure 4-15 and Figure 4-16

respectively, to find the best predicted GSR_H (ANN-H-2.1) and GSR_D (ANN-D-2.1). Figure 4-17 and Figure 4-18 show the fit between the predicted and actual measured GSR.

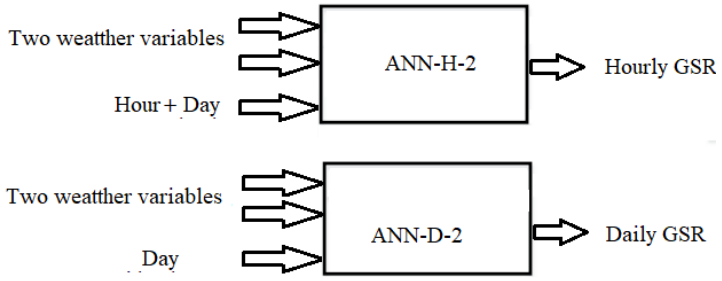

Figure 4-14 ANN-2 model structure

Table 4.6 Performance of GSR_H and GSR_D prediction, with two weather variables

	GSR_H				
Model	**Input**	**Neuron**	$nRMSE(\%)$	R^2	adj-R^2
ANN-H-2.1	D, h, cc, hu	100	26.185	0.87885	0.87883
ANN-H-2.2	D, h, T, hu	150	27.549	0.8685	0.86848
ANN-H-2.3	D, h, T, cc	50	28.089	0.86303	0.86301
	GSR_D				
Model	**Input**	**Neuron**	$nRMSE(\%)$	R^2	adj-R^2
ANN-D-2.1	D, cc, hu	100	10.61	0.94468	0.94467
ANN-D-1.1	D, T, cc	150	12.679	0.9347	0.93468
ANN-D-1.1	D, T, hu	25	14.91	0.92218	0.92215

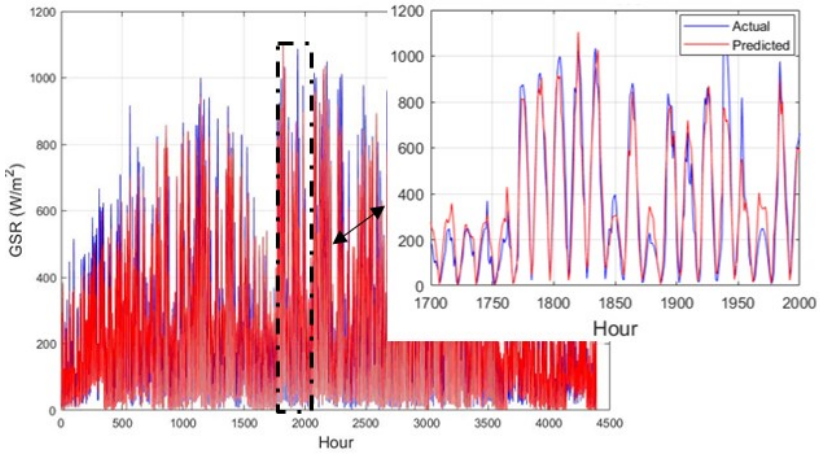

Figure 4-15 Actual and predicted GSR_H values for 2005, for ANN-H-2.1

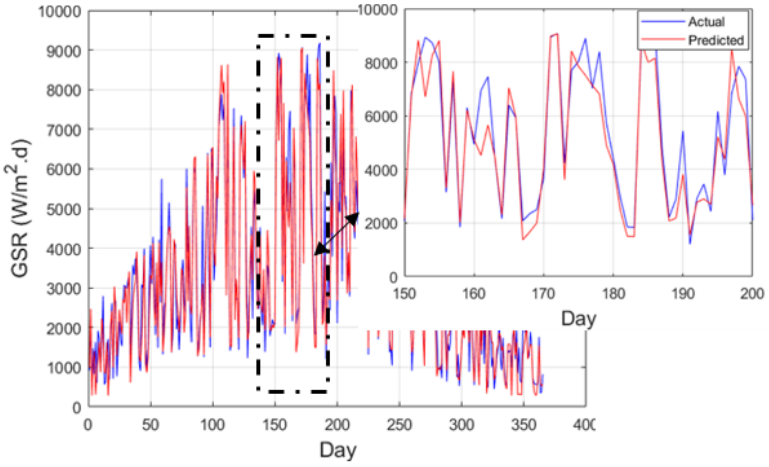

Figure 4-16 Actual and predicted GSR_D values for 2005, for ANN-D-2.1

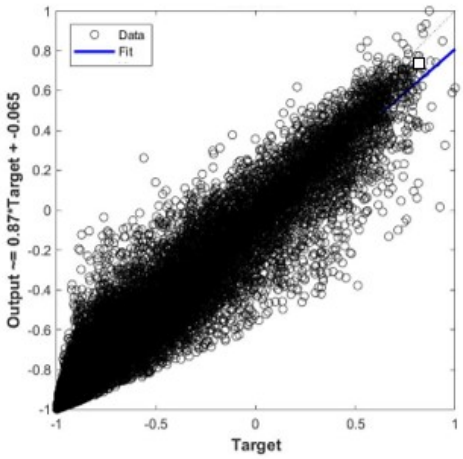

Figure 4-17 The fit between actual and predicted GSR_H values, for ANN-H-2.1

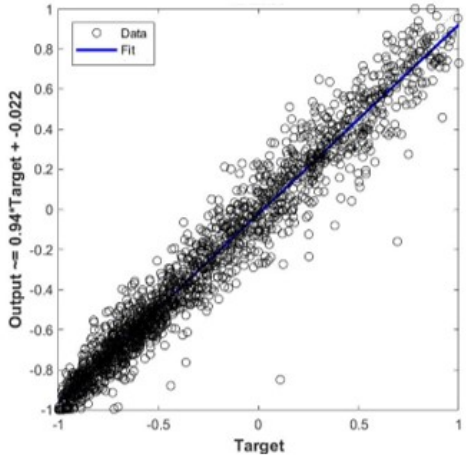

Figure 4-18 The fit between actual and predicted GSR_D values for ANN-D-2.1

It was found that using combinations of two weather variables: *hu* and *cc*, *T* and *cc*, and *hu* and *T* as inputs provided improved performance in comparison to using only one weather variable. The best results for GSR_H and GSR_D are obtained when cc and hu are used as inputs. The evaluation showed that the ANN model performed better for GSR_H and GSR_D.

Next, different combinations of more than two weather variables were used as inputs for GSR_H and GSR_D prediction, as shown in Figure 4-19. In this step, the best results for each case were selected based on *nRMSE* and *adj-* R^2, as shown in Table 4.7. The predicted GSR_H and GSR_D were compared with measured GSR_H and GSR_Dvalues for 2005, as shown in Figure 4-20 and Figure 4-21 respectively, to find the best predicted GSR_H (ANN-H-3.1) and GSR_D (ANN-H-3.1). Figure 4-22 and Figure 4-23show the fit between the predicted and actual measured GSR.

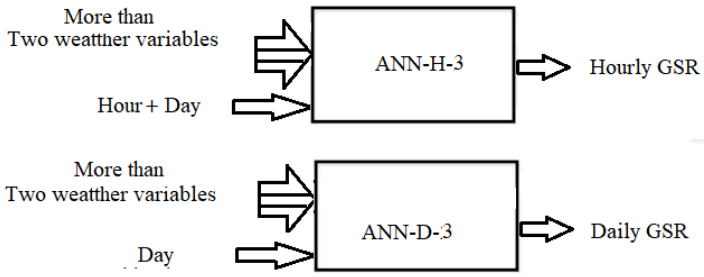

Figure 4-19 ANN-3 model structure

Table 4.7 Performance of GSR_H and GSR_D prediction, with more than two weather variables

	GSR_H				
Model	**Input**	**Neuron**	$nRMSE(\%)$	R^2	$adj - R^2$
ANN-H-3.1	D, h, T, hu, cc, w_s	170	22.915	0.9105	0.91048
ANN-H-3.2	D, h, T, hu, cc	175	25.542	0.89136	0.89134
	GSR_D				
Model	**Input**	**Neuron**	$nRMSE(\%)$	R^2	$adj - R^2$
ANN-D-3.1	D, T, hu, cc, w_s	150	8.0986	0.96533	0.96532
ANN-D-3.2	D,T, hu, cc	75	9.0514	0.96148	0.96147

As shown in Table 4.7, using the variables *T, hu, cc* and w_s (wind speed) provided the best results for GSR_H and GSR_D prediction, in comparison to previous models. Adding more weather variables as inputs slightly increases the prediction accuracy.

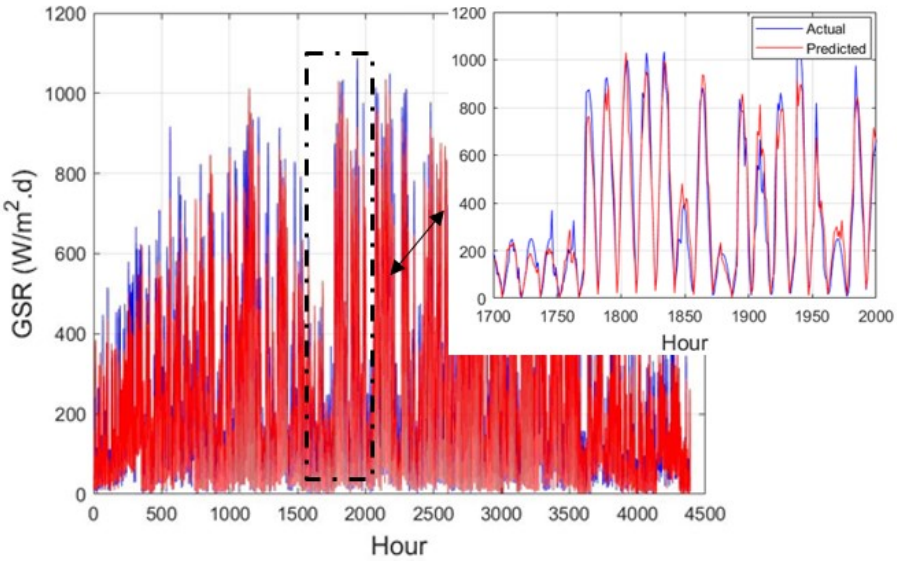

Figure 4-20 Actual and predicted GSR_H values, for ANN-H-3.1

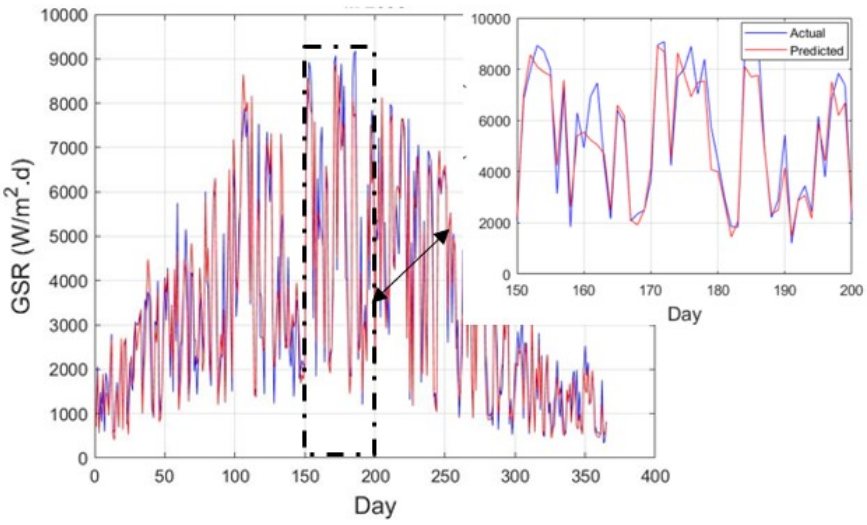

Figure 4-21 Actual and Predicted GSR_D values for ANN-D-3.1

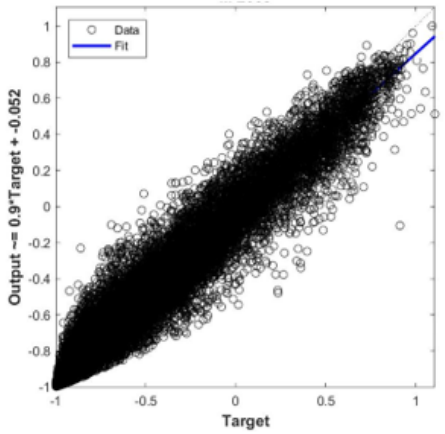

Figure 4-22 The fit between actual and predicted GSR_H values, for ANN-H-3.1

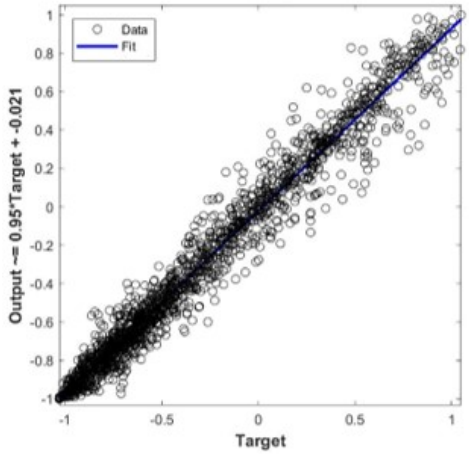

Figure 4-23 The fit between actual and predicted GSR_D values, for ANN-D-3.1

4.6.2 Construction of the Proposed Models

To develop a simple model with a better performance, three models were proposed. The maximum GSR_H and GSR_D for five years (2000:2004) were obtained and used as inputs, as shown in Figure 4-24 and Figure 4-25. Using maximum GSR_H and GSR_D gives each hour and day at a specific location a distinctive identity, by eliminating the effect of weather variables on GSR. This helps to process the effect of each individual weather variable on GSR. In addition, using maximum GSR helps to decrease the number of weather variables needed for prediction.

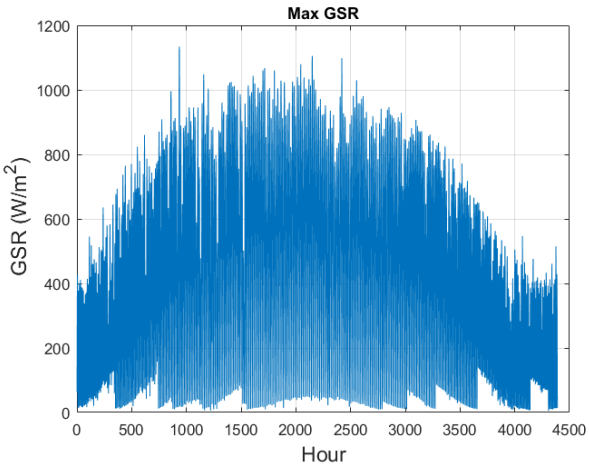

Figure 4-24 Maximum GSR_H

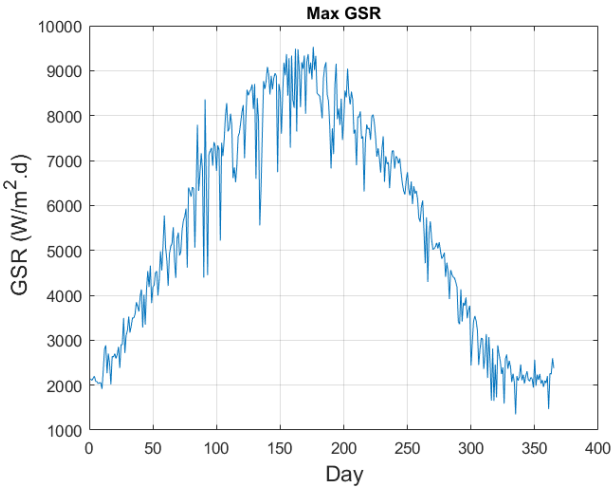

Figure 4-25 Maximum GSR_D

4.6.2.1 First Proposed Model

The first proposed model added maximum GSR_H and GSR_D as inputs to previous models, as shown in Figure 4-26, Figure 4-27 and Figure 4-28. The best results for each case, with different numbers of input weather variables, were selected based on *nRMSE* and *adj-* R^2. The proposed model, with enhanced results as compared to previous models, is shown in Table 4.8. The predicted GSR_H and GSR_D were compared with measured values for 2005, as shown in Figure 4-29 and Figure 4-30 respectively, to find the best predicted GSR_H, (ANN-H-5.1) and GSR_D (ANN-D-6.1). Figure 4-31 and Figure 4-32 show the fit between the predicted and measured values.

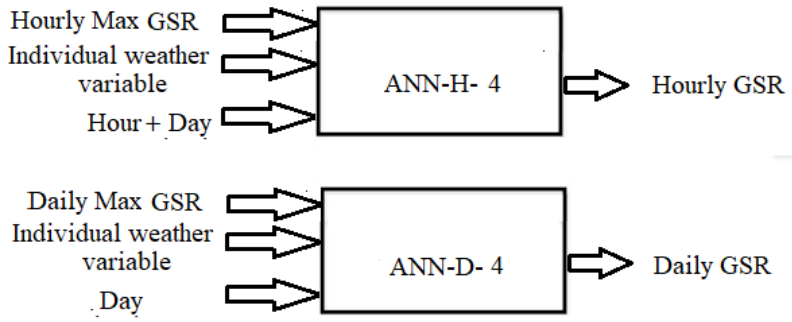

Figure 4-26 ANN-4 model structure

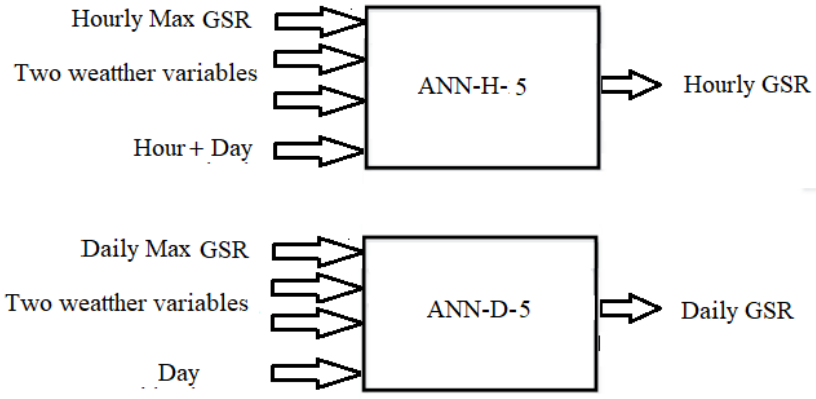

Figure 4-27 ANN-5 model structure

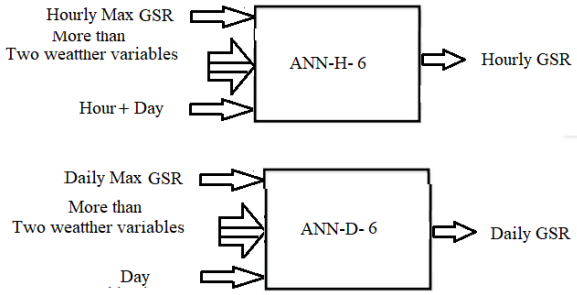

Figure 4-28 ANN-6 model structure

Table 4.8 Performance of GSR_H and GSR_D prediction, with maximum GSR_H and GSR_D as input

	GSR_H				
Model	**Input**	**Neuron**	$nRMSE(\%)$	R^2	adj-R^2
ANN-H-5.1	D, h, hu, cc, max GSR_H	125	18.068	0.94724	0.94723
ANN-H-6.1	D, h,T, hu, cc, max GSR_H	75	19.894	0.93842	0.93841
ANN-H-6.2	D, h, T, hu, cc, ws, max GSR_H	150	20.353	0.93474	0.93473
ANN-H-4.1	D, h, hu, max GSR_H	175	21.04	0.93112	0.93111
ANN-H-5.1	D, h, hu, T, max GSR_H	75	21.548	0.93071	0.93069
	GSR_D				
Model	**Input**	**Neuron**	$nRMSE(\%)$	R^2	adj-R^2
ANN-D-6.1	D, T, hu, cc, max GSR_D	150	6.9962	0.97886	0.97885
ANN-D-6.2	D,T, hu, cc, w_s, max GSR_D	50	7.9101	0.97592	0.97591

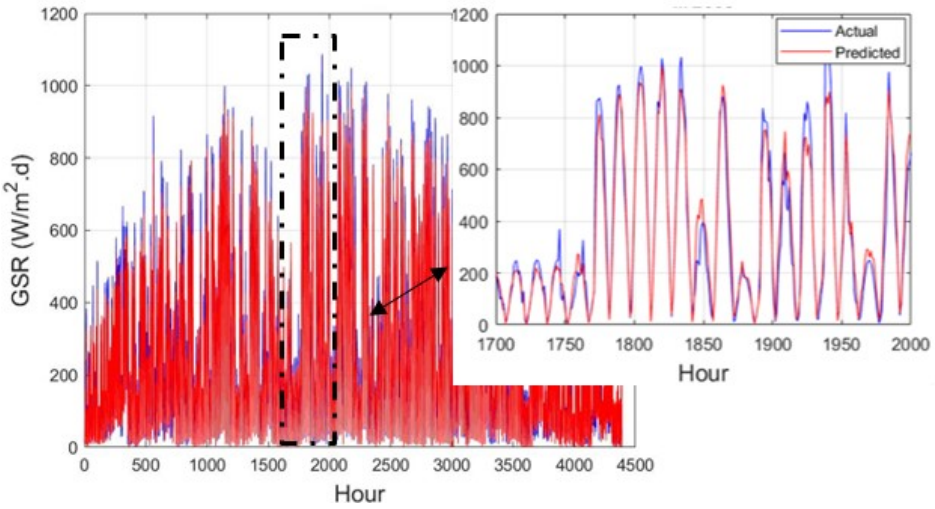

Figure 4-29 Actual and predicted GSR_H values, for ANN-H-5.1

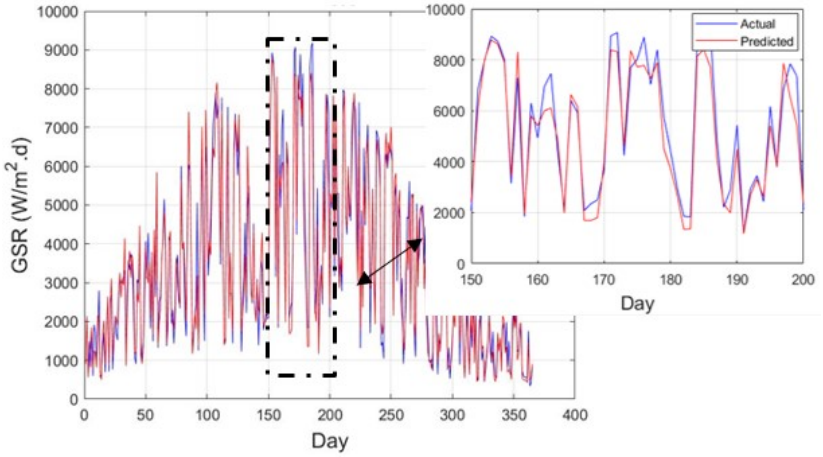

Figure 4-30 Actual and predicted GSR_D values, for ANN-D-6.1

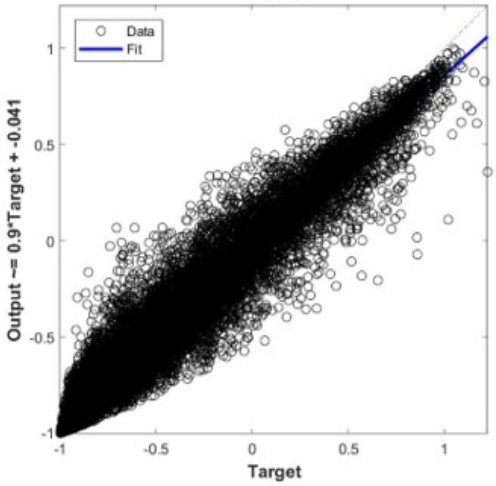

Figure 4-31 The Fit between actual and predicted GSR_H values for ANN-H-5.1

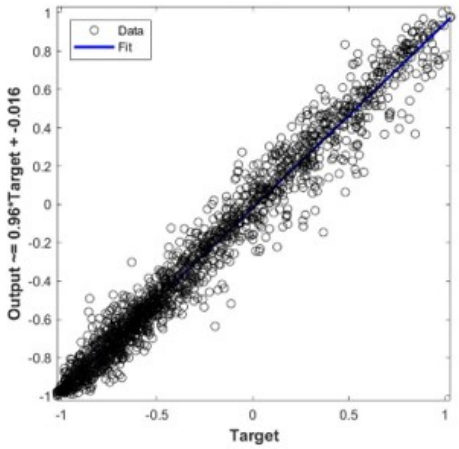

Figure 4-32 The Fit between actual and predicted GSR_D values, for ANN-D-6.1

As shown in Table 4.8, five different sub-models of the first proposed model exhibited improved results, in comparison to previous conventional models for GSR_H prediction. For GSR_D prediction, only two sub-models exhibited better results. The variables *hu* and maximum GSR_H exhibited a common influence on GSR_H prediction for each sub-model. However, *hu, T* and maximum GSR_D exhibited a common influence on GSR_D prediction. For GSR_H, sub-model ANN-H-4.1 performed well, with a simple structure, in comparison to other models. Although sub-models ANN-D-6.1 and ANN-D-6.2 performed well, more than two weather variables were required in addition to the maximum GSR_D . Moreover, this proposed model enhanced the GSR_H values more than the GSR_Dvalues.

4.6.2.2 Second Proposed Model

As shown Figure 4-33 and Figure 4-34, the second proposed model added another stage, that was fed by the output of the first proposed model (GSR_{1H} or GSR_{1D}) and two other weather variables. The best results for each case, with different combinations of the input weather variables *hu*, *cc* and *T*, were selected based on *nRMSE* and *adj-* R^2. The proposed model, with enhanced results as compared to previous conventional models and the first proposed model, is shown in Table 4.9. The predicted GSR_H and GSR_D were compared with measured values for 2005, as shown in Figure 4-35 and Figure 4-36 respectively, to find the best predicted GSR_H (ANN-H-7.1) and GSR_D (ANN-D-7.1). Figure 4-37 and Figure 4-38 show the fit between the predicted and measured values.

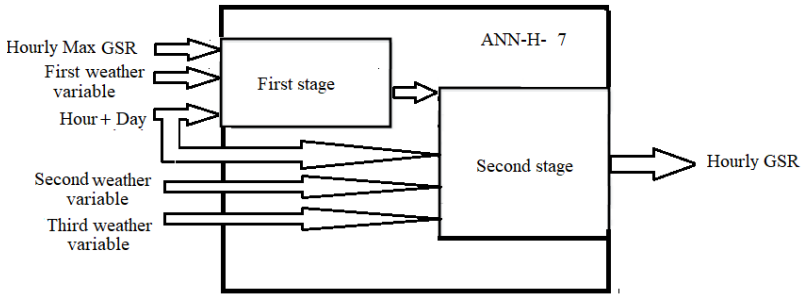

Figure 4-33 ANN-H-7 model structure

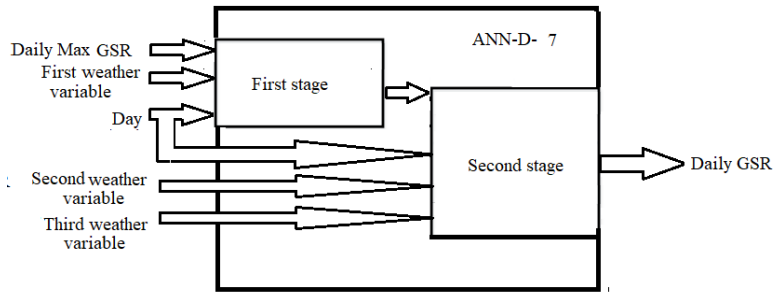

Figure 4-34 ANN-D-7 model structure

Table 4.9 Performance of GSR_H and GSR_D prediction for the second proposed model

	Hourly GSR				
Model	**Input of 1st stage**	**Input of 2nd stage**	$\boldsymbol{nRMSE}(\%)$	$\boldsymbol{R^2}$	*adj*-$\boldsymbol{R^2}$
ANN-H-7.1	D, h, cc, max GSR_H	D, h, hu, T, 1st stage output (GSR_{1H})	14.467	0.96197	0.96197
ANN-H-7.2	D, h, hu, max GSR_H	D, h, cc, T, 1st stage output (GSR_{1H})	14.908	0.96102	0.96102
ANN-H-7.3	D, h, T, max GSR_H	D, h, hu, cc, 1st stage output (GSR_{1H})	16.1	0.95508	0.95507
	Daily GSR				
Model	**Input of 1st stage**	**Input of 2nd stage**	$\boldsymbol{nRMSE}(\%)$	$\boldsymbol{R^2}$	*adj*-$\boldsymbol{R^2}$
ANN-D-7.1	D, cc, max GSR_D	D, hu, T, 1st stage output (GSR_D)	5.9958	0.98187	0.98187
ANN-D-7.2	D, hu, max GSR_D	D, cc, T,1st stage output (GSR_D)	6.1082	0.98162	0.98161

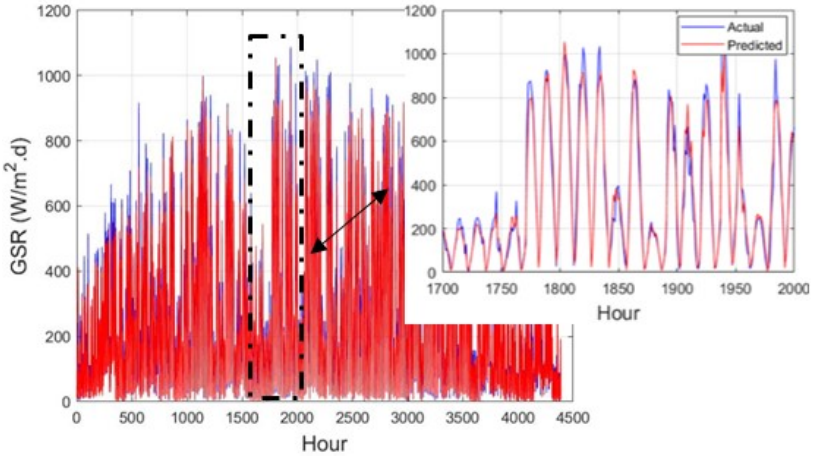

Figure 4-35 Actual and predicted GSR_H values, for ANN-H-7.1

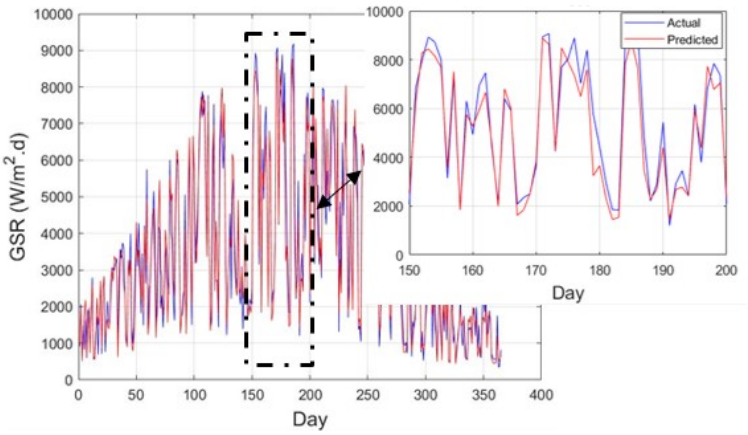

Figure 4-36 Actual and predicted GSR_D values, for ANN-D-7.1

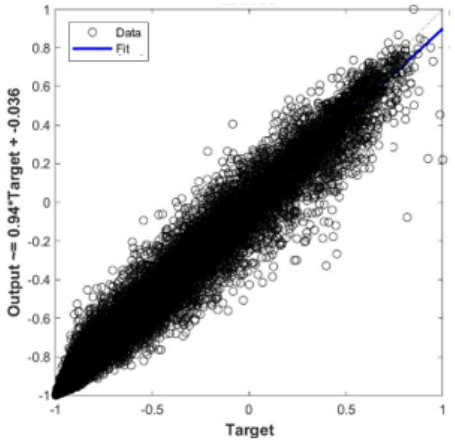

Figure 4-37 The fit between actual and predicted GSR_H values, for ANN-H-7.1

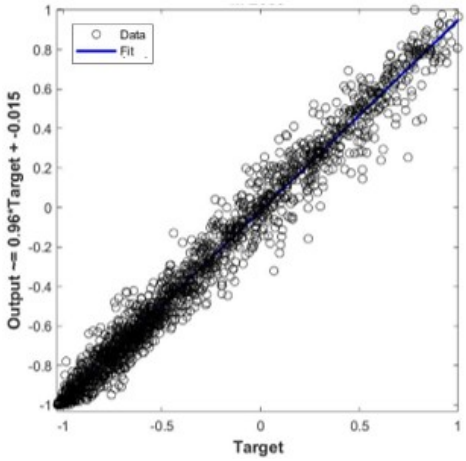

Figure 4-38 The fit between actual and predicted GSR_D values for ANN-D-7.1

As shown in Table 4.9, three different sub-models of the second proposed model exhibited improved results, in comparison to previous GSR_H prediction models. For GSR_D prediction, two sub-models exhibited better results. The ANN-H-7.1 and ANN-D-7.1 models exhibited the best performance for GSR_H and GSR_D prediction, respectively. Moreover, the second proposed model enhanced the GSR_H values more than the GSR_D values.

4.6.2.3 Third Proposed Model

The third proposed model consists of two parts. The first part predicts GSR error (GSR_e), which is the difference between the measured *GSR* and the *GSR* predicted by the second proposed model. The second part uses the output of the second proposed model (GSR_H or GSR_D). The results of both parts are then added together to generate the final predicted *GSR,* as shown in Figure 4-39 and Figure 4-40. In addition, the two parts are fed by the same input variables.

The use of ANN did not enhance the GSR_e prediction results. For this reason, WNN was used for GSR_e prediction. Various mother wavelet functions (Morlet, Mexican Hat

(Mexihat), Haar and Gaussian) were used as transfer functions for the hidden layer, for GSR_e prediction.

The third proposed model was applied only to ANN-H-7.1 and ANN-D-7.1, to enhance the performance of these models. The best results for each case, with different input weather variables and different mother wavelet functions, were selected based on *nRMSE* and *adj-*R^2. The proposed model, with enhanced results as compared to previous models, is shown in Table 4.10. The predicted GSR_H and GSR_D were compared with measured values for 2005, as shown in Figure 4-41 and Figure 4-42 respectively, to find the best predicted GSR_H (ANN-H-8.1) and GSR_D (ANN-D-8.1). Figure 4-43 and Figure 4-44 show the fit between the predicted and measured values. The hourly and daily GSR_e predicted by the second proposed model for the best cases of GSR_H and GSR_D, ANN-H-8.1 and ANN-D-8.1, are shown in Figure 4-45 and Figure 4-46, respectively. The errors produced by the final predicted GSR_H and GSR_D are shown in Figure 4-47 and Figure 4-48, respectively.

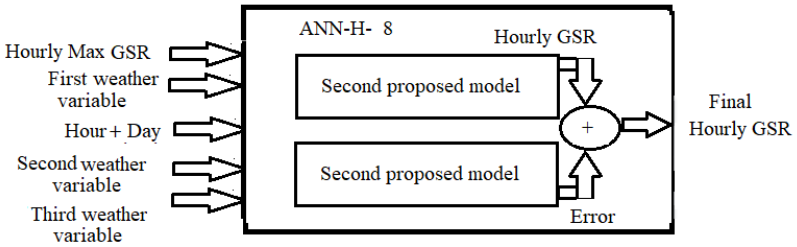

Figure 4-39 ANN-H-8 model structure

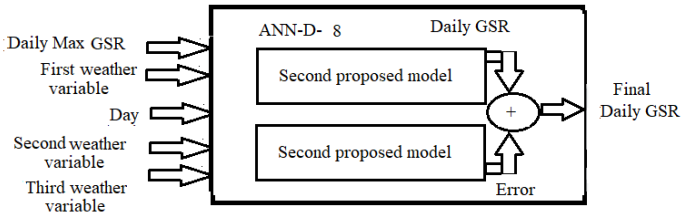

Figure 4-40 ANN-D-8 model structure

Table 4.10 Performance of GSR_H and GSR_D prediction, for third proposed model

	Final GSR_H					
Model	**Input of 1st stage**	**Input of 2nd stage**	**Function of Hidden layer**	$nRMSE(\%)$	R^2	*adj*-R^2
ANN-H-8.1	D, h, cc, max GSR_H	D, h, hu, T, 1st stage Output(GSR_{1H})	Morlet	12.505	0.96939	0.96939
			Mexihat	14.204	0. 96231	0. 96231
ANN-H-8.2	D, h, hu, max GSR_H	D, h, cc, T, 1st stage output(GSR_{1H})	Morlet	13.566	0.966	0.966
			Mexihat	14.775	0.96125	0.96125
ANN-H-8.3	D, h, T, max GSR_H	D, h, hu, cc, 1st stage Output(GSR_{1H})	Morlet	15.687	0.95718	0.95718
			Mexihat	15.795	0.95668	0.95668
	Final GSR_D					
Model	**Input of 1st stage**	**Input of 2nd stage**	**Function of Hidden layer**	$nRMSE(\%)$	R^2	adj-R^2
ANN-D-8.1	D, cc, max GSR_D	D, hu, T, 1st stage output(GSR_{1D})	Morlet	5.103	0.9829	0.9829
ANN-D-8.2	D, hu, max GSR_D	D, cc, T 1st stage output(GSR_{1D})	Mexihat	5.719	0.982	0.982

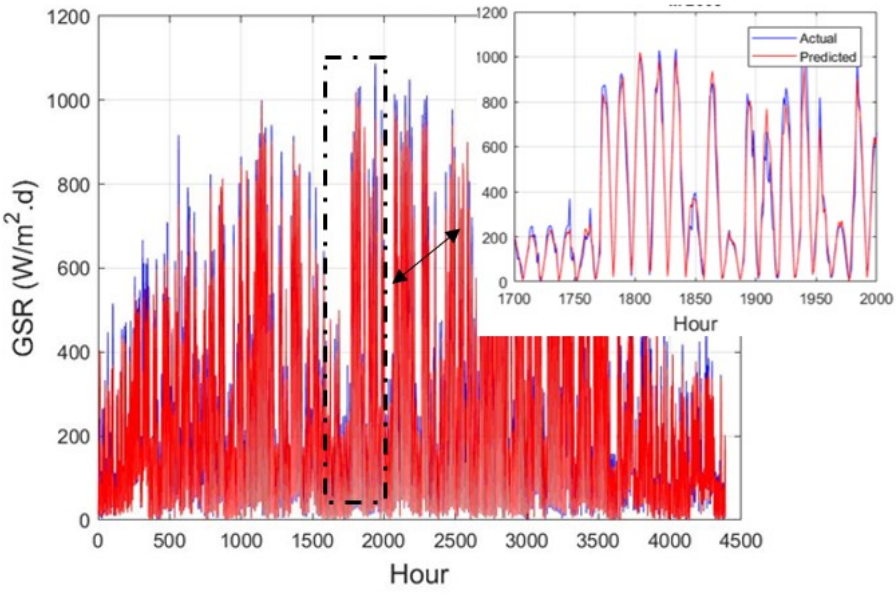

Figure 4-41 Actual and predicted GSR_H values, for ANN-H-8.1

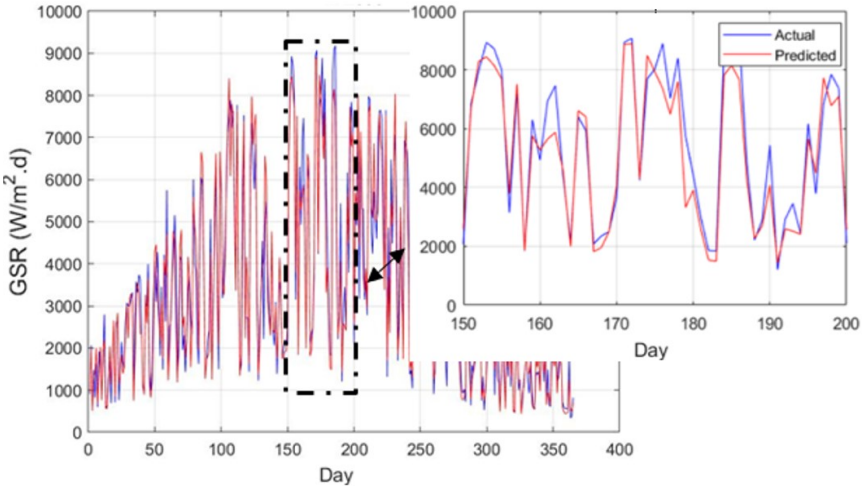

Figure 4-42 Actual and predicted GSR_D values, for ANN-D-8.1

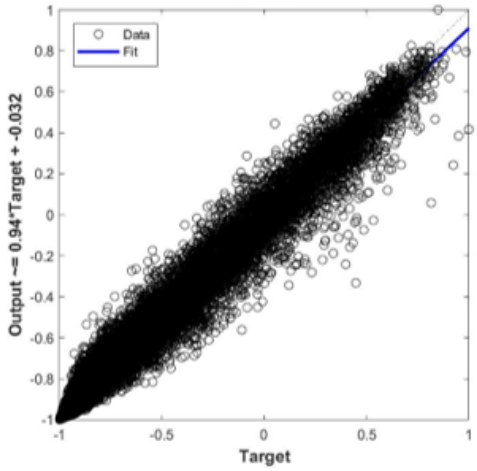

Figure 4-43 The fit between actual and predicted GSR_H values, for ANN-H-8.1

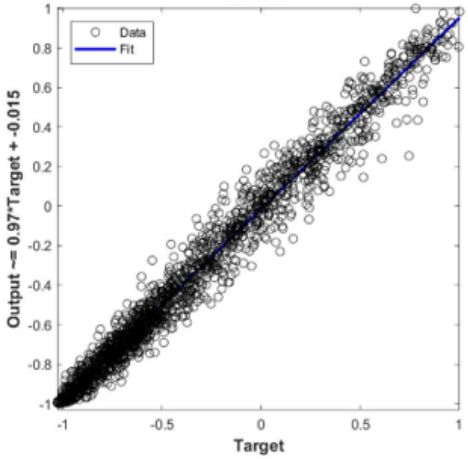

Figure 4-44 The fit between actual and predicted GSR_D values, for ANN-D-8.1

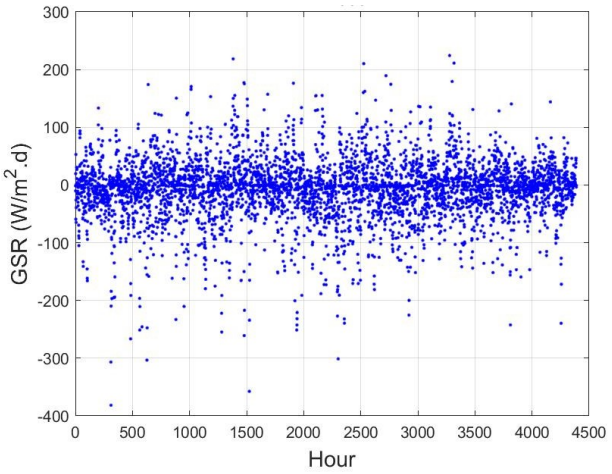

Figure 4-45 Predicted hourly GSR_e by the second proposed model, ANN-H-8.1

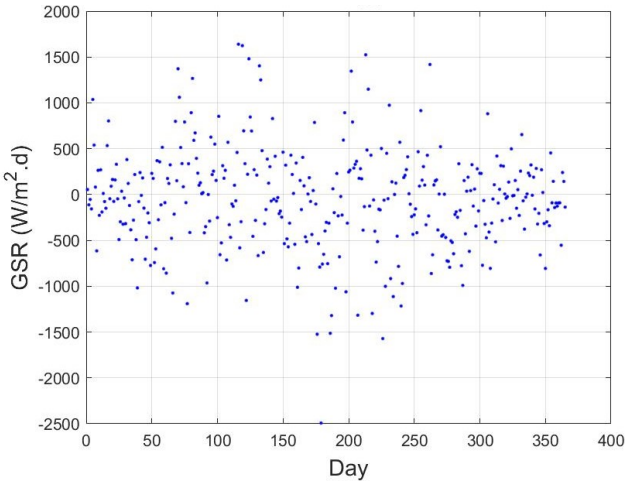

Figure 4-46 Predicted daily GSR_e by the second proposed model, ANN-H-8.1

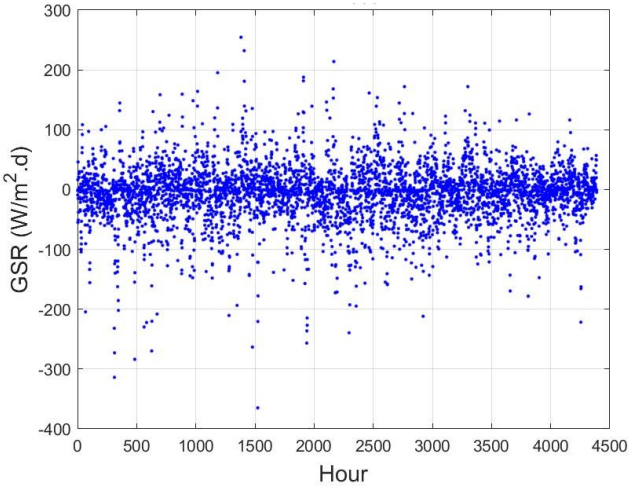

Figure 4-47 Final hourly error, for ANN-H-8.1

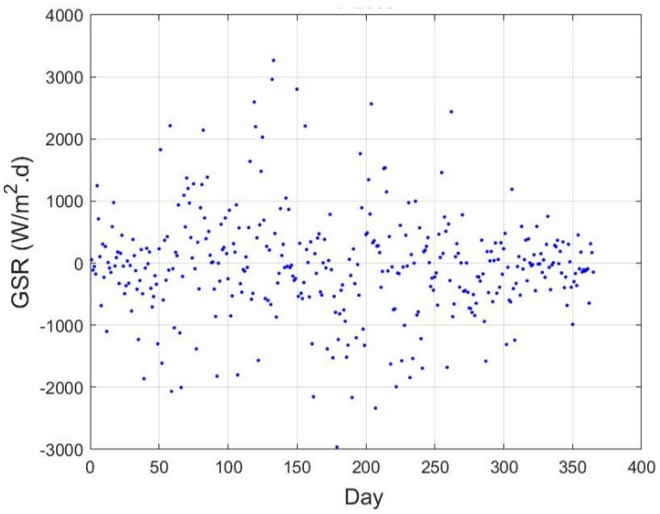

Figure 4-48 Final daily error, for ANN-D-8.1

As shown in Table 4.10, the third proposed model exhibited better results than previous conventional models and the other proposed models, for GSR_H and GSR_D prediction. The use of a Morlet wavelet function as a hidden layer transfer function for *GSR* error prediction achieved the desired goal. The ANN-H-7.1 and ANN-D-7.1 models exhibited the best performance for GSR_H and GSR_D prediction, respectively. This proposed model enhanced the GSR_H values more than the GSR_D values.

The absolute error values for GSR_H prediction is determined for monthly and seasonally trend evaluation as shown in Figure 4-49. It can be seen that GSR_H prediction error is weather sensitive. The error increases in winter and spring because of the highest variability of the cloudiness in both seasons. This applies for GSR_D prediction case.

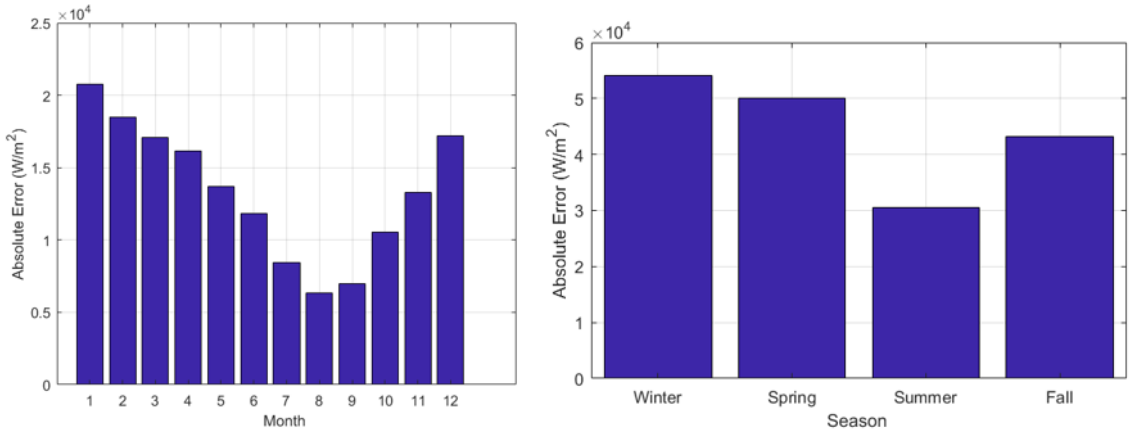

a) Monthly absolute error b) Seasonally absolute error

Figure 4-49 Monthly and seasonally absolute error for GSR_H prediction

4.6.3 Comparison with Other Studies

Various studies have been done with different geographic locations and weather conditions, GSR_H and GSR_Dprediction. Table 4.11 and Table 4.12 present an overview of other studies and proposed models that carry out GSR_H and GSR_D prediction. This comparison includes input weather variables and the performance of different models.

Table 4.11 Comparison of the developed model and other GSR_H ANN models

	GSR_H		
Author	**Inputs**	**Location**	**Performance Evaluation**
Moustris et al. (2008) [100]	latitude, longitude, altitude, sunshine hours, cloud cover, hourly data of air temperature, and relative humidity	Greece	R=0.99
Alam et al. (2009) [101]	latitude, longitude, altitude, time, months of the year, air temperature, relative humidity, rainfall, wind speed, and net long wavelength	India	R^2=0.85 nRMSE=8.8%
Pavan et al. (2010) [102]	Solar irradiance, the number of days in a month and mean air temperature per day	Italy	R^2=0.95-0.98 (Sunny day) R^2=0.92-0.95 (Cloudy Day)
Mellit et al. (2010) [102]	Hourly solar irradiance, air temperature, and hours	Italy	R=98.95 nRMSE=13.14%
Hasni et al. (2012) [107]	month, day, hour, temperature and relative humidity	Algeria	R^2=0.85 nRMSE=17.2%
Loutfi, et al. (2017) [113]	Temperature, pressure, relative humidity, wind speed	Moroco	R^2=0.932 nRMSE=15%
1st proposed model	Day, hour, relative humidity, Temperature, cloud cover, Max GSR_H	Canada	R^2=0.94724 nRMSE=18.068%
2nd proposed model	Day, hour, relative humidity, Temperature, cloud cover, Max GSR_H	Canada	R^2=0.96197 nRMSE=14.467%
3rd proposed model	Day, hour, relative humidity, Temperature, cloud cover, Max GSR_H	Canada	R^2=0.96939 nRMSE=12.505%

Table 4.12 Comparison of the developed model and other GSR_D ANN models

	GSR_D		
Author	**Inputs**	**Location**	**Performance Evaluation**
Deng et al. (2010) [103]	latitude, longitude, altitude, sunshine duration, air temperature, rainfall, relative humidity, atmospheric pressure, and day of year	China	R^2=0.93
Angela et al. (2011) [105]	Sunshine duration	India	R^2=0.963 nRMSE=52%
Alharbi, et al. (2013) [108]	Temperature, relative humidity, and daily date	Saudi Arabia	R^2=0.986 nRMSE=7.5%
Bader, et al. (2014) [109]	Day, relative humidity, and air temperature	Saudi Arabia	R^2=.98 nRMSE=4.75%
Masoud, et al. (2017) [112]	Particulate Matter, Relative Humidity, Wind Speed and Daily Temperature	Iran	R^2=.99 nRMSE=5%
Yıldırım, er al.(2017) [114]	Sunshine duration, Temperatur and Relative Humidity	Turkey	R^2=.9611 nRMSE=14%
1st proposed model	Day, hour, relative humidity, Temperature, cloud cover, max GSR_D	Canada	R^2=0.97886 nRMSE=6.9962%
2nd proposed model	Day, hour, relative humidity, Temperature, cloud cover, max GSR_D	Canada	R^2=.98187 nRMSE=5.9958%
3rd proposed model	Day, hour, relative humidity, Temperature, cloud cover, max GSR_D	Canada	R^2=0.9829 nRMSE=5.103%

The three proposed models use the same input weather variables in addition to maximum *GSR*, with different structural configurations. These weather variables are widely available and easily measured. The weather conditions in Halifax are relatively volatile in comparison to those of other areas. In addition, earlier work took place close to the equator compared to this work. This makes the prediction process more difficult and the solar

radiation more sensitive to other weather variables for this study. For GSR_H prediction, the three proposed models perform better than other models. *nRMSE* of the proposed models within the band of errors of earlier works, 9% to 19%. Although the model proposed by Alam (2009) has a lower *nRMSE* value, more input weather variables are required for the prediction process. For GSR_D prediction, the three proposed models perform better than other models. *nRMSE* of the proposed models within the band of errors of earlier works, 5% to 15%. However, the models proposed by Bader (2014) and Masoud (2017) have slightly lower *nRMSE* values.

The second model proposed for *GSR* prediction is used as part of a load management application. More details will be provided in the following section.

4.6.4 Conclusions

Three new models are proposed for predicting GSR_H and GSR_D by using ANN and WNN with the most effective combination of weather variables. Performance is enhanced by using maximum *GSR* as an input for prediction models. For this study, a weather dataset for a specific location in Canada was used. These data, collected between 2000 and 2005, include *cc, hu, T,* w_s, and *GSR*.

In the first step, different combinations of weather variables and model structures were tested, and *MATLAB* ™ simulations were used to find the most effective weather variables. It was found that cc*, hu,* and *T* are the best combination of variables for predicting GSR_H and GSR_D. These variables were used as inputs for the proposed models.

The first proposed model was selected from combination models that use max *GSR* in addition to other weather variables. *hu, cc,* and max *GSR* gave improved accuracy for GSR_H

prediction (ANN-H-5.1). However, *cc, hu, T,* and max *GSR* provided better accuracy for GSR_D predictions (ANN-D-6.1).

For the second proposed model, *cc* and max *GSR* were used as inputs for the first stage, and *hu* and *T* were used for the second stage of the model. This combination gave the best results in terms of accuracy for GSR_H and GSR_D prediction (ANN-H-7.1 and ANN-D-7.1).

For the third proposed model, *cc* and max *GSR* were used as inputs for the first stage, and *hu* and *T* were used in the second stage for GSR_{1H} and GSR_{1D} and GSR_e prediction (ANN-H-8.1 and ANN-D-8.1). The Morlet wavelet function was used as a transfer function for the hidden layer of the GSR_e prediction. The three proposed models favor GSR_H prediction in comparison to GSR_D prediction. These models gave good results compared to others, although weather conditions in Halifax are relatively volatile in comparison to those of other areas.

CHAPTER 5 HARMONICS

Solar energy sources require the use of power converters, however these introduce harmonics into the output waveforms. This chapter describes the concept of harmonics, and discusses their causes and effects.

5.1 INTRODUCTION

Harmonic distortion can be divided into two classes, voltage distortion and current distortion, as illustrated in Figure 5-1 . Because the voltage is common to all loads in a system, any voltage distortion that occurs will result in a corresponding current distortion, assuming that the source impedance is low. Conversely, current distortion results in voltage distortion only insofar as the source impedance provides a common coupling impedance [115].

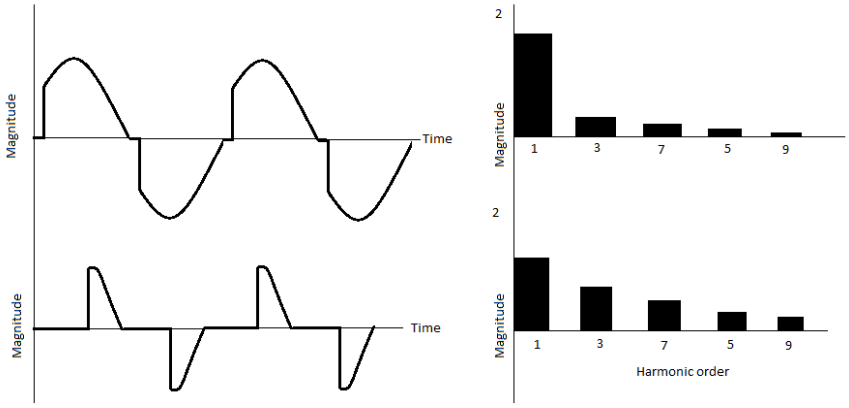

Figure 5-1 Harmonic distortion of different waveform

Two concepts must be addressed to gain a full understanding of harmonic phenomena. The first concept concerns the nature of loads which cause the production of harmonic voltages

and currents, namely non-linear loads. The second concept involves the way that harmonic currents flow, and how subsequent harmonic voltages arise.

It should be pointed out that symmetrical waves contain only odd harmonics, whereas asymmetrical waves contain both even and odd harmonics. A wave which exhibits symmetry is one in which the positive and negative parts are identical, but opposite in magnitude. A wave which is asymmetrical contains a DC offset; in other words, the positive section of the wave differs from the negative section [116].

5.2 CAUSES OF HARMONICS

Non-linear loads exhibit a waveform that does not look like the applied voltage waveform. This can occur for various reasons. One example involves the use of switches which conduct the load current only during a portion of the full period of the applied power waveform. In this case, it is possible to conceive of a non-linear load where Ohm's law does not accurately describe the relationship between the voltage and the current.

Rectifying devices in power systems account for the most common non-linear loads. Such loads are present in power converters, power supplies, UPS systems, arc devices such as electric furnaces for melting metals, electroplating systems, and fluorescent lamps [116].

When harmonics are added together with the characteristic components, waveforms are produced which have components that are not whole integer multiples of the fundamental frequency of the particular system. These are referred to as inter-harmonics. Inter-harmonics commonly occur with the use of AC to AC converters. These devices operate with a set amplitude and frequency at the input, however, at the output these factors can be variable in nature [116].

Non-linear loads generally do not cause reactive power to flow at the fundamental system frequency. However, it is possible that they may draw high root mean square (RMS) currents and thus add to distribution losses for a given load. The non-linear nature of the load then draws non-pure sinusoidal waveform currents, which cause harmonics of the fundamental current to be present. Because the connection of non-linear elements to the power system causes harmonic distortion, any device with non-linear characteristics can act as the cause of such distortion. For example, power system harmonics (some more problematic than others) can occur in the following [115]:

- Transformer saturation
- Transformer neutral connections
- Arc Furnaces
- Fluorescent lighting
- Battery charging devices
- Imperfect AC sources
- Variable frequency motor drives
- Inverters

Non-linear loads such as these reduce the power factor not because of a phase shift of the fundamental current with respect to the voltage, but rather due to higher RMS currents which arise because of the pulsed nature of the input current. This means that power is taken from the source only for a short time near the peak of the voltage wave. The higher line current causes a reduction in the power factor, because the total power factor is defined as the real power in Watts divided by the product of the RMS voltage and current [115].

Applications that utilize electricity with loads that require some form of power conditioning, such as rectification and inversion, are steadily increasing. Most industrial non-linear loads are associated with solid state switches, which are used in power converting devices that convert electrical power from one form to another. This includes AC to DC converter units for motor speed control, and units that convert from AC to DC and back again to AC at variable frequencies, for processes involving the speed control of induction motors. Many bulk energy conversion processes occur in the oil, mining, steel milling, pulp and paper, and automobile industries, as well as in the area of manufacturing and factories employing electrolytic coating processes [116].

Non-sinusoidal scenarios can also occur when harmonics are contained within network voltages and currents. Although some harmonics are caused by non-linear system components, most harmonics are the result of power electronic loads such as adjustable-speed drives and diode bridge rectifiers. The harmonics above the fundamental frequency which are considered to be significant are usually the 3^{rd}, 5^{th}, and 7^{th} multiples in 50 Hz or 60 Hz systems. Thus, the frequencies of interest lie in the low audible range [117].

With regard to PV systems in particular, when a large number of PV systems is installed in the same area, harmonic currents generated by these systems may be detrimental to the quality of the electrical grid supply, and may negatively alter the performance of other equipment connected to the grid. In addition, the inverters themselves are quite sensitive to harmonic voltages, and may possibly operate incorrectly as a result of harmonic voltage distortion. For this reason, engineers must be able to predict these undesirable effects and mitigate them or prevent them entirely before they occur [118].

5.3 EFFECTS

The effects produced by harmonic currents from non-linear loads are not completely understood. The vast majority of power systems operate with a low impedance, which enables them to absorb significant amounts of harmonic current without converting the harmonics into undesirable voltage distortion levels [116].

The effects of harmonic distortion range from equipment losses, where the service life of equipment, such as transformers and cables, is shortened, to interference in audio and data communications systems. As well, harmonics can also cause the tripping of protective devices such as surge protectors, resulting in unnecessary equipment downtime. The monetary cost of cleaning or filtering out such harmonic noise often reduces the benefit of improving the equipment to enable it to function better in a disturbed environment. A general rule of thumb in electronics is that the more components there are, or the more sophisticated and sensitive the electronic equipment is, the more it will cost to maintain, because it can be expected to be more sensitive to harmonic distortion disturbances [116].

Sensitive industrial processes such as automated assembly lines are susceptible to power-related damage from harmonic distortion. Conversely, the more rigid the AC source is, the lower the harmonic voltage distortion will be across the terminals.

The harmonic voltages in a system sum together, and when added to the nominal voltage produce a voltage distortion which misrepresents the actual system voltage. The magnitude of the voltage distortion is dependent on the source impedance and the harmonic voltages being produced. In a situation where the source impedance is low, the voltage distortion will also be low. If a significant portion of the load becomes non-linear, with increased

harmonic currents, and a resonant condition with greater impedance becomes prevalent in the circuit, the voltage can increase dramatically. Harmonic currents are responsible for a number of problems, such as: [119]

- Overheating of equipment
- Malfunction
- Failure
- Interference
- Tripping of breakers/fuses
- Process issues
- Conductor heating
- Risk of fire

In turn, all of these risks result in increased maintenance costs for the system. Of course, it can be inferred that the effects on a system caused by exposure to harmonics are not always immediately visible, but can have serious consequences in the medium to long term. In general, this is because such distortions subject systems to voltages and currents outside the range of values for which they were designed. Utility companies in particular face a number of challenges with regard to harmonics insofar as they have to deal with increased RMS currents, heating and line losses. Power transformers are also prone to overheating. Distribution equipment may become de-rated, and overloading can occur in phase and neutral conductors. Resonances also can amplify harmonic currents. In addition, a wide range of component failures may also occur [119].

The effects of poor power quality on electrical equipment can differ depending on the component affected. Different electronic devices have set tolerances, and can withstand specific ranges of inputs up to a certain threshold before they are subject to failure. Device design plays a pivotal role in the length of life of a given piece of equipment and the efficiency of its operation in the event of different degrees of disruption. A number of critical factors are vital in determining the tolerance of a device. Some of these are: [120]

- The age of the device
- The duration and magnitude of a particular disturbance
- The frequency of occurrence of the disturbance
- The sensitivity of the device (determined by the specifications and design)
- The location of the device within a given installation
- The pathway existing between the device and the event
- Network impedance

5.4 METRIC USED IN THE MEASUREMENT OF HARMONIC LEVELS

One metric frequently used in the measurement of harmonic levels is total harmonic distortion (THD), which is also known as the distortion factor. This measurement is comprised of the ratio of the RMS value of the harmonics present above the fundamental frequency to the RMS value of the fundamental multiplied by 100%. This ratio is given by [116], [117]

$$THD_V = \frac{\sqrt{\sum_{h=2}^{\infty} V_{h\,rms}^2}}{V_{1\,rms}} * 100 \tag{5.1}$$

$$THD_I = \frac{\sqrt{\sum_{h=2}^{\infty} I_{h\,rms}^2}}{I_{1\,rms}} * 100 \tag{5.2}$$

If there are no harmonics, then the THD will be zero. The true power factor is given by [53], [121]:

$$PF_{true} = \frac{P_{avg}}{V_{1\,rms} I_{1\,rms} \sqrt{1 + (\frac{THD_V}{100})^2} \sqrt{1 + (\frac{THD_I}{100})^2}} \tag{5.3}$$

where the RMS values for voltage and current are given by [53], [121]:

$$V_{rms} = V_{1\,rms} \sqrt{1 + (\frac{THD_V}{100})^2} \tag{5.4}$$

$$I_{rms} = I_{1\,rms} \sqrt{1 + (\frac{THD_I}{100})^2} \tag{5.5}$$

The average power is calculated via the expression [116], [117]:

$$\begin{aligned} P_{avg} &= \sum_{h=1}^{\infty} V_{h\,rms} I_{h\,rms} \cos(\delta_h - \theta_h) \\ &= P_{1avg} + P_{2avg} + P_{3avg} + \cdots \end{aligned} \tag{5.6}$$

Here it can be seen that every harmonic present makes a contribution, either positive or negative, to the average power of the system.

Finally, the power factor expression can be further simplified by expressing the equation as the product of two components. This is given by [116], [117]:

$$PF_{true} = \frac{P_{avg}}{V_{1\,rms} I_{1\,rms}} * \frac{1}{\sqrt{1 + (\frac{THD_V}{100})^2} \sqrt{1 + (\frac{THD_I}{100})^2}} \tag{5.7}$$

If two assumptions are incorporated into the above expression, one being that in most cases the contributions made by harmonics above the fundamental frequency to the average

power are modest such that $P_{avg} = P_{1avg}$, and the second being that the total harmonic distortion of the voltage is typically 10% or less such that $V_{rms} = V_{1\,rms}$, then the approximation of the true power factor can be simmplified to [116], [117]:

$$PF_{true} \approx \frac{P_{1avg}}{V_{1\,rms} I_{1\,rms}} * \frac{1}{\sqrt{1 + \left(\frac{THD_I}{100}\right)^2}} = PF_{dis} PF_{dist} \tag{5.8}$$

It is important to note that generally it is not possible to compensate for a poor distortion power factor (PF_{dist}) simply by adding shunt capacitors. Only a displacement power factor (PF_{dis}) can be improved by the addition of capacitors. This is especially significant in load areas with mainly single-phase power electronic loads, because these tend to have high displacement power factors but low distortion power factors. In fact, adding shunt capacitors in such instances is likely to have a detrimental effect on the power factor, by causing resonances and increased harmonic levels. A more effective solution would be to add passive or active filters with the aim of removing the harmonics produced by non-linear loads, or perhaps to use low distortion power electronic loads [116].

5.5 LITERATURE REVIEW

Different types of converters are available. They are chosen based on the method of isolation, the number of conversion stages, and the DC link. Three types of commonly used converter are an inverter with a DC link, an inverter with a pseudo-DC link, and an inverter without a DC link [122]. The prevalent topologies have one or two stages. The number of stages is significant in determining the complexity of the PV system and its cost. A single-stage structure has the most advantageous topology; however, problems can appear during implementation and some benefits may be lost. Although multiple stage inverters can

accept a wide range of voltage inputs, they are typically more expensive and more complex. New trends in inverter development favor inverters without a DC link, to reduce the total number of conversion stages and the overall cost per unit volume [122].

Most advanced work is focused on increasing the overall efficiency, minimizing the leakage current, reducing the harmonic distortion, and regulating the output voltage. Utilizing a suitable pulse width modulation (PWM) technique and adding more switches to the fundamental converter help to regulate the voltage across the flying capacitor, as shown in Figure 5-2.

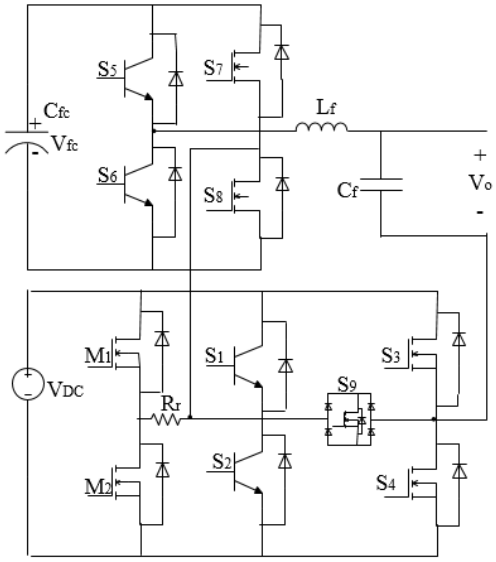

Figure 5-2 Inverter with a flying capacitor [123]

Another topology consists of a capacitor selection circuit and a full-bridge converter, as shown in Figure 5-3 [124]. This configuration helps to reduce the number of switches. Switching losses are decreased by reducing the number of switches operating at a high

frequency to a single switch. In this configuration, techniques of the DC-AC converter are similar to fundamental converter techniques.

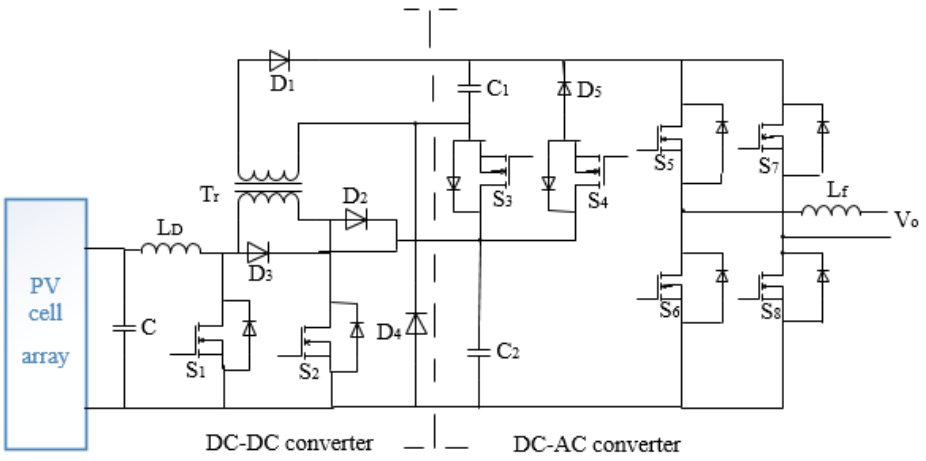

Figure 5-3 Configuration of seven-level inverter

Figure 5-4 shows the topology of an active buck-boost inverter [125]. It is a quasi single-stage inverter that aims to eliminate the drawbacks of using single- or multistage inverters. It consists of a full bridge and AC/AC units that share the inductor and capacitor.

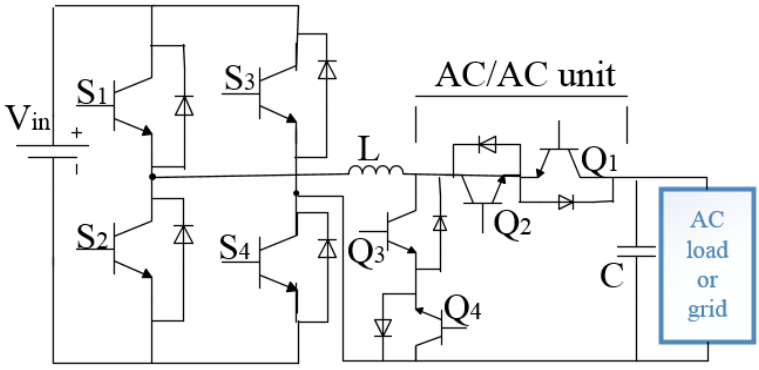

Figure 5-4 Active buck–boost full-bridge inverter [126]

Another topology involves a switched-capacitor circuit (SC) followed by an H-bridge, as shown in Figure 5-5. The number of SCs and H-bridges connected in series or in parallel determines the number of voltage steps. The SC circuits consist of switches S_1, S_2, S'_1, and

S’$_2$, and capacitors C_1 and C_2. The H-bridge consists of switches S_{1a}, S_{11}, S_{12}, S_{13}, S_{21}, S_{22}, S_{23}, and S_{24} which provide negative voltage steps. All the switches are controlled by pulse width modulation (PWM). Diodes D_1 and D block the current going back to the DC input source. C_1 and C_2 are equal to V_{DC1} and V_{DC2} respectively, when they are fully charged [127].

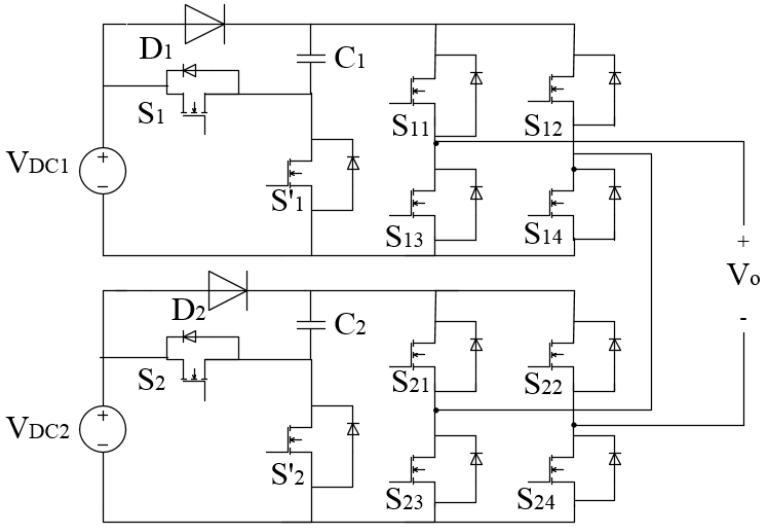

Figure 5-5 Topology with switched-capacitor circuit (SC) followed by H-bridge

Most converter topologies are derived from the fundamental topology shown in Figure 5-6. For this reason, this study will focus on this topology, with different techniques.

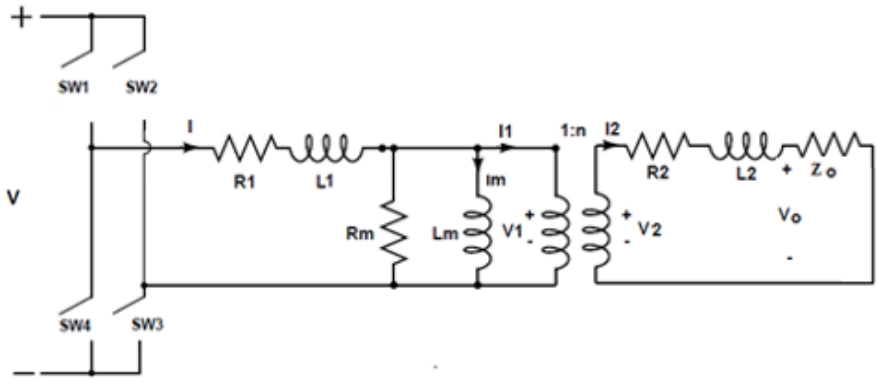

Figure 5-6 Classic model of PV DC-AC conversion system

5.6 Effect of Weather Conditions on Harmonic Performance of PV Inverters

Most converter topologies are derived from the fundamental topology illustrated in Figure 5-6. The present work therefore focuses on this topology, with different techniques. Three years' worth of data involving various environmental conditions are used for three different case studies [3], [7]. The data is fed to the PV model, and the voltage and current at the maximum power point are determined. Most earlier work has focused on varying either the radiation or the temperature and determining the effect on the maximum power point [128]-[130]. This work utilizes real data that has different radiation and temperature values in a given time span, without using a DC link in the conversion stage. The dataset was applied to a PV model, and maximum power point tracking (MPPT) was implemented by using the model and algorithm found in [7]. Then, three different inverting techniques are applied to generate AC signal. Finally, harmonics are extracted from the AC signal as shown in Figure 5-7.

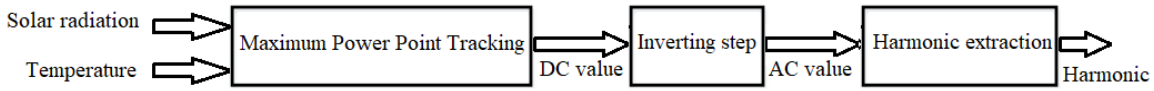

Figure 5-7 Steps of Harmonic extraction

5.6.1 Modeling of PV DC-AC Conversion System using resistive output load

This work studies the effects of variations of environmental conditions on the output voltage harmonics of a PV system. This study uses a dataset of the average solar radiation (hourly and daily) and the hourly average temperature over a three-year time span (2001 to 2003), as shown in Figure 5-8. This dataset was provided by Environment Canada, and

measurements were obtained by using a pyranometer [81]. In cases when observations were unavailable, a MAC3 model, WON statistical model, or linear interpolations were used to estimate the climate information [131]. It has been assumed that an hourly dataset was sufficient to represent environmental fluctuations. In reality, a study should be conducted for each environment, to determine the sampling period which accurately represents weather patterns. Moreover, due to seasonal variations, it is important to study the weather patterns over an entire year. In addition, it is assumed that the hourly available data is obtained based on measurements that meet the Nyquist sampling criteria. The highest frequency is about 49th harmonic order.

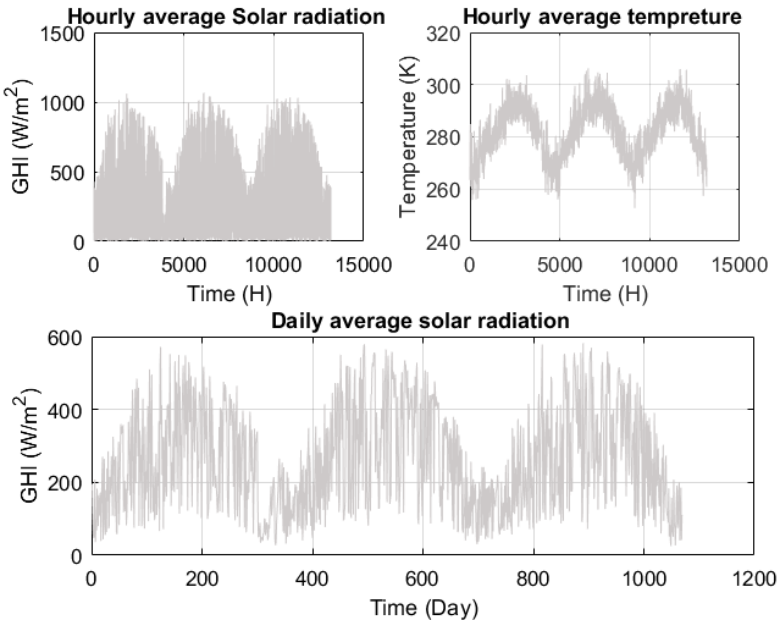

Figure 5-8 Time variation of average solar radiation and temperature

A Solarex MSX60 60w module was used for this simulation. The PV module parameters are given, including the number of series and parallel cells in the PV array [71]. The PV system consists of two modules connected in parallel to generate an output power of approximately 75 W.

Due to the nonlinearity of the current-voltage equation for the PV cell, an iterative method such as the Newton-Raphson method is required to solve for the current [131]:

$$X_{n+1} = X_n - \frac{f(X_n)}{f'(X_n)} \tag{5.9}$$

where X_{n+1} is a new value, X_n is the present value, and $f'(X_n)$ is the derivative of the function evaluated at the present value. The current-voltage (I-V) relationship for the PV array becomes:

$$f(I) = N_p I_L - N_p I_o \exp\left[\frac{q\left(\frac{V}{N_S} + \frac{IR_{s)}}{N_p}\right)}{nkT} - 1\right] - \frac{\frac{VN_p}{N_S} + IR_s}{R_{SH}} - I \tag{5.10}$$

First, the hourly current versus voltage and power versus voltage characteristics of a PV array are obtained for whole day's worth of data, as shown in Figure 5-9 and Figure 5-10. Figure 5-11 and Figure 5-12 illustrate a three-year time span. In the plots, each curve is produced by using hourly temperature and radiation measurements. In addition, the curves show the effect of both temperature and radiation on the hourly output current *(I)*, voltage *(V)*, and power *(P)*. These results are similar to those found in [132], [133].

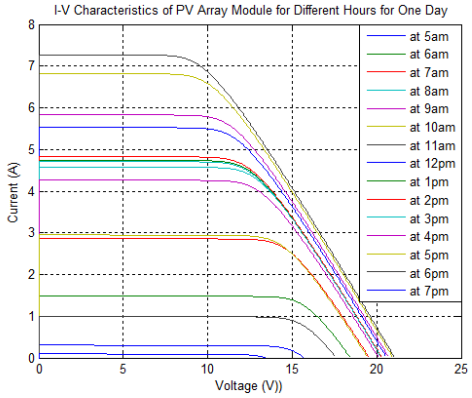

Figure 5-9 I-V characteristic of PV array module

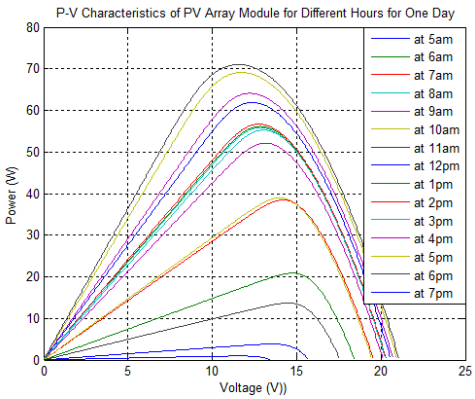

Figure 5-10 P-V characteristic of PV array module

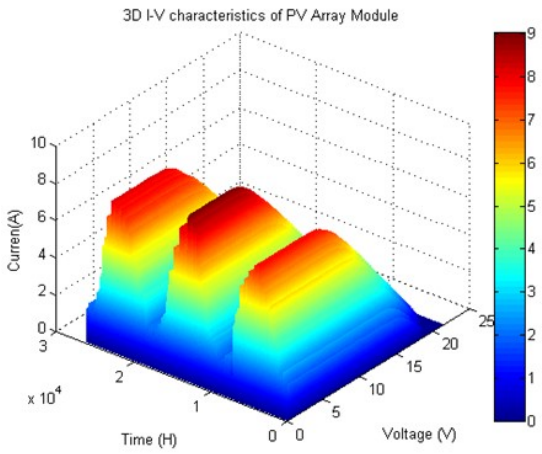

Figure 5-11 I-V characteristic for three years

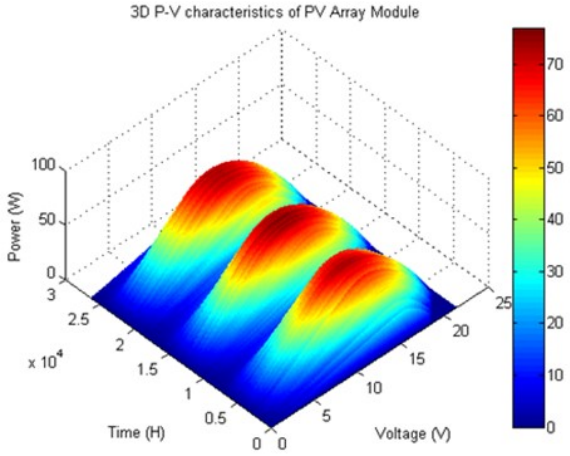

Figure 5-12 P-V characteristic for three years

Secondly, for each curve, the maximum power point of the PV array can be determined from Figure 5-9 and Figure 5-10 for a whole day's worth of data. This permits the determination of the hourly output current *(I)* and voltage *(V)* at the maximum points of these curves for one day, as shown in Figure 5-13.

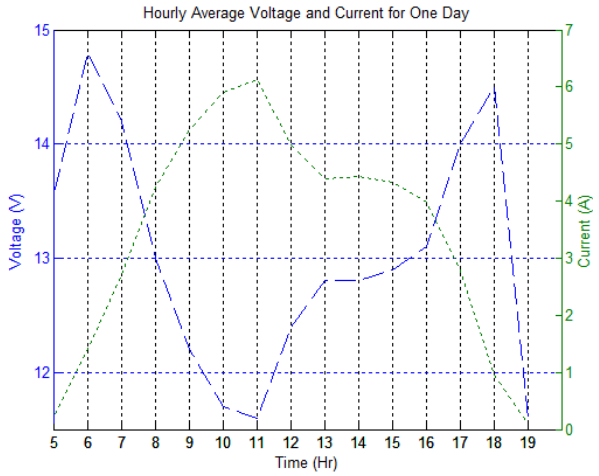

Figure 5-13 Maximum output current (*I*) and voltage (*V*)

Recently, different converter topologies have been used in this area. However, all converter designs are derived from fundamental converter techniques. The techniques used are a

square-wave inverter with 60 Hz switching, a square-wave inverter with blanking angle (firing angle or dead-zone angle) and 60 Hz switching, and pulse width modulation (PWM). For a PV system, a classic model used to convert a DC signal into an AC signal is shown in Figure 5-6. This model consists of four switching devices and one transformer, which connects the output of a converter to a Thevenin equivalent model of the power grid.

The transformer is represented by its exact equivalent circuit. Here I_m is the magnetization current of the transformer, I_1 is the primary current of the transformer, I_2 is the secondary current of the transformer, R_1 is resistance of the primary winding of the transformer, L_1 is inductance of the primary winding of the transformer, R_2 is the resistance of the secondary winding, L_2 is the inductance of the secondary winding, R_m is a model of the transformer core losses, L_m is the magnetization inductance, and n is the turns ratio of the transformer. The harmonic analysis of the inverter topology alone is performed subsequently. The state space representation of the whole model consists of three states (I, I_1, and I_m) [132]:

$$\begin{bmatrix} \frac{dI}{dt} \\ \frac{dI_1}{dt} \\ \frac{dI_m}{dt} \end{bmatrix} = \begin{bmatrix} \left(\frac{R_1 + R_m}{L_1}\right) & \frac{R_m}{L_1} & \frac{R_m}{L_1} \\ \frac{R_m n^2}{L_2} & \frac{R_m n^2}{L_2} & \frac{-(R_m + \left(\frac{R_2 + Z_o}{n^2}\right))n^2}{L_2} \\ \frac{R_m}{L_1} & \frac{-R_m}{L_1} & \frac{-R_m}{L_1} \end{bmatrix} \begin{bmatrix} I \\ I_1 \\ I_m \end{bmatrix} + \begin{bmatrix} \frac{V}{L_1} \\ 0 \\ 0 \end{bmatrix} u(t) \tag{5.11}$$

$$I_2 = \frac{I_1}{n} \tag{5.12}$$

$$V_o = I_2 Z_o \tag{5.13}$$

In this study, the model represents an isolated community. Here Z_o, the representative Thevenin equivalent impedance, is assumed to be a 10Ω resistive load, which is large enough to be studied. The effect of the reactive part of the impedance on the conversion stage is examined in [7]. Since the system is isolated, the effect of the grid voltage is neglected. The current provided by the PV modules is the current fed to the converter, and then to the load Z_o. The current performance is the same as the voltage performance, as a resistive load is used in this work. A variety of switching devices can be used for inverting the signal. For example, a MOSFET is suitable for high-frequency applications, and an IGBT is a switch that is appropriate for high-voltage applications [126].

5.6.2 Simulation of the PV DC-AC Conversion System

5.6.2.1 Square-wave inverter using 60Hz switching

To produce a 60 Hz output frequency, the output DC voltage of the PV cells is fed to the inverter. The inverter output is then fed to the transformer, which provides power to the load. The output voltage of the square-wave inverter alternates between V and –V at a frequency of 60 Hz, as shown in Figure 5-14. The transformer inductance is very small, has no effect on the output waveform, and has a DC offset and harmonic components.

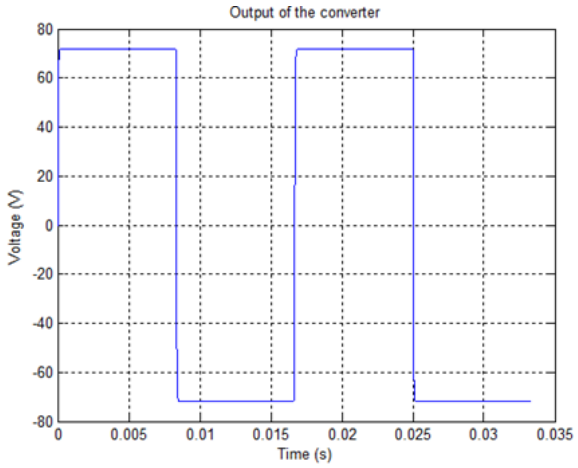

Figure 5-14 Output of the square -wave inverter at 60 Hz switching

The order and magnitude of harmonics for the AC output of the inverters are shown in Figure 5-15. The output voltage waveform contains only odd order harmonics. The most significant harmonics are the 3rd, to 11th; the other harmonics are insignificant in comparison. This is in agreement with results reported in the literature [134]-[136]. Table 5.1 shows the ratio of harmonic components to the fundamental component, as calculated from Figure 5-14.

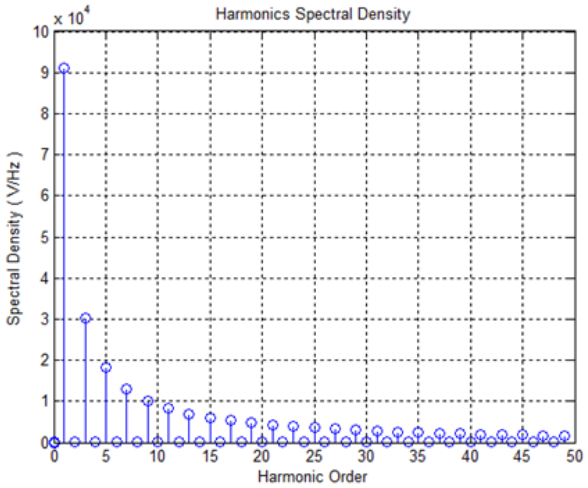

Figure 5-15 Harmonic order spectrum of the square -wave inverter at 60 Hz switching

Table 5.1 Ratios of the harmonic components to the fundamental component

Order	3^{rd}	5^{th}	7^{th}	9^{th}	11^{th}	13^{th}	15^{th}	17^{th}
Ratio (%)	33	20	14	11	9	7.6	6.6	5.6

In this work, a probability density function (PDF) is used to show the probability of occurrence of harmonic amplitudes. The harmonics produced during the conversion process can be modeled by using hourly solar radiation and temperature data, and a power inverter model. A simulation using hourly data over a three-year period shows the variability in amplitude of each harmonic component. This study of the harmonic distribution can aid in the effective design of an adaptive filtering system. The study also provides the probability density function for the fundamental component for each hour. This helps to determine the storage system capacity, including sizing. Accurate values can improve the performance and service life.

In addition, distribution fitting is used to find a probability distribution model that describes the frequency of occurrence of the magnitude of the fundamental frequency and harmonic components of the inverted waves. Many probability distributions were used, including beta, Birnbaum-Saunders, exponential, extreme value, gamma, generalized extreme value, generalized Pareto, inverse Gaussian, logistic, log-logistic, lognormal, Nakagami, normal, t location-scale and Weibull distributions [137]. The best four probability distributions were selected and sorted with regard to the Bayesian information criterion, based on the values of the negative of the log likelihood (NLogL).

Figure 5-16 shows the probability density function for the fundamental and harmonic components. It is concluded that the fluctuations of the even order harmonics over time are

too small to be considered, in comparison to the odd order harmonics. In addition, the odd harmonic components dominate and vary significantly. From Figure 5-16 it is concluded that:

1. The fundamental component has the greatest amplitude and a wide range of spectral density. The 3rd and 5th harmonics have a wider range of spectral density than is the case with other harmonics.

2. The fundamental, 3rd and 5th components exhibit the greatest probability density around (11.85, 3.85, and 2.3)$\times 10^4$ v/Hz respectively, ranging from 1.4×10^{-4} and 7×10^{-4}. However, the PDF for the 2nd, 4th and 6th components is equal to 0.038. These values can assist in the design of filter parameters to eliminate or minimize undesired harmonic components.

3. The ratios of the spectral density range of the 3rd and 5th harmonics to the fundamental are approximately equal to 4.3/13.12= 32.8% and 2.65/13.12= 20.2% respectively. These values agree with those indicated in Table 5.1.

4. The PDF patterns for the fundamental and odd harmonic components are very similar, with a different range of harmonic spectral density. Moreover, the even harmonic components have the same PDF pattern.

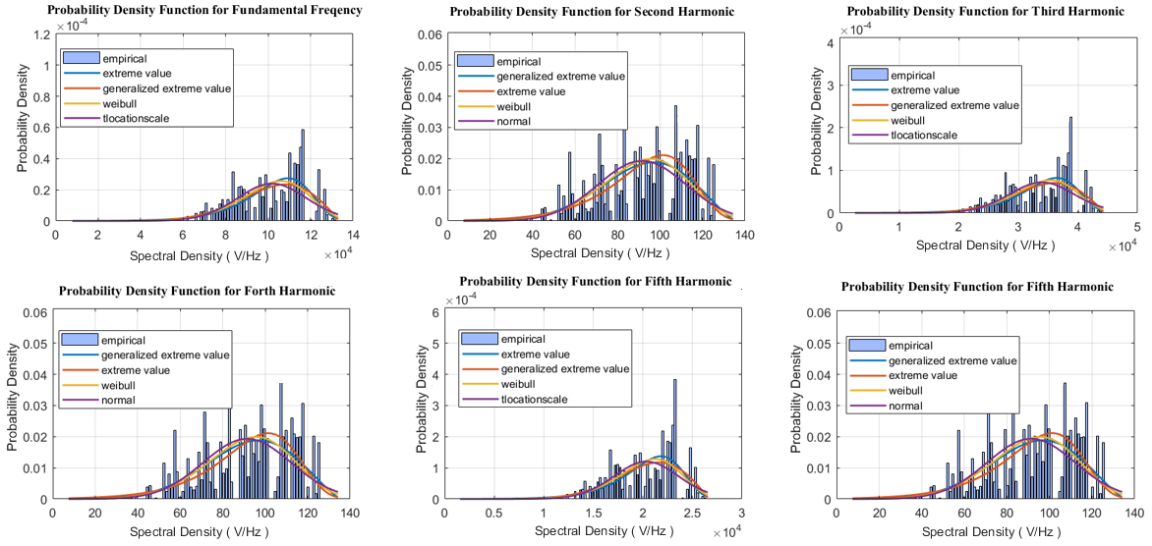

Figure 5-16 Probability density function and fitted distribution for the fundamental and harmonics of a square-wave inverter with 60 Hz switching

The probability distributions with the best fit for the fundamental component and odd harmonics are the extreme value, generalized extreme value, Weibull and t- location-scale distributions. However, the probability distributions with the best fit for the even harmonics are the generalized extreme value, extreme value, Weibull and normal distributions. The distributions with the best fit and their parameters are listed in sorted order in Table 5.2.

Table 5.2 Fitted distributions for fundamental and harmonic components, and their parameters for square –wave inverter at 60 Hz switching

Distribution Name	Parameters values for Fundamental Frequency	Parameters values for 3rd harmonic	Parameters values for 5th harmonic
'Extreme value'	location (mu) =109353.79 Scale (sigma) =13417.05	location (mu) =36434.72 Scale (sigma) =4470.344	location (mu) =21841.02 Scale (sigma) =2679.801
'Generalized extreme value'	Shape (k)=-0.508 Scale (sigma)=18391.99 Location (mu)= 97282.35	Shape (k)= -0.5081 Scale (sigma)=6127.902 Location (mu)= 32412.619	Shape (k)= -0.508 Scale (sigma)=3673.434 Location (mu)= 19429.810
'Weibull'	Scale(A)=108316.19 Shape(B)=7.45	Scale(A)= 36089.010 Shape(B)= 7.484	Scale(A)= 21633.776 Shape(B)= 7.484
't-location-scale'	Location(mu)= 101875.14, Scale(sigma)=16484.72, Degree of Freedom(Nu)=27.72	Location(mu)= 33942.930 Scale(sigma)= 5492.496 Degree of Freedom(Nu)= 27.72	Location(mu)= 20347.250 Scale(sigma)= 292.610 Degree of Freedom(Nu)= 27.73
Distribution Name	**Parameters values for 2nd harmonic**	**Parameters values for 4th harmonic**	**Parameters values for 6th harmonic**
'Generalized extreme value'	Shape (k) = -0.4376 Scale (sigma)=21.924 Location (mu)= 85.77	Shape (k) = -0.437 Scale (sigma)=21.907 Location (mu)= 85.728	Shape (k) = -0.437 Scale (sigma)=21.881 Location (mu)= 85.636
'Extreme value'	location (mu) =101.432 Scale (sigma) =17.427	location (mu) =101.369 Scale (sigma) =17.416	location (mu) =101.258 Scale (sigma) =17.397
'Weibull'	Scale(A)= 99.583 Shape(B)= 5.292	Scale(A)= 99.521 Shape(B)= 5.292	Scale(A)= 99.412 Shape(B)= 5.293
'Normal'	Location(mu)= 91.562 Scale(sigma)= 20.6839	Location(mu)= 91.506 Scale(sigma)= 20.669	Location(mu)= 91.406 Scale(sigma)= 20.643

In this case, the total harmonic distortion is approximately 47%. This is a high level, which can be expected to have negative impacts, as previously discussed.

Many techniques are available to reduce the harmonics, including the use of filtering systems, multilevel inverters, and changing the blanking angle of the switches or PWM [57], [126], [136], [138], [139].

5.6.2.2 Square-wave inverter using 60Hz switching and blanking angle

By changing the blanking angle (firing angle or dead-zone angle) of the switches of the square-wave inverter, the harmonic magnitude can be controlled. This results in changing the total harmonic distortion (THD). Figure 5-17 shows the THD obtained for different blanking angles, indicating that the optimum blanking angle to produce the minimum THD is approximately 24^o.

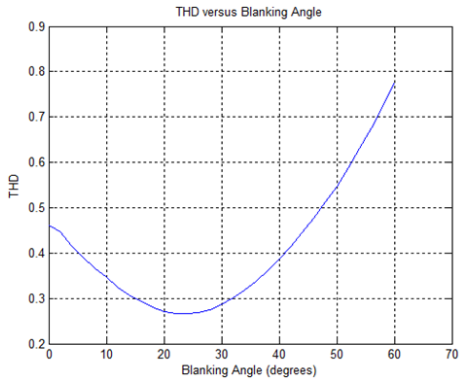

Figure 5-17 THD for different blanking angles

The AC output of the inverter for a specific radiation and temperature value is given in Figure 5-18. Figure 5-19 illustrates the harmonic magnitudes, and Table 5.3 shows the ratios of harmonic components to the fundamental component.

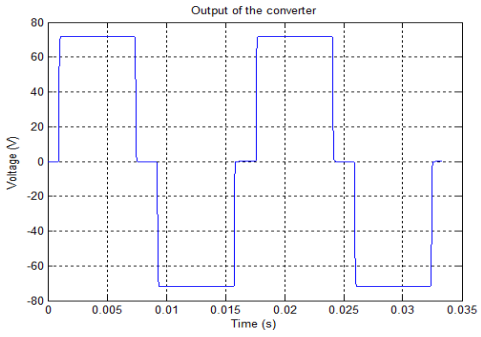

Figure 5-18 Output of inverter with blanking angle of 24^o

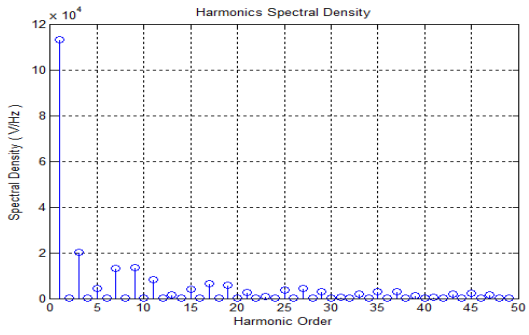

Figure 5-19 Harmonic order spectrum

From Table 5.3, it can be seen that the odd harmonic components are reduced in comparison to the previous case, and that the most dominant harmonics are the 3rd, 7th, 9th, 11th, and 17th.

Table 5.3 Ratios of the harmonic components to the fundamental component

Order	3rd	5th	7th	9th	11th	13th	15th	17th
Ratio (%)	17.7	4	11.6	11.8	7.3	1.3	3.5	5.7

Figure 5-20 shows the probability density function for the fundamental frequency and the odd/even order harmonics, for various radiation and temperature values over a three-year time span. The analysis is carried out for a certain blanking angle. It can be concluded that fluctuations of the even order harmonics are still negligible in comparison to those of the odd order harmonics. From Figure 5-20, it is concluded that:

1. The fundamental frequency has a wider range.
2. For the fundamental and the 3rd,5th, 7th, 9th, and 17th harmonics, the greatest probability density occurs at (13.79, 2.439, 0.5152,1.606, 1.623 and 0.8001)$\times 10^4$ v/Hz respectively, and is equal to 5.4, 29.4, 120.4, 43.7, 47.3, 16.3, 72.4)$\times 10^{-5}$.
3. The ratios of the spectral density range of the 3rd, 5th, 7th, 9th, and 17th harmonics to the fundamental are approximately equal to 2.79/15.38= 17.7%, 0.59/15.38= 3.7%, 1.84/15.38= 11.6%, 1.84/15.38= 11.6% and .91/15.38= 5.7% respectively. These values agree with those shown in Table 5.3.
4. The PDF patterns for the fundamental and odd harmonic components are very similar, with a different range of harmonic spectral density. In addition, the even harmonic components have the same PDF pattern.

In this case, the total harmonic distortion is approximately 28.2%.

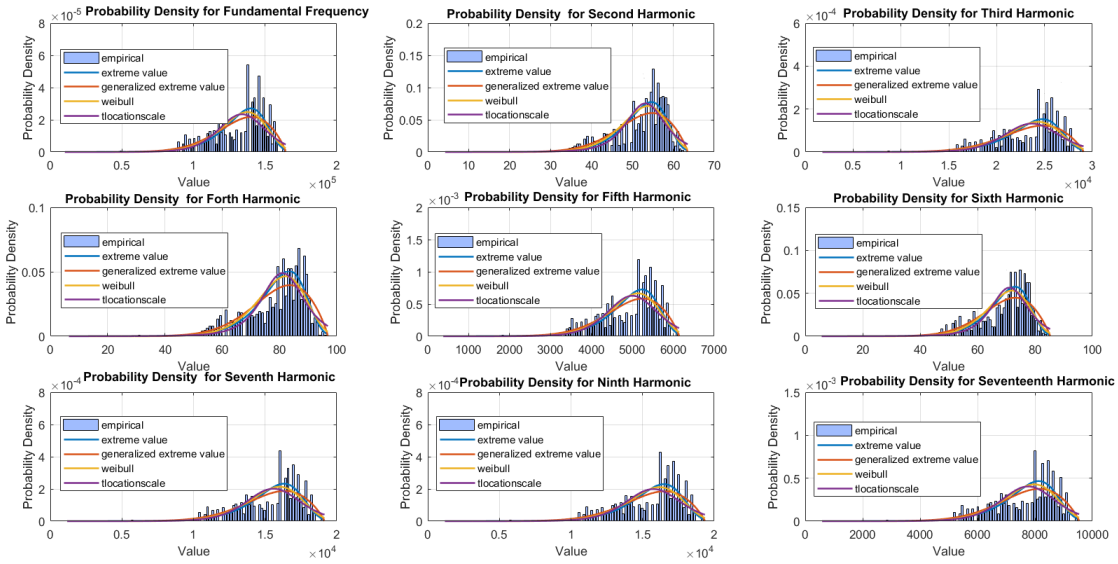

Figure 5-20 Probability density function and fitted distribution for the fundamental and harmonics of a square-wave inverter with 60 Hz switching, with blanking angle

The probability distributions with the best fit for the fundamental component and odd and even harmonics are the extreme value, generalized extreme value, Weibull and t location-scale distributions. The distributions with the best fit and their parameters are listed in sorted order in Table 5.4.

Table 5.4 Fitted distributions for fundamental and harmonic components, and their parameters for square –wave inverter at 60 Hz switching with blanking angle

Distribution Name	Parameters values for Fundamental Frequency	Parameters values for 2nd harmonic	Parameters values for 3rd harmonic
'Extreme value'	location (mu) =140064.6 Scale (sigma) =13589.43	location (mu) =54.64 Scale (sigma) =4.73	location (mu) =24777.88 Scale (sigma) =2404.697
'Generalized extreme value'	Shape (k)= -0.550 Scale (sigma)=20406.09 Location (mu)= 127308.98	Shape (k)= -0.5471 Scale (sigma)=7.341 Location (mu)= 50.096	Shape (k)= -0.550 Scale (sigma)=3610.521 Location (mu)= 22520.878
'Weibull'	Scale(A)= 139167.45 Shape(B)= 9.33	Scale(A)= 54.356 Shape(B)= 10.49	Scale(A)= 24619.09 Shape(B)= 9.336
't-location-scale'	Location(mu)= 133773.90 Scale(sigma)= 16479.90 Degree of Freedom(Nu)= 7.61	Location(mu)= 53.185 Scale(sigma)= 4.934 Degree of Freedom(Nu)= 3.596	Location(mu)= 23664.15 Scale(sigma)= 2916.674 Degree of Freedom(Nu)= 7.631
Distribution Name	Parameters values for 4th harmonic	Parameters values for 5th harmonic	Parameters values for 6th harmonic
'Extreme value'	location (mu) =83.379 Scale (sigma) =7.267	location (mu) =5234.872 Scale (sigma) =507.094	location (mu) =73.108 Scale (sigma) =6.382
'Generalized extreme value'	Shape (k)= -0.548 Scale (sigma)=11.216 Location (mu)= 76.435	Shape (k)= -0.550 Scale (sigma)=761.399 Location (mu)= 4759.013	Shape (k)= -0.536 Scale (sigma)=9.830 Location (mu)= 66.976
'Weibull'	Scale(A)= 82.942 Shape(B)= 10.452	Scale(A)= 5201.44 Shape(B)= 9.354	Scale(A)= 72.72 Shape(B)= 10.458
't-location-scale'	Location(mu)= 81.072 Scale(sigma)= 7.611 Degree of Freedom(Nu)= 3.695	Location(mu)= 5000.83 Scale(sigma)= 614.33 Degree of Freedom(Nu)= 7.55	Location(mu)= 71.11 Scale(sigma)= ,6.583 Degree of Freedom(Nu)= 3.587
Distribution Name	Parameters values for 7th harmonic	Parameters values for 9th harmonic	Parameters values for 17th harmonic
'Extreme value'	location (mu) =16311.302 Scale (sigma) =1582.068	location (mu) =16488.03 Scale (sigma) =1599.784	location (mu) =8128.489 Scale (sigma) =788.539
'Generalized extreme value'	Shape (k)= -0.550 Scale (sigma)=2375.832 Location (mu)= 14826.29	Shape (k)= -0.550 Scale (sigma)=2402.194 Location (mu)= 14986.51	Shape (k)= -0.550 Scale (sigma)=1184.059 Location (mu)= 7388.468
'Weibull'	Scale(A)= 16206.8 Shape(B)= 9.3426	Scale(A)= 16382.421 Shape(B)= 9.339	Scale(A)= 8076.44 Shape(B)= 9.341
't-location-scale'	Location(mu)= 15579.400 Scale(sigma)= 1918.157 Degree of Freedom(Nu)= 7.606	Location(mu)= 15747.44 Scale(sigma)= 1940.042 Degree of Freedom(Nu)= 7.620	Location(mu)= 7763.615 Scale(sigma)= 956.050 Degree of Freedom(Nu)= 7.610

5.6.2.3 Inverter with pulse width modulation (PWM)

In this case, PWM is used. The AC output of the inverter for a specific solar radiation and temperature value, with a switching frequency of 12 kHz, is given in Figure 5-21. The output more closely resembles a sine wave than is found with the waveforms produced in the previous cases, shown in Figure 5-14and Figure 5-18.

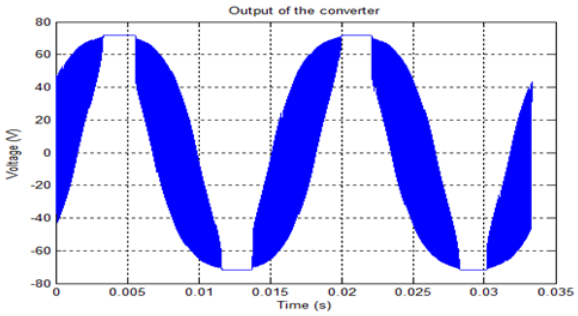

Figure 5-21 Output of the inverter with PWM

From Figure 5-22, it can be concluded that the magnitude of the even and odd order harmonics is negligible after the 198th order harmonic. Furthermore, Figure 5-23 and Figure 5-24 show that the dominant harmonics are around 12 kHz and 24 kHz.

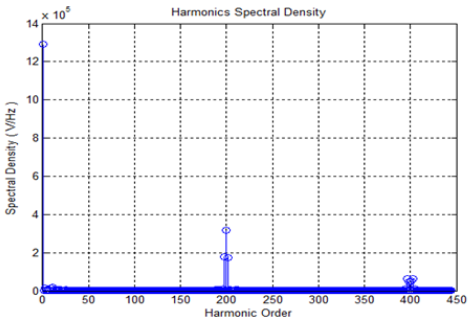

Figure 5-22 Harmonic order spectrum of inverter with PWM

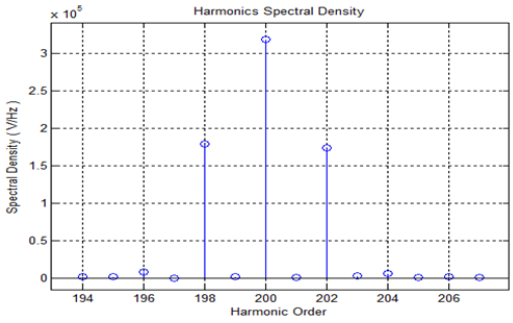

Figure 5-23 Harmonic order spectrum around 12kHz

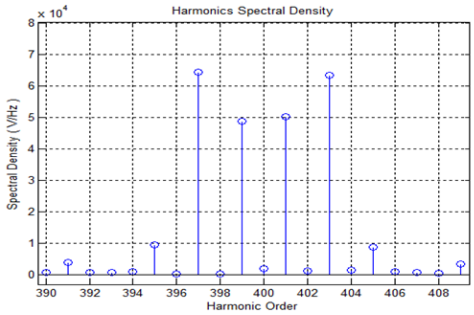

Figure 5-24 Harmonic order spectrum around 24kHz

From Table 5.5, it can be seen that the odd harmonic components are significantly reduced in comparison to the previous cases. However, some of the higher order harmonics, especially around the 12 kHz carrier frequency of the PWM and multiples of 12 kHz, have large magnitudes. Thus, PWM shifts the harmonics to higher frequencies. This makes the harmonics easier to handle.

Table 5.5 Ratios of the harmonic components to the fundamental component

Order	3rd	5th	7th	9th	11th	13th	15th	17th
Ratio (%)	1	0.6	0.3	1.1	1.4	0.4	0.2	0.1

Table 5.6 shows the ratios of higher harmonic components to the fundamental component when PWM is used. This leads to reduced filtering requirements, which is similar to results found in [57], [126], [138], [139]and [57], [126], [138], [139]. The harmonics shown in Table 5.6 are the most dominant harmonics, contributing approximately 60% of the THD. The rest of the harmonics, following the 403rd, contribute only 3% of the THD.

Table 5.6 Ratios of the harmonic components to the fundamental component

Order	198th	200th	202nd	397th	399th	401st	403rd
Ratio (%)	14	25	13.6	5.8	3.8	3.9	5.7

Figure 5-25 shows the probability density function of the fundamental frequency and the odd/even order harmonics for various radiation and temperature values over a three-year time span. From Figure 5-25, it is concluded that:

1. For the fundamental and the 198th,200th, 202nd, 397th, 399th, 401st and 403rd harmonics, the greatest probability density occurs around (15.58, 2.2, 3.8, 2.2, 0.74, 0.56, 0.58 and 0.74)$\times 10^{5}$ v/Hz respectively, and is equal to (.37, 2.65, 1.67, 2.65, 8.5, 13.3, 13 and 9.1)$\times 10^{-5}$.

2. The ratios of the spectral density range of the 198th, 200th, 202nd, 397th, 399th, 401st and 403rd harmonics to the fundamental are approximately equal to 2.4/17.1= 14.03%, 4.1/17.1=24%, 2.24/17.1=13.01%, 0.85/17.1=5.0 %, 0.62/17.1=3.6%, 0.64/17.1=3.7% and 0.82/17.1= 4.8% respectively. These values agree with those shown in Table 5.6.

3. The PDF patterns for the fundamental and dominant harmonic components are very similar, with a different range of harmonic spectral density. However, the fundamental component has a wide range compared to the harmonics, and the 200th harmonic has the widest harmonic range.

In this case, the total harmonic distortion is approximately 32.8%.

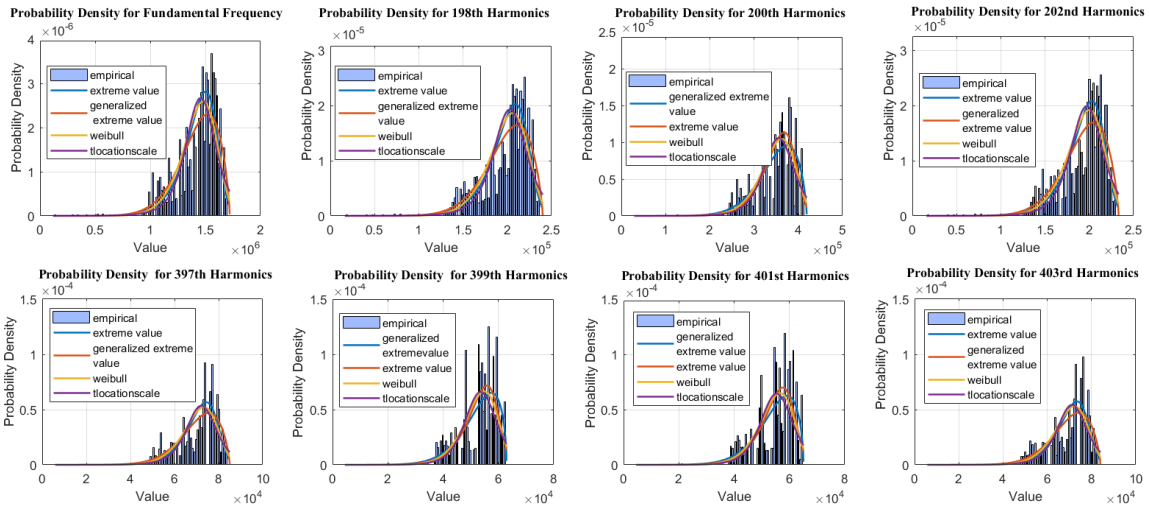

Figure 5-25 Probability density function for the fundamental and harmonics of an inverter with PWM

The probability distributions with the best fit for the fundamental component and the 198th, 202nd, 397th and 403rd harmonics are the extreme value, generalized extreme value, Weibull and t location-scale distributions. However, the probability distributions with the best fit for the 200, 399th and 401st harmonics are the generalized extreme value, extreme value, Weibull and t location-scale distributions. The distributions with the best fit and their parameters are listed in sorted order in Table 5.7.

Table 5.7 Fitted distributions for fundamental and harmonic components, and their parameters, for PWM

Distribution Name	Parameters description	Parameters values Fundamental Frequency	Parameters values For 198th harmonic	Parameters values For 202nd Harmonic	Parameters values For 397th Harmonic	Parameters values For 403rd harmonic
'Extreme value'	location (mu) Scale (sigma)	1502197.44 130825.17	209141.56 18187.04	203039.85 17667.20	74394.37 6481.83	73397.54 6403.84
'Generalized extreme value'	Shape (k) Scale (sigma) Location (mu)	-0.591 199896.73 1382379.82	-0.584 27838.14 192354.48	-0.582 27032.44 186714.58	-0.598 9894.39 68494.27	-0.592 9768.85 67538.89
'Weibull'	Scale(A) Shape(B)	1494344.97 10.48	208050.81 10.49	201979.97 10.48	74005.22 10.47	73012.72 10.46
't-location-scale'	Location(mu) Scale(sigma) Degree of Freedom(Nu)	1457058.32 140587.33 4.10	203000.88 19422.65 3.99	197070 18861.21 3.99	72124.65 7021.40 4.21	71155.95 6926.529 4.20

Distribution Name	Parameters values	Parameters values for 200 Harmonic	Parameters values for 399th harmonic	Parameters values for 401st harmonic
'Generalized extreme value'	Shape (k) Scale (sigma) Location (mu)	-0.614 49110.69 339022.033	-0.669 7648.68 51505.05	-0.656 7849.48 53118.62
'Extreme value'	location (mu) Scale (sigma)	367947.65 10.37	55771.93 5131.50	57564.73 5261.22
'Weibull'	Scale(A) Shape(B)	365989.035 0.48	55454.13 9.98	57240.20 10.048
't-location-scale'	Location(mu) Scale(sigma) Degree of Freedom(Nu)	355806.43 35719.31 4.62	53586.76 5789.37 5.78	14555353.76 5927.36 5.63

5.6.3 Modeling of PV DC-AC Conversion System Using Different Loading Conditions

The introduction of inductance to the load when a switching model with zero blanking angle is used causes the output voltage waveform of the inverter to become smoother. Figure 5-26 shows the output voltage waveforms and harmonic spectral densities for different inductor values. When the inductor value is equal to .005 H, the output voltage becomes smoother. The harmonic spectral densities for the 3rd, 5th and 7th harmonics are approximately 30%, 15% and 9%, as shown in Figure 5-27. Therefore, there is no DC component. When the inductor value is increased to 0.01 H, the output voltage again becomes smoother. The harmonic spectral densities for the 3rd, 5th and 7th harmonics become approximately 24.2%, 10.6% and 5.9% of the fundamental component,

respectively. These values are lower than is the case when L=0.005. In addition, the spectral density for the fundamental component decreases. However, the DC component and lower even harmonics appear in the harmonic spectral density. When the inductor value is increased to 0.02 H, the spectral densities for the 3rd, 5th and 7th harmonics become approximately 17.8%, 7.3% and 4% of the fundamental component, respectively. These values are lower than those in the previous cases when L=0.005 H and L=0.01 H. However, the influence of the DC component and lower even harmonics becomes larger. The total harmonic distortion is measured for different inductor values, as shown in Figure 5-28.

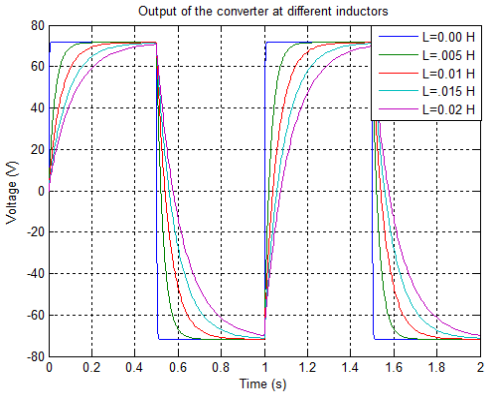

Figure 5-26 Output voltage waveforms for different inductor values

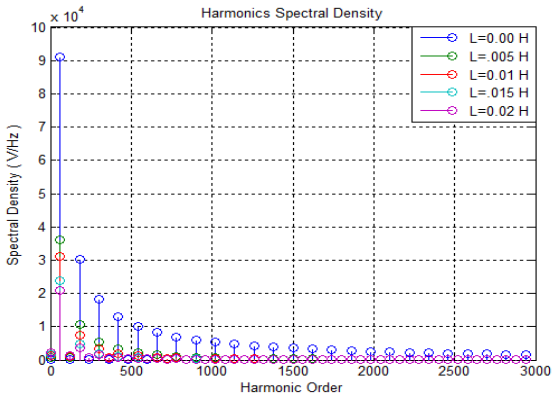

Figure 5-27 Harmonic spectral density for different inductor values

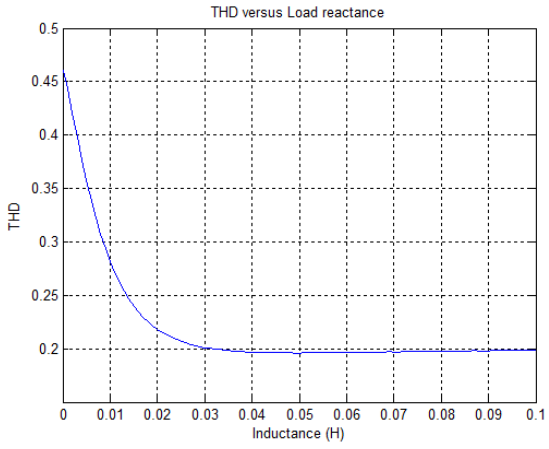

Figure 5-28 Total harmonic distortion for different inductor values

5.6.4 Effects of Weather Condition on PV Harmonics

The ratio of each harmonic to the fundamental components of the output over three years is similar for the first conversion technique, as listed in Table 5.8. This indicates that the variation in weather conditions does not affect this ratio. This applies for other two conversion techniques.

Table 5.8 Ratios of the harmonic components to the fundamental component over three years

Order	3^{rd}	5^{th}	7^{th}	9^{th}	11^{th}	13^{th}	15^{th}	17^{th}
Ratio (%)	33	20	14	11	9	7.6	6.6	5.6

However, the amplitude of the fundamental and harmonic components (spectral density) changes when the weather conditions change, as shown in Figure 5-29. This applies to these two conversion techniques. Figure 5-29 shows that when the first conversion technique is used, the amplitude of the output is large when the solar radiation level, and the temperature are low. On the other hand, the amplitude of the fundamental and harmonic components decreases when the temperature increases. Knowing the amplitude of the fundamental and harmonic components, especially in extreme weather conditions, is helpful for determining parameters to design an adaptive filter and size a storage system.

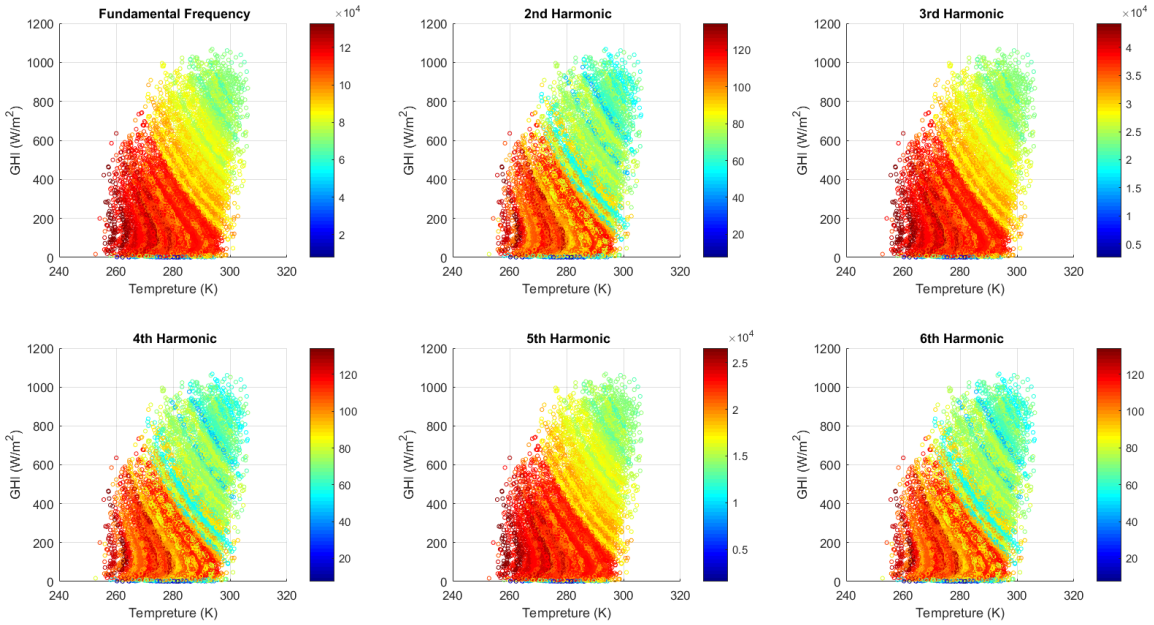

Figure 5-29 Spectral density of the fundamental and harmonics components of the output over three years at different temperature and solar radiation values

5.6.5 Conclusions

The probability density functions for the fundamental frequency and several of the odd/even order harmonics for the three methods of inversion are evaluated. For the three conversion techniques, the probability density of the even order harmonics is too small to be considered in comparison to the odd order harmonics. The odd order harmonics dominate and have a wide variance. The use of PDF shows that in comparison with other techniques, the magnitude of the fundamental frequency is significantly larger, and the ratio of the harmonic components to the fundamental is small when the PWM inversion method is used. These results agree with previous studies that have been carried with a different method. Suitable probability distribution models are determined for each fundamental and harmonic component of the signal, for the three different techniques.

The results show that the variability in the amplitude of each harmonic component is beneficial for placing an adaptive filtering system and sizing the storage system capacity.

The size of a PV storage system could be bounded by lower and upper limits. The use of PDF can assist in finding the boundaries of the fundamental and the magnitudes that occur more frequently. This can aid in improving the storage system efficiency. Adaptive filters are needed for PV systems when some parameters of the desired operation are changed. Thus, adaptive filters need to modify the transfer function, depending upon the new operating conditions. The goal of the adaptation is to adjust the characteristics of the adaptive filter. Because PDF studies help to determine the boundaries of each harmonic and which harmonic magnitude occurs more frequently, this can contribute to the design of the adaptive filter. Furthermore, it is shown that the variation in weather conditions does not influence the ratio between each harmonic and the fundamental component of the output. However, it influences the amplitude of the fundamental and harmonics.

CHAPTER 6 LOAD MANAGEMENT

6.1 INTRODUCTION

On the electricity side, demand has been continuously increasing, which causes capacity problems in the power grid. It is impossible to continue adding new conventional power generation supplies to meet these demands. This leads to the inclusion of power production from renewable energy sources. The renewable energy sources most commonly used in power generation are large wind turbines and PV systems [140]-[143].

The use of renewable energy from sources near the point of consumption results in reduced transmission and demands on the capacity of the distribution network. However, such energy sources depend on weather conditions, which can lead to imbalances between power generation and consumption. Rapid responses from power plants and energy storage systems are required to overcome these issues. However, such solutions are inefficient, especially at times of peak consumption.

A more efficient solution is load management, or demand side load management (DSM). This process aims to adjust the load rather than increasing the output of power stations. This can be done by peak shaving and by shifting the load to more favourable periods [140], [143]. DSM can help to reduce emissions and costs through the use of fewer generators and power sources. This also reduces network instability and helps to increase power efficiency [144]. The use of appropriate load management by power utilities familiarizes consumers with load shedding, to avoid rolling blackouts.

DSM can be achieved by models and devices that take into consideration the physical properties of the distribution network, such as the topology, capacity, and lines, in addition to the load behaviour. DSM can also take into account changes in the weather.

Most DSM applications are based on radio frequency and powerline communications, such as smart meters.

6.2 LITERATURE REVIEW

The development of load management technologies has increased rapidly in recent years in different sectors, including households and industry. In 1972, Boeing developed a monitoring system for security, fire and medical systems which used digital transmissions [145].

The Alabama Power Company developed a load management system which has the ability to monitor power consumption by monitoring the watt power meter disc. This development gave the power plant the ability to prevent usage peaks for water heaters and air conditioners [146].

In 2005, Florida Power and Light had the largest residential load control system, controlling 1000 MW of electrical power for 800,000 loads. This initiative minimized the construction of new power plants [147].

A predictive scheduling model with a DSM program was developed by Jawad, et al [148] for a residential house. The purpose of this model was to optimize coordination between the grid, PV panels, battery storage, and the load demand, in addition to ensuring the power supply for all residential applications by predicting loads 24 hours in advance and categorizing the type of load. The model helps to find a balance between the comfort level of consumers and energy prices. A fuzzy logic decision maker (FDM) was implemented to

offer consumers the flexibility of using a device according to their needs throughout the day. The DSM program reduces peak loads and sizing of the PV battery.

A mathematical model was developed by Sebastian, et al [149] for a residential house. This model helps to optimize the electricity generation production site of a local energy system, with a small combined heat and power (CHP) plant, a battery system, and a PV system. The purpose of this model is to reduce the peak load and to adjust the power generation load curve.

A dynamic simulation model was developed by Alessia, et al [150] for an industrial building in Italy which has a thermal energy storage (TES) system coupled with heat pumps. The model implements DSM, which shifts the electricity demand for cooling and heating purposes from peak hours to off-peak hours. The purpose of this model is to take advantage of PV overproduction during weekends by charging the storage system outside of working hours, and then using the stored thermal energy during weekdays. In addition, this reduces heat pump usage during peak hours, when electricity prices are higher. This strategy helps to take advantage of PV energy production and lower electricity grid prices during the weekend.

A community energy storage (CES) system was optimized by David, et al [151] to achieve PV energy time shifting and demand load shifting simultaneously. The purpose of the model is to optimize battery performance when the battery is charging and discharging. This study suggested when the PV energy should be integrated with the CES, and CES discharging times at peak times. In addition, a type of battery was chosen to optimize the demand load and the performance and profitability of PV generation.

6.3 USING NEURAL NETWORKS FOR LOAD MANAGEMENT APPLICATION

Many approaches can be taken to maximize the benefits of PV, PVT and thermal systems. One method is to change the ratio of PV cells in a PVT system, as described earlier. Another approach is to accommodate the amount of energy generated by adjusting the behavior of the load. This is referred to as load management. A solar boiler system, a thermal system for heating water, was used to analyze and develop a load management application [2].

6.3.1 Overview of Solar Boiler System

A solar boiler system is used to heat water in combination with a conventional domestic water heating system. Cold water is initially heated by the solar boiler, and is then transferred to a conventional heating system for final heating. Oil, electricity, propane, or natural gas can be used to power the conventional system. A solar boiler system consists of solar collectors, solar water storage, and a PV module, as shown in Figure 6-1 [152].

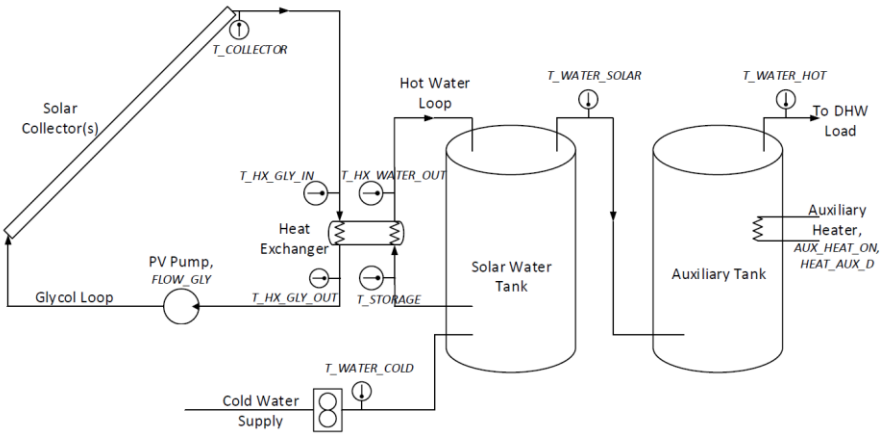

Figure 6-1 Solar Boiler System layout [152]

The black metal absorber is heated by solar energy, which is collected by solar collectors. Antifreeze solution, propylene glycol and water, is heated and circulated between the collectors and the solar boiler. It is pumped through the collector and returns to the solar boiler via the pump. Heat is then transferred from the antifreeze solution to the storage tank, to heat the water [152].

6.3.2 Simulation and Analysis

Use of the solar boiler at appropriate times can reduce the requirement for conventional energy sources. On average, only 30% of the solar energy produced is utilized by the solar boiler system. The annual solar energy for the collector, and the solar storage and hot water for different sizes of collectors are shown in Table 6.1 [153].

Table 6.1 Annual solar energy on collector and to solar storage [153]

System	Solar Energy (kwh)		
	On collector	To solar storage	%
SB64(6 m^2)	5752	1964	34.1
SB32(3 m^2)	3099	1467	29.1%

SmartSaver, a load management application, was developed to maximize utilization of the solar boiler system through the scheduling of household activities. This application uses the second proposed model for GSR_H and GSR_D prediction, and is fed the weather variables directly from a weather website.

The most common household activities that use hot water are washing dishes, using the washing machine, and taking a shower or bath. The average behaviour of consumers in performing household activities is shown in Table 6.2 for a family of four.

Table 6.2 Average consumer behaviour in performing household activities

System	Weekly Usage / Time (Hour)
Dishwasher	7/2.5
Washing machine	5/0.5
Shower	12/0.25
Bath	4/0.5

The steps involved in developing the application are shown in Figure 6-2. In the first step, live weather data are provided from a weather website via an Application Program Interface (API) [154]. In the second step, the GSR_H and GSR_D are predicted for ten days. The cumulative hourly energy is then calculated for ten days. Results for Nov 2nd to Nov 11th are shown in Figure 6-3 to Figure 6-12. In addition, the cumulative daily energy, and optimal days in the ten-day period are shown in Figure 6-13, and are given by [155]:

$$Generated\ Energy\ (kwh) = Power\ (\text{kW})\ \text{x time (hours)} \tag{6.1}$$

$$\text{Power (kW)} = GSR\left(\frac{\text{KW}}{m^2}\right) * (\text{COLLECTOR AREA})(m^2) \tag{6.2}$$

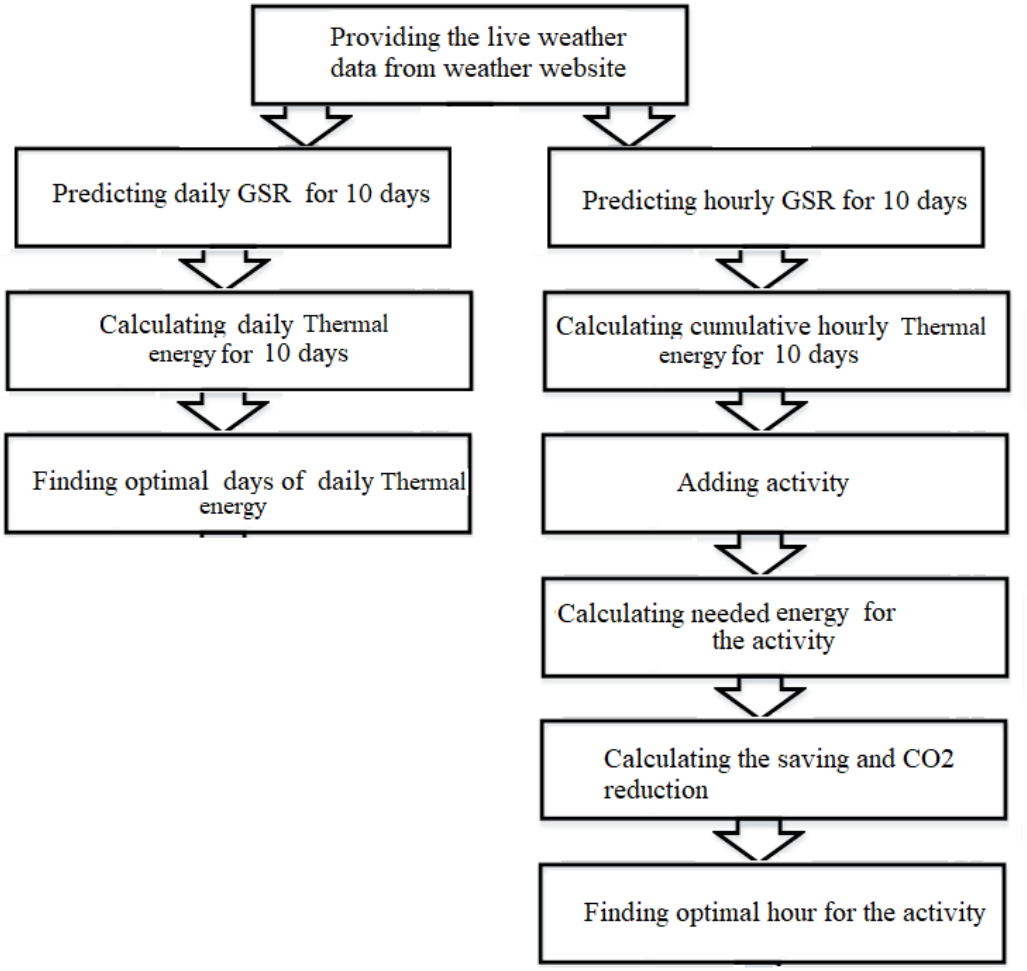

Figure 6-2 Steps of developing the application

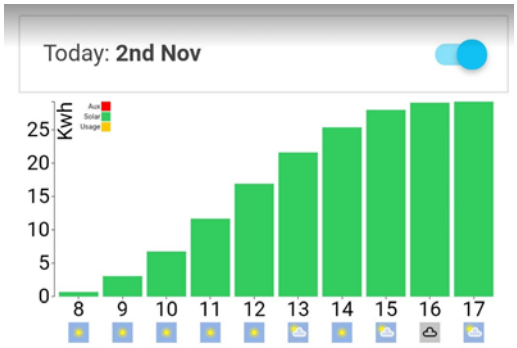

Figure 6-3 Cumulative hourly energy for Nov 2nd

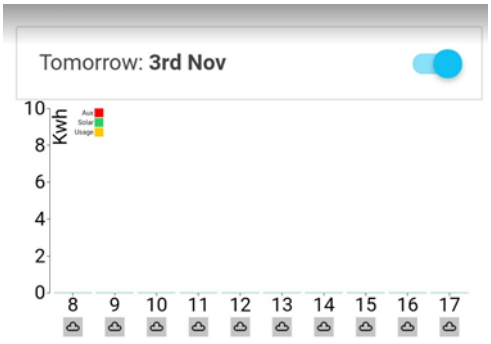

Figure 6-4 Cumulative hourly energy for Nov 3rd

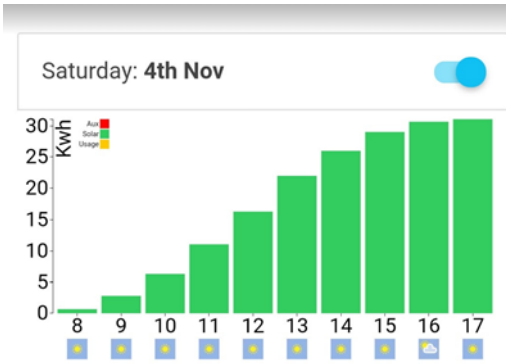

Figure 6-5 Cumulative hourly energy for Nov 4th

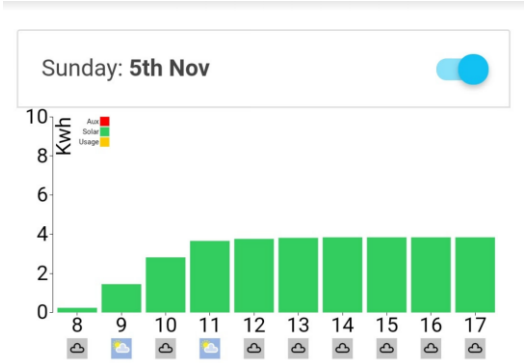

Figure 6-6 Cumulative hourly energy for Nov 5th

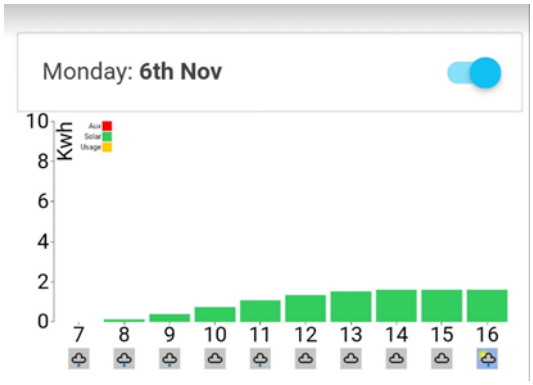

Figure 6-7 Cumulative hourly energy for Nov 6th

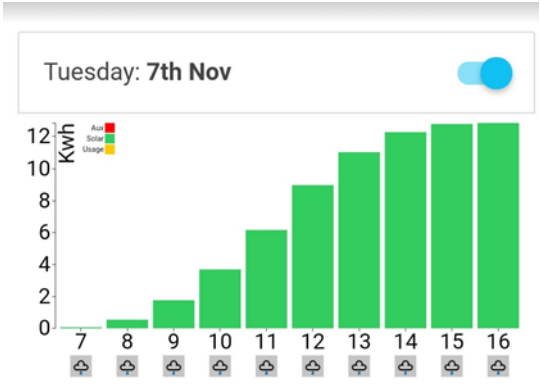

Figure 6-8 Cumulative hourly energy for Nov 7th

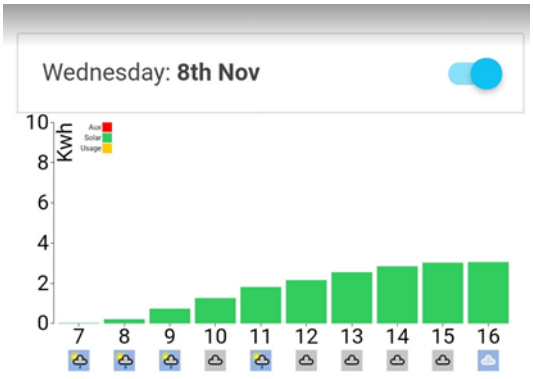

Figure 6-9 Cumulative hourly energy for Nov 8th

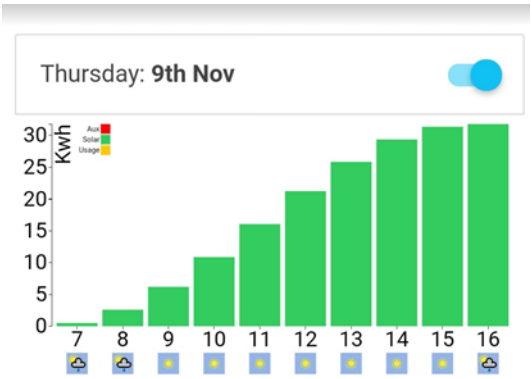

Figure 6-10 Cumulative hourly energy for Nov 9th

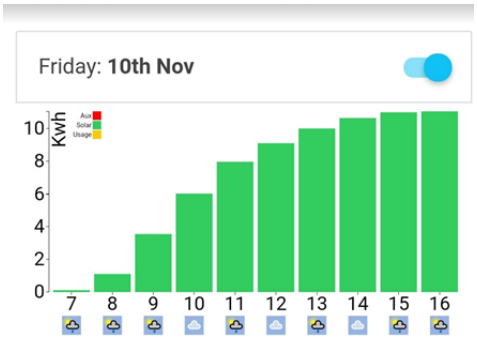

Figure 6-11 Cumulative hourly energy for Nov 10th

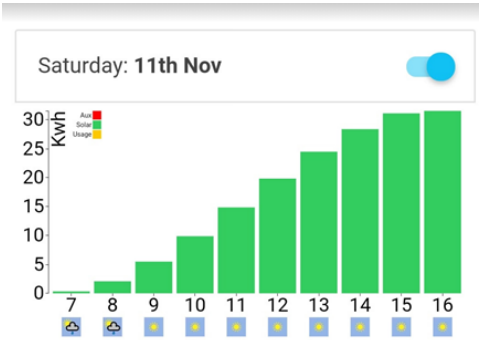

Figure 6-12 Cumulative hourly energy for Nov 11th

Figure 6-13 Daily energy and optimal days, for ten days

The next step is to add household activities which consume hot water, such as washing dishes, using the washing machine, and taking a shower or bath. Three selections are provided by the application, as shown in Figure 6-14.

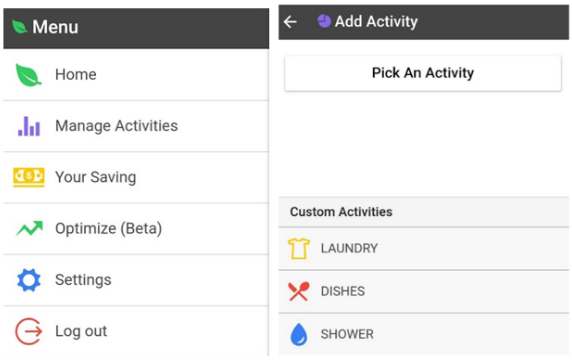

Figure 6-14 Selection of activities: first activity choice is a laundry

The first activity choice is a laundry. There are nine laundry modes, which are given in Table 6.3 [156], [157]. The energy required for heating a volume of water is calculated by [158]:

$$Energy\ (kwh) = V_{water} * \left(T_{upper} - T_{lower}\right) * \left(\frac{69.8}{60000}\right) \quad (6.3)$$

where V_{water} is the volume of water, T_{upper} is the temperature of the hot water, which depends on the type and mode of activity, and T_{lower} is the temperature of cold water. The results are shown in Figure 6-16 and Figure 6-17, for average hourly and daily values. A heater with 100% efficiency is assumed. In addition, tank losses are ignored. The temperature of the hot water that is provided by the solar boiler system is around 55^c. V_{water} and T_{upper} for each laundry mode are given in Table 6.3. Three laundry operation modes are shown in Figure 6-15.

Table 6.3 Nine laundry operation modes

Size	**Color**					
	Hot (white)		Warm (Color)		Cold (bright)	
	V_{water} (liter)	T_{upper} (Celsius)	V_{water} (liter)	T_{upper} (Celsius)	V_{water} (liter)	T_{upper} (Celsius)
Large	101.1	55^c	101.1	32^c	101.1	T_{lower}
Medium	79.16	55^c	79.16	32^c	79.16	T_{lower}
Small	58.08	55^c	58.08	32^c	58.08	T_{lower}

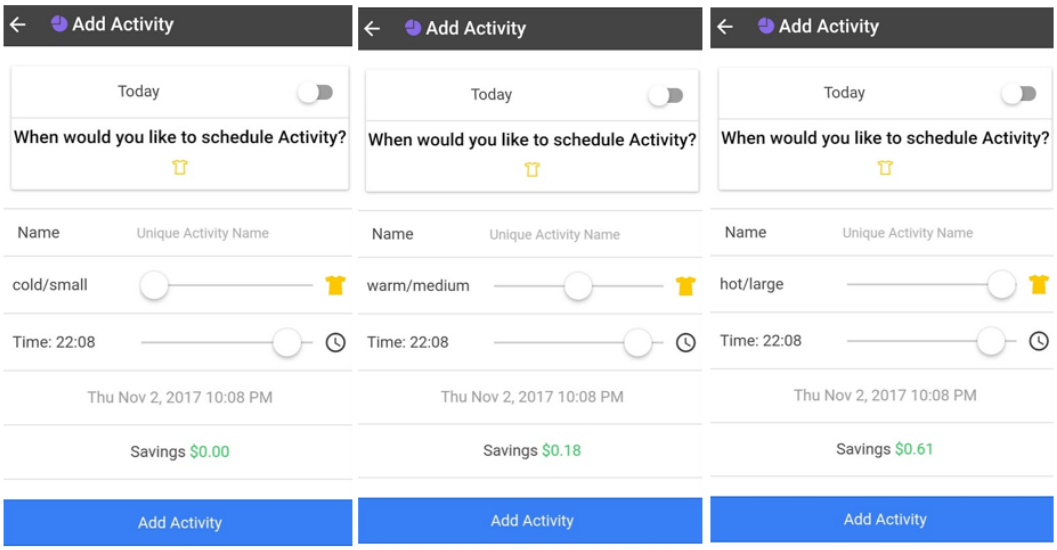

Figure 6-15 Three laundry operation modes

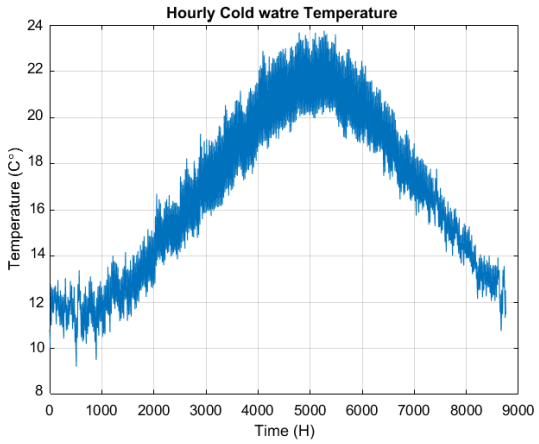

Figure 6-16 Average hourly temperature of cold water

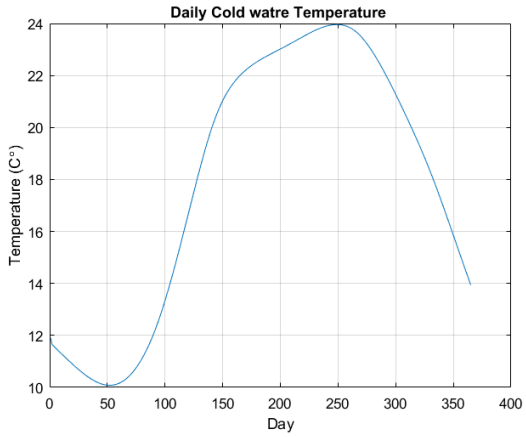

Figure 6-17 Average daily temperature of cold water

The next step is to find the optimal savings obtainable by scheduling the activity. This is done by changing the time bar and looking for maximum savings achieved when the load is completely supplied from solar energy, rather than from the auxiliary part. For example, when a hot, large mode is selected for a laundry operation, different savings amounts are shown for different hours, as illustrated in Figure 6-18. The cost of energy and CO_2 emission reductions are calculated, as given by [155]:

$$Cost\ of\ energy\ =\ Energy\ x\ Fuel\ cost \tag{6.4}$$

$$CO_2\ reductions\ =\ Energy\ x\ CO_2\ emissions \tag{6.5}$$

The fuel cost for electricity is equal to \$0.17 per kWh of electricity, and CO_2 emissions amount to 1.2 kg per kWh of electricity [83].

Figure 6-18a show a savings amount equal to zero when the time selected for the activity is 7:15 AM, because at that time no solar energy has been harvested. If the time selected for the activity is 8:45 AM, the savings amount is \$0.14, because at that time the water has been heated by a small amount of solar energy, and the rest of the energy is supplied by electricity, as shown in Figure 6-18b and Figure 6-19. However, if the time selected for the activity is 11:08 AM, the savings amount is \$0.61, because at that time the water has been completely heated by solar energy, with no electricity required, as shown in Figure 6-18c and Figure 6-20.

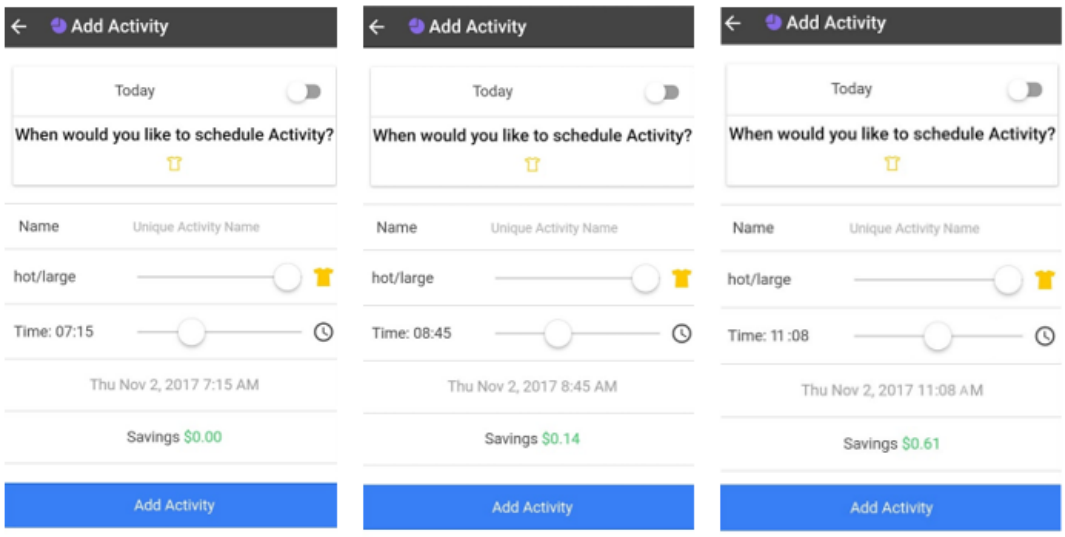

(a) (b) (c)

Figure 6-18 Different savings amounts at different times of day, for a hot, large laundry mode

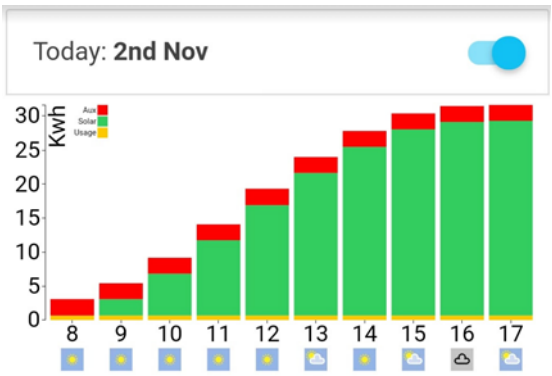

Figure 6-19 Energy when the time selected for the activity is 8:45 AM

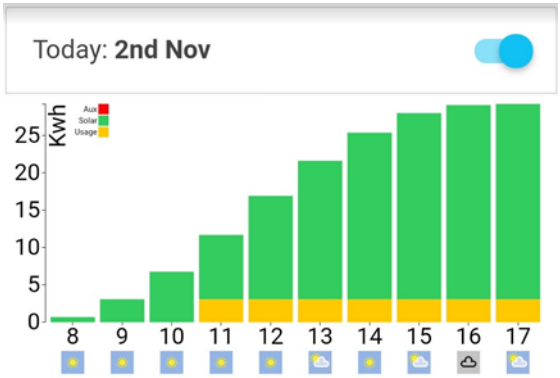

Figure 6-20 Energy when the time selected for the activity is 11:08 AM

The second activity choice is washing dishes. There are four dishwasher modes, as shown in Table 6.4 and Figure 6-21 [159], [160]. Equation (6.3) is used to calculate the energy required for heating a volume of water.

For each dishwasher mode, V_{water} and T_{upper} are given in Table 6.4. The four dishwasher operation modes are shown in Figure 6-21.

Table 6.4 Four dishwasher operation modes

Mode	V_{water} (liter)	T_{upper} (Celsius)
Heavy	29.2	55^c
Auto	18.95	55^c
Normal	15.81	55^c
Rinse		T_{lower}

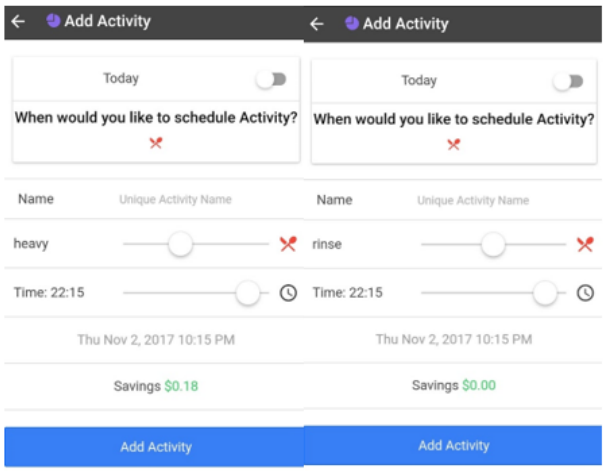

Figure 6-21 Two dishwasher operation modes

The third activity choice is taking a shower. The energy required for heating the water for this activity is calculated as follows:

$$Energy\ (kwh) = V_{avg\_water} * (T_{upper} - T_{lower}) * \left(\frac{69.8}{60000}\right) * time \qquad (6.6)$$

where V_{avg_water} is equal to 480 litres of water per hour [161], time is the length of the shower in hours, andT_{upper} is approximately 38^{c}. Two options for this activity are shown in Figure 6-22, which specifies the length and time of the shower.

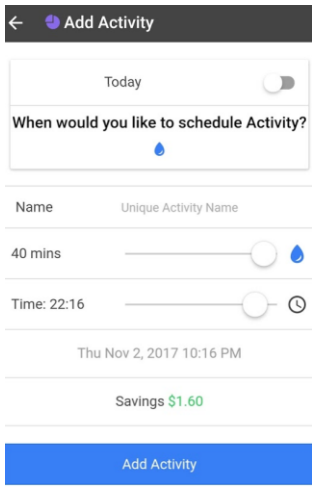

Figure 6-22 Two options for a shower

The application provides monthly and annual savings and CO_2 emission reductions, as shown in Figure 6-23. The use of hourly and daily energy data, as given in Figure 6-3 to Figure 6-13, helps to schedule activities based on the amount of savings and on which activities need to be performed on a daily basis. For example, laundry could be scheduled by looking at the daily energy chart in Figure 6-13, because laundry may be done on a weekly basis, with a frequency lower than that of the other activities. On the other hand, taking a shower or using the dishwasher could be scheduled based on the hourly energy charts given in Figure 6-3 to Figure 6-12.

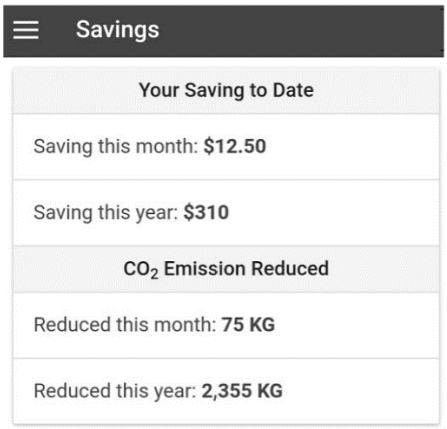

Figure 6-23 Monthly and annual savings and CO_2 emission reductions

Many machines, such as dishwashers and washing machines, are automated and could be controlled via mobile or smart home devices such as Google Nest. In addition, such machines have timers which could start them based on the results of the application. Thus, the application is compatible with other applications and tools.

6.3.3 Conclusions

The second proposed model for *GSR* prediction is used as part of a load management application. This application helps to maximize the utilized energy of thermal systems by

30%, to reduce the costs and emissions. This could be done by rescheduling household activities, such as washing dishes, using the washing machine, and taking a shower or bath, which consume hot water to days and times of day that have maximum solar energy.

Household activities could be scheduled based on the hourly and daily harvested energy charts. Laundry could be scheduled by looking at the daily energy chart, because laundry may be done on a weekly basis as an example. On the other hand, taking a shower or using the dishwasher could be scheduled based on the hourly energy charts.

CHAPTER 7 CONCLUSIONS

This chapter summarizes the results of this thesis and the contributions made. Suggestions for future work are also discussed.

7.1 CONCLUSIONS

In this thesis, weather conditions and their effects on solar energy applications and systems are investigated in order to maximize the utilized energy. The effect of weather conditions on harmonics generated in PV systems, and on the PV cell ratio in PVT systems is studied and analyzed.

Chapter 1 presents a brief overview, together with the contributions and objectives. In Chapter 2, an overview of renewable and solar energy is provided. Chapter 3 discusses the background of PV and PVT systems and the classification of these systems. In addition, the modeling, simulation, analysis and discussion of the effect of weather conditions on the PV cell ratio in PVT systems are presented. Chapter 4 discusses the concept of solar radiation forecasting using ANN and WNN. Moreover, new models for global solar radiation (GSR) prediction are introduced and compared with previous work in the field. While in Chapter 5, the causes and effects of harmonics and the measurement of harmonic levels are reviewed. Furthermore, the modeling, simulation, analysis and discussion of the effect of weather conditions on the generation of harmonics is presented. In Chapter 6, the concept of load management is defined. In addition, a new load management application is presented which could be valuable for maximizing cost savings and reducing emissions through the use of thermal systems.

This thesis is divided into four main parts. Various models are proposed in each part of the thesis. The first part comprises a PVT investigation based on PV coverage area and flow rate which can be summarized as follows:

- The OTE of PV systems is obtained for cases with constant (average) and variable (real) flow rates.
- The PV coverage ratio was varied from 1% to 100% to determine the maximum OTE of a PVT system.
- Three different time span levels are analyzed: macro, meso, and micro.
- The maximum OTE is obtained at different PV coverage ratios for each month. This contributes to maximizing the annual generated energy.
- The results show that the PV coverage ratio which produces the maximum OTE for constant and variable flow rate cases differs.
- Two different models based on two different cases of flow rate values are proposed.
- Specific PV coverage area values are proposed for each month to minimize annual CO_2 emissions.

The second part is concerned with weather forecasting, which can be summarized as follows:

- Three new models are proposed for predicting GSR_H and GSR_D by using ANN and WNN with the most effective combination of weather variables.
- It was found that cc, *hu,* and *T* are the best combination of variables for predicting GSR_H and GSR_D.

- The first proposed model was selected from combination models that used max *GSR* in addition to other weather variables.
- For the second proposed model, *cc* and max *GSR* were used as inputs for the first stage, and *hu* and *T* were used for the second stage of the model.
- For the third proposed model, *cc* and max *GSR* were used as inputs for the first stage, and *hu* and *T* were used in the second stage for GSR_{1H} and GSR_{1D} and GSR_e prediction.
- The Morlet wavelet function was used as a transfer function for the hidden layer of the GSR_e prediction.
- These models gave good results compared to others, although weather conditions in Halifax are relatively volatile in comparison to those of other research areas.

The third part focuses on harmonic analysis, which can be summarized as follows:

- The PDF for the fundamental frequency and the odd/even order harmonics for the three methods of inversion are evaluated.
- The PDF of the even order harmonics is too small to be considered for the three conversion techniques.
- The odd order harmonics dominate and have a wide variance.
- The magnitude of the fundamental frequency is significantly larger.
- Probability distribution models are determined for each fundamental and harmonic components of the signal, for the three different techniques.
- PDF can assist in finding the boundaries of the fundamental and the magnitudes that occur more frequently.

- The ratio between each harmonic and the fundamental components of the output is not influenced by the variation in weather conditions.
- The variation in weather conditions influences the amplitude of the fundamental and harmonics components.

The last part focuses on load management analysis and application which can be summarized as follows:

- A load management application was developed using the second proposed model for *GSR* prediction.
- This application helps to maximize the utilized energy of thermal systems by 30%, to reduce the costs and emissions.
- This could be done by rescheduling household activities which consume hot water to days and times of day that have maximum solar energy.
- Household activities could be scheduled based on the hourly and daily harvested energy charts.

7.2 FUTURE WORK

Due to the potential value of the findings and results of this study, further investigations are recommended which can be summarized as follows:

- Further investigations in relation to other weather variables and harmonics. Such future work could include practical adaptive filter system design.

- Hybrid model for solar radiation forecasting could also be studied and investigated. The approach used here could later be transferred to an experimental stage and could potentially be used in numerous practical applications.
- Tank losses could be included, and the results for the application could be saved and compared to real measurements to achieve greater accuracy, for load management applications.
- Maximum utilized energy could be found by optimization techniques, rather than manually changing the time of the activity.
- Using fuzzy clustering, such as Fuzzy K-Means and Fuzzy-C Means, to establish patterns of radiation, temperatures, and wind speed and produce a brief illustration of a system's behavior.

REFERENCES

[1] S. H. Shehadeh, H. H. Aly and M. E. El-Hawary, "New Approach on Solar Radiation Prediction Based on Neural Network Technique," *Renewable Energy, Submitted. (RENE-D-18-00864),* 2018.

[2] S. H. Shehadeh, H. H. Aly and M. E. El-Hawary, "A Proposed Intelligent Load Management Application Based on Solar Radiation Forecasting Model," *Electric Power Components and Systems, Submitted. (UEMP-2018-0218),* 2018.

[3] S. H. Shehadeh, H. H. Aly and M. E. El-Hawary, "Effect Of Weather Conditions on Harmonic Performance Of PV Inverters," *Electric Power Components and System, Submitted. (UEMP-2018-0201),* 2018.

[4] S. H. Shehadeh *et al*, "CO2 emissions reduction of photovoltaic thermal model using variable flow rate values," in *Electrical and Computer Engineering (CCECE), 2018 IEEE 31th Canadian Conference on, Accepted.* 2018.

[5] S. H. Shehadeh, H. H. Aly and M. E. El-Hawary, "Investigation of Photovoltaic Coverage Ratio for Maximum Overall Thermal Energy of Photovoltaic-Thermal System," *Renewable Energy, Submitted. (RENE-D-17-03932),* 2017.

[6] S. H. Shehadeh, H. H. Aly and M. E. El-Hawary, "Minimizing CO_2 emissions of photovoltaic thermal model in North America," in *Electrical and Computer Engineering (CCECE), 2017 IEEE 30th Canadian Conference On,* pp. 1-6. 2017.

[7] S. H. Shehadeh, H. H. Aly and M. E. El-Hawary, "PV harmonic distribution analysis for various conditions," in *Electrical and Computer Engineering (CCECE), 2016 IEEE Canadian Conference On,* 2016.

[8] S. H. Shehadeh, H. H. Aly and M. E. El-Hawary, "Photovoltaic inverters technology," in *Electrical and Computer Engineering (CCECE), 2015 IEEE 28th Canadian Conference On,* pp. 436-443. 2015.

[9] S. H. Shehadeh, H. H. Aly and M. E. El-Hawary, "Photovoltaic multi-level inverters technology," in *Electrical and Computer Engineering (CCECE), 2015 IEEE 28th Canadian Conference On,* pp. 648-655. 2015.

[10] S. H. Shehadeh, H. H. Aly and M. E. El-Hawary, "An overview of inverter topologies for photovoltaic electrical energy," in *Electrical Power & Energy Conference (EPEC), 2013 IEEE,* pp. 1-8. 2013.

[11] J. P. Benner and L. Kazmerski, "Photovoltaics: Gaining greater visibility," *IEEE Spectrum,* vol. 36, *(9),* pp. 34-42, 1999.

[12] European Renewable Energy Council, "Renewable Energy Scenario to 2040," European Renewable Energy Council: Brussels, Rep. 2012.

[13] J. M. Carrasco *et al*, "Power-electronic systems for the grid integration of renewable energy sources: A survey," *IEEE Transactions on Industrial Electronics,* vol. 53, *(4),* pp. 1002-1016, 2006.

[14] F. Blaabjerg, Z. Chen and B. K. Soeren, "Power electronics as efficient interface in dispersed power generation systems," *IEEE Transactions on Power Electronics,* vol. 19, *(5),* pp. 1184-1194, 2004.

[15] T. Bradford, *Solar revolution: The economic transformation of the global energy industry.* MIT Press, 2006.

[16] C. K. Ho *et al*, "Evaluation of glare at the Ivanpah Solar Electric Generating System," USDOE National Nuclear Security Administration (NNSA): United States, Rep. 2015.

[17] M. Y. Othman *et al*, "Performance analysis of PV/T Combi with water and air heating system: An experimental study," *Renewable Energy,* vol. 86, pp. 716-722, 2016.

[18] R. Tchinda, "Thermal behaviour of solar air heater with compound parabolic concentrator," *Energy Conversion and Management,* vol. 49, *(4),* pp. 529-540, 2008.

[19] R. P. Charles *et al*, "Assessment of concentrating solar power technology cost and performance forecasts," Rep. 2005.

[20] B. J. De Vries, D. P. Van Vuuren and M. M. Hoogwijk, "Renewable energy sources: Their global potential for the first-half of the 21st century at a global level: An integrated approach," *Energy Policy,* vol. 35, *(4),* pp. 2590-2610, 2007.

[21] REN21, "Renewables 2017 Global Status Report," REN21 Secretariat: Paris, Rep. 2017.

[22] F. Trieb *et al*, "Characterisation of solar electricity import corridors from MENA to Europe," German Aerospace Center (DLR), Institute of Technical Thermodynamics: Germany, Rep. 2009.

[23] G. Cramer, M. Ibrahim and W. Kleinkauf, "PV system technologies: State-of-the-art and trends in decentralised electrification," *Refocus,* vol. 5, *(1),* pp. 38-42, 2004.

[24] German Solar Energy Society, *Planning and installing photovoltaic systems: A guide for installers, architects and engineers.* 2nd ed. London, UK: Earthscan, 2008.

[25] R. A. Messenger and J. Ventre, *Photovoltaic systems engineering.* 2nd ed. Boca Raton, FL: CRC Press, 2003.

[26] EPIA, "Solar Generation 6: Solar photovoltaic electricity empowering the world," Rep. 1, February, 2011.

[27] D. LENARDIC, "Large-Scale Photovoltaic Power Plants: Cumulative and Annual Installed Power Output Capacity," *Annual Review,* 2008.

[28] N. A. Ahmed and M. Miyatake, "A stand-alone hybrid generation system combining solar photovoltaic and wind turbine with simple maximum power point tracking control," in *Power Electronics and Motion Control Conference, 2006. IPEMC 2006. CES/IEEE 5th International,* 2006.

[29] A. Campoccia *et al*, "Reliability analysis of a stand-alone PV system for the supply of a remote electric load," in *Int. Symp. on Power Electronics Elect. Drives Automation and Motion, (SPEEDAM),* Pisa, Italy, pp. 158-163. June 2010.

[30] R. W. Wies, R. A. Johnson and J. Aspnes, "Design of an energy-efficient standalone distributed generation system employing renewable energy sources and smart grid technology as a student design project," in *Power and Energy Society General Meeting, 2010 IEEE,* 2010.

[31] SolarWorld Americas, "Sunmodule for off-grid solutions," SolarWorld: Camarillo, Rep. 2011.

[32] R. Akkaya and A. A. Kulaksiz, "A microcontroller-based stand-alone photovoltaic power system for residential appliances," *Applied Energy,* vol. 78, *(4),* pp. 419-431, 2004.

[33] M. Muselli, G. Notton and A. Louche, "Design of hybrid-photovoltaic power generator, with optimization of energy management," *Solar Energy,* vol. 65, *(3),* pp. 143-157, 1999.

[34] Y. Chen, C. Cheng and H. Wu, "Grid-connected hybrid PV/wind power generation system with improved DC bus voltage regulation strategy," in *Applied Power Electronics Conference and Exposition, 2006. APEC'06. Twenty-First Annual IEEE,* 2006.

[35] S. Chiang, K. T. Chang and C. Y. Yen, "Residential photovoltaic energy storage system," *IEEE Transactions on Industrial Electronics,* vol. 45, *(3),* pp. 385-394, 1998.

[36] C. Hua and P. Ku, "Implementation of a stand-alone photovoltaic lighting system with MPPT, battery charger and high brightness LEDs," in *Power Electronics and Drives Systems, 2005. PEDS 2005. International Conference On,* 2005.

[37] A. Mohamed and T. Khatib, "Design of hybrid PV/diesel generator systems at minimum cost: Case study for kuching, malaysia," in *Transmission and Distribution Conference and Exposition (T&D), 2012 IEEE PES,* 2012.

[38] International Electrotechnical Commission, "Photovoltaic devices—Part 3: measurement principles for terrestrial photovoltaic (PV) solar devices with reference spectral irradiance data," *Iec 60904–3,* 1989.

[39] A. Ruiz, "System Aspects of Large Scale Implementation of a Photovoltaic Power Plant." , Royal Institute of Technology, Stockholm, Sweden, 2011.

[40] H. Felten, A. Kreutzmann and P. Welter, "Increase in grid-connected pv system power in germany," in *4th World Conf. on Photovoltaic Energy Conversion, (WCPEC-4),* Waikoloa, HI, pp. 2494-2496. May 2006.

[41] M. A. Eltawil and Z. Zhao, "Grid-connected photovoltaic power systems: Technical and potential problems—A review," *Renewable and Sustainable Energy Reviews,* vol. 14, *(1),* pp. 112-129, 2010.

[42] W. Omran, "Performance Analysis of Grid-Connected Photovoltaic Systems." , University of Waterloo, 2010.

[43] N. Mohan, T. M. Undeland and W. P. Robbins, *Power electronics: Converters, applications and design.* 3rd ed. John Wiley & Sons Australia, 2003.

[44] M. H. Rashid, *Power electronics handbook: Devices, circuits and applications.* Burlington: Academic press, 2010.

[45] A. Marinopoulos *et al*, "Grid integration aspects of large solar PV installations: LVRT capability and reactive power/voltage support requirements," in *PowerTech, 2011 IEEE Trondheim,* 2011.

[46] C. Nayar *et al*, "Power electronics for renewable energy sources," in *Alternative Energy in Power Electronics*, M. Rashid, Ed. Elsevier Inc., 2014, pp. 1-79.

[47] B. Van Zeghbroeck, *Principles of semiconductor devices and heterojunctions.* Prentice Hall PTR, 2007.

[48] F. A. Lindholm, J. G. Fossum and E. L. Burgess, "Application of the superposition principle to solar-cell analysis," *IEEE Transactions on Electron Devices,* vol. 26, *(3),* pp. 165-171, 1979.

[49] D. Mehmet, "Design and Implementation of PLC Controlled Solar Tracking System," *Technological Applied Sciences,* vol. 4, *(3),* pp. 315-329, 2009.

[50] M. A. Green, *Solar cells: Operating principles, technology, and system applications.* Prentice-Hall, 1982.

[51] N. E. Anku *et al*, "A model for photovoltaic module optimisation," *Journal of Mechanical Engineering and Automation,* vol. 5, *(2),* pp. 72-79, 2015.

[52] M. K. El-Adawi and I. A. Al-Nuaim, "A method to determine the solar cell series resistance from a single I–V. Characteristic curve considering its shunt resistance—new approach," *Vacuum,* vol. 64, *(1),* pp. 33-36, 2001.

[53] M. R. Patel, *Wind and solar power systems: Design, analysis, and operation.* 2nd ed. CRC press, 2006.

[54] W. Jewell and R. Ramakumar, "The effects of moving clouds on electric utilities with dispersed photovoltaic generation," *IEEE Transactions on Energy Conversion, (4),* pp. 570-576, 1987.

[55] T. Ehara, "Overcoming PV grid issues in urban areas," *IEA PVPS Task,* vol. 10, 2009.

[56] G. Chicco, J. Schlabbach and F. Spertino, "Performance of grid-connected photovoltaic systems in fixed and sun-tracking configurations," in *Power Tech, 2007 IEEE Lausanne,* 2007.

[57] D. G. Holmes and T. Lipo, *Pulse width modulation for power converters: Principles and practice.* Wiley-IEEE Press, 2003.

[58] M. Liserre, F. Blaabjerg and S. Hansen, "Design and control of an LCL-filter based three-phase active rectifier," in *Industry Applications Conference, 2001. Thirty-Sixth IAS Annual Meeting. Conference Record of the 2001 IEEE,* 2001.

[59] F. Blaabjerg *et al*, "Analysis of the grid side behavior of a LCL-filter based three-phase active rectifier," in *Industrial Electronics, 2003. ISIE'03. 2003 IEEE International Symposium On,* 2003.

[60] T. C. Wang *et al*, "Output filter design for a grid-interconnected three-phase inverter," in *Power Electronics Specialist Conference, 2003. PESC'03. 2003 IEEE 34th Annual,* 2003.

[61] P. Fairley, "BP solar ditches thin-film photovoltaics," *IEEE Spectrum,* vol. 40, *(1),* pp. 18-19, 2003.

[62] PV EnergyTrend*, PV Spot Price*, 2017. [Online]. Available: http://pv.energytrend.com/pricequotes.html.

[63] J. Yazdanpanahi, F. Sarhaddi and M. M. Adeli, "Experimental investigation of exergy efficiency of a solar photovoltaic thermal (PVT) water collector based on exergy losses," *Solar Energy,* vol. 118, pp. 197-208, 2015.

[64] R. Tripathi, G. N. Tiwari and I. M. Al-Helal, "Thermal modelling of N partially covered photovoltaic thermal (PVT)–Compound parabolic concentrator (CPC) collectors connected in series," *Solar Energy,* vol. 123, pp. 174-184, 2016.

[65] S. Dubey and G. N. Tiwari, "Thermal modeling of a combined system of photovoltaic thermal (PV/T) solar water heater," *Solar Energy,* vol. 82, *(7),* pp. 602-612, 2008.

[66] S. Dubey and G. N. Tiwari, "Analysis of PV/T flat plate water collectors connected in series," *Solar Energy,* vol. 83, *(9),* pp. 1485-1498, 2009.

[67] T. T. Chow *et al*, "Energy and exergy analysis of photovoltaic–thermal collector with and without glass cover," *Applied Energy,* vol. 86, *(3),* pp. 310-316, 2009.

[68] G. N. Tiwari and S. Dubey, *Fundamentals of photovoltaic modules and their applications.* 1st ed. Royal Society of Chemistry, 2009.

[69] A. Al Tarabsheh *et al*, "Performance of photovoltaic cells in photovoltaic thermal (PVT) modules," *IET Renewable Power Generation,* vol. 10, *(7),* pp. 1017-1023, 2016.

[70] M. G. Villalva, J. R. Gazoli and E. Ruppert Filho, "Comprehensive approach to modeling and simulation of photovoltaic arrays," *IEEE Transactions on Power Electronics,* vol. 24, *(5),* pp. 1198-1208, 2009.

[71] Solarex, "MSX-60 and MSX-64 Photovoltaic Modules," datasheet, 1998.

[72] X. Zhang *et al*, "Socio-economic performance of a novel solar photovoltaic/loop-heat-pipe heat pump water heating system in three different climatic regions," *Applied Energy,* vol. 135, pp. 20-34, 2014.

[73] J. J. Michael, S. Iniyan and R. Goic, "Flat plate solar photovoltaic–thermal (PV/T) systems: a reference guide," *Renewable and Sustainable Energy Reviews,* vol. 51, pp. 62-88, 2015.

[74] A. D. Jones and C. P. Underwood, "A thermal model for photovoltaic systems," *Solar Energy,* vol. 70, *(4),* pp. 349-359, 2001.

[75] T. T. Chow, W. He and J. Ji, "Hybrid photovoltaic-thermosyphon water heating system for residential application," *Solar Energy,* vol. 80, *(3),* pp. 298-306, 2006.

[76] G. N. Tiwari, R. K. Mishra and S. C. Solanki, "Photovoltaic modules and their applications: a review on thermal modelling," *Applied Energy,* vol. 88, *(7),* pp. 2287-2304, 2011.

[77] G. N. Tiwari and I. M. Al-Helal, "Analytical expression of temperature dependent electrical efficiency of N-PVT water collectors connected in series," *Solar Energy,* vol. 114, pp. 61-76, 2015.

[78] S. Agrawal and G. N. Tiwari, "Energy and exergy analysis of hybrid micro-channel photovoltaic thermal module," *Solar Energy,* vol. 85, *(2),* pp. 356-370, 2011.

[79] S. Agrawal and G. N. Tiwari, "Overall energy, exergy and carbon credit analysis by different type of hybrid photovoltaic thermal air collectors," *Energy Conversion and Management,* vol. 65, pp. 628-636, 2013.

[80] R. Tripathi, G. N. Tiwari and V. K. Dwivedi, "Overall energy, exergy and carbon credit analysis of N partially covered photovoltaic thermal (PVT) concentrating collector connected in series," *Solar Energy,* vol. 136, pp. 260-267, 2016.

[81] Canadian Weather Energy*, Engineering Data Sets (CWEEDS); CWEC Weather Files*. [Online]. Available: http://open.canada.ca/data/en/dataset/2b9bc161-ca00-4a1e-9c75-58ed621ef4b1.

[82] EURELECTRIC "Preservation of Resources" Working Group's and "Upstream" Sub-Group in collaboration with, VGB, "Efficiency in Electricity Generation " Rep. July, 2003.

[83] Commission for Environmental Cooperation, "North American POWER PLANT Air Emissions," Rep. 2011.

[84] A. Moreno-Munoz *et al*, "Very short term forecasting of solar radiation," in *Photovoltaic Specialists Conference, 2008. PVSC'08. 33rd IEEE,* 2008.

[85] D. Anderson and M. Leach, "Harvesting and redistributing renewable energy: on the role of gas and electricity grids to overcome intermittency through the generation and storage of hydrogen," *Energy Policy,* vol. 32, *(14),* pp. 1603-1614, 2004.

[86] C. Voyant *et al*, "Twenty four hours ahead global irradiation forecasting using multi-layer perceptron," *Meteorological Applications,* vol. 1, Mar., 2013.

[87] A. Mellit *et al*, "Artificial intelligence techniques for sizing photovoltaic systems: A review," *Renewable and Sustainable Energy Reviews,* vol. 13, *(2),* pp. 406-419, 2009.

[88] B. Espinar *et al*, "Photovoltaic forecasting: A state of the art," in *5th European PV-Hybrid and Mini-Grid Conference,* 2010.

[89] V. Lara-Fanego *et al*, "Evaluation of the WRF model solar irradiance forecasts in Andalusia (southern Spain)," *Solar Energy,* vol. 86, *(8),* pp. 2200-2217, 2012.

[90] S. K. Aggarwal and L. M. Saini, "Solar energy prediction using linear and non-linear regularization models: a study on AMS (American Meteorological Society) 2013–14 solar energy prediction contest," *Energy,* vol. 78, pp. 247-256, 2014.

[91] S. A. Kalogirou, "Artificial neural networks in renewable energy systems applications: a review," *Renewable and Sustainable Energy Reviews,* vol. 5, *(4),* pp. 373-401, 2001.

[92] C. Voyant *et al*, "Machine learning methods for solar radiation forecasting: A review," *Renewable Energy,* vol. 105, pp. 569-582, 2017.

[93] J. M. Zurada, *Introduction to artificial neural networks.* St. Paul: West Publishing Company, 1992.

[94] A. K. Jain, J. Mao and K. M. Mohiuddin, "Artificial neural networks: A tutorial," *IEEE Computer,* vol. 29, *(3),* pp. 31-44, 1996.

[95] Q. Zhang and A. Benveniste, "Wavelet networks," *IEEE Transactions on Neural Networks,* vol. 3, *(6),* pp. 889-898, 1992.

[96] J. Moody and C. J. Darken, "Fast learning in networks of locally-tuned processing units," *Neural Computation,* vol. 1, *(2),* pp. 281-294, 1989.

[97] Z. Zainuddin and O. Pauline, "Improved wavelet neural networks for early cancer diagnosis using clustering algorithms," *International Journal of Information and Mathematics Sciences,* vol. 6, *(1),* pp. 30-36, 2010.

[98] Z. Zainuddin and P. Ong, "An effective and novel wavelet neural network approach in classifying type 2 diabetics," *Neural Network World,* vol. 22, *(5),* pp. 407, 2012.

[99] J. Mubiru and Banda, E J K B, "Estimation of monthly average daily global solar irradiation using artificial neural networks," *Solar Energy,* vol. 82, *(2),* pp. 181-187, 2008.

[100] K. Moustris *et al*, "Use of neural networks for the creation of hourly global and diffuse solar irradiance data at representative locations in Greece," *Renewable Energy,* vol. 33, *(5),* pp. 928-932, 2008.

[101] S. Alam, S. C. Kaushik and S. N. Garg, "Assessment of diffuse solar energy under general sky condition using artificial neural network," *Applied Energy,* vol. 86, *(4),* pp. 554-564, 2009.

[102] A. Mellit and A. M. Pavan, "A 24-h forecast of solar irradiance using artificial neural network: Application for performance prediction of a grid-connected PV plant at Trieste, Italy," *Solar Energy,* vol. 84, *(5),* pp. 807-821, May., 2010.

[103] Fangping Deng *et al*, "Global solar radiation modeling using the artificial neural network technique," in *Asia-Pacific Power and Energy Eng. Conf. (APPEEC),* pp. 1-5. 2010.

[104] Z. Wang, F. Wang and S. Su, "Solar Irradiance Short-Term Prediction Model Based on BP Neural Network," *Energy Procedia,* vol. 12, pp. 488-494, 2011.

[105] A. Karoro, T. Ssenyonga and J. Mubiru, "Predicting Global Solar Radiation Using an Artificial Neural Network Single-Parameter Model," *Advances in Artificial Neural Syst.,* vol. 2011, pp. 1-7, 2011.

[106] K. D. Rao, B. I. Rani and G. S. Ilango, "Estimation of daily global solar radiation using temperature, relative humidity and seasons with ANN for indian stations," in *Int. Conf. on Power, Signals, Controls and Computation (EPSCICON),* pp. 1-6. 2012.

[107] A. Hasni *et al*, "Estimating global solar radiation using artificial neural network and climate data in the south-western region of Algeria," *Energy Procedia,* vol. 18, pp. 531-537, 2012.

[108] M. Alharbi, "Daily Global Solar Radiation Forecasting using ANN and Extreme Learning Machine: A Case Study in Saudi Arabia." , Elect. and Computer Eng., Dalhousie Univ., Halifax, NS, 2013.

[109] B. M. Alluhaidah, S. H. Shehadeh and M. E. El-Hawary, "Most influential variables for solar radiation forecasting using artificial neural networks," in *Electrical Power and Energy Conference (EPEC), 2014 IEEE,* 2014.

[110] M. Shaddel, D. S. Javan and P. Baghernia, "Estimation of hourly global solar irradiation on tilted absorbers from horizontal one using artificial neural network for case study of Mashhad," *Renewable and Sustainable Energy Reviews,* vol. 53, pp. 59-67, 2016.

[111] M. Laidi *et al*, "Supervised artificial neural network-based method for conversion of solar radiation data (case study: Algeria)," *Theoretical and Applied Climatology,* vol. 128, *(1-2),* pp. 439-451, 2017.

[112] M. Vakili *et al*, "Evaluating the effect of particulate matter pollution on estimation of daily global solar radiation using artificial neural network modeling based on meteorological data," *Journal of Cleaner Production,* vol. 141, pp. 1275-1285, 2017.

[113] H. Loutfi, A. Bernatchou and R. Tadili, "Generation of Horizontal Hourly Global Solar Radiation from Exogenous Variables Using an Artificial Neural Network in Fes (Morocco)," *International Journal of Renewable Energy Research (IJRER),* vol. 7, *(3),* pp. 1097-1107, 2017.

[114] H. B. Yıldırım *et al*, "Estimating daily Global solar radiation with graphical user interface in Eastern Mediterranean region of Turkey," *Renewable and Sustainable Energy Reviews,* 2017.

[115] L. Cividino, "Power factor, harmonic distortion; causes, effects and considerations," in *Telecommunications Energy Conference, 1992. INTELEC'92., 14th International,* 1992.

[116] F. De la Rosa, *Harmonics and power systems.* CRC press Boca Raton, 2006.

[117] W. M. Grady and R. J. Gilleskie, "Harmonics and how they relate to power factor," in *EPRI Proceeding of the Power Quality Issues & Oppertunities Conference,* 1993.

[118] E. Vasanasong and E. D. Spooner, "The prediction of net harmonic currents produced by large numbers of residential PV inverters: Sydney olympic village case study," in pp. 116-121. 2000.

[119] J. Arrillaga and N. R. Watson, *Power system harmonics.* John Wiley & Sons, 2004.

[120] M. PatsalidesA. StavrouG. MakridesV. Efthimiou and G. E. Georghiou*, Harmonic Response of Distributed Grid Connected PhotoVotaic Systems*, 2008. [Online]. Available: http:/www.pvtechnology.ucy.ac/pvtechnology/publication/DEMSEE08_pq.paper.pdf.

[121] F. Zare and G. Ledwich, "A new predictive current control technique for multilevel converters," in *Tencon.2006,* pp. 1-4. December 2006.

[122] S. B. Kjaer, J. K. Pedersen and F. Blaabjerg, "A review of single-phase grid-connected inverters for photovoltaic modules," *IEEE Transactions on Industry Applications,* vol. 41, *(5),* pp. 1292-1306, 2005.

[123] G. Buticchi *et al*, "A nine-level grid-connected converter topology for single-phase transformerless PV systems," *IEEE Transactions on Industrial Electronics,* vol. 61, *(8),* pp. 3951-3960, 2014.

[124] J. C. Wu and C. W. Chou, "A Solar Power Generation System with a Seven-Level Inverter," *IEEE Transactions on Power Electronics,* vol. 29, *(7),* pp. 3454-3462, 2014.

[125] Y. Tang, X. Dong and Y. He, "Active buck–boost inverter," *IEEE Transactions on Industrial Electronics,* vol. 61, *(9),* pp. 4691-4697, 2014.

[126] R. S. Alan, *Fundamentals of power electronics with matlab.* Boston: Laxmi Publications, 2007.

[127] J. Liu, K. Cheng and Y. Ye, "A cascaded multilevel inverter based on switched-capacitor for high-frequency AC power distribution system," *IEEE Transactions on Power Electronics,* vol. 29, *(8),* pp. 4219-4230, 2014.

[128] D. Iero *et al*, "SPICE modelling of a complete photovoltaic system including modules, energy storage elements and a multilevel inverter," *Solar Energy,* vol. 107, pp. 338-350, 2014.

[129] K. Ishaque and Z. Salam, "An improved modeling method to determine the model parameters of photovoltaic (PV) modules using differential evolution (DE)," *Solar Energy,* vol. 85, *(9),* pp. 2349-2359, 2011.

[130] Y. M. Roshan and M. Moallem, "Maximum power point estimation and tracking using power converter input resistance control," *Solar Energy,* vol. 96, pp. 177-186, 2013.

[131] D. C. McKay and R. J. Morris, *Solar radiation data analyses for canada, 1967-1976.* Canadian Climate Program, 1985.

[132] L. Cristaldi *et al*, "An improved model-based maximum power point tracker for photovoltaic panels," *IEEE Transactions on Instrumentation and Measurement,* vol. 63, *(1),* pp. 63-71, 2014.

[133] S. Lineykin, M. Averbukh and A. Kuperman, "An improved approach to extract the single-diode equivalent circuit parameters of a photovoltaic cell/panel," *Renewable and Sustainable Energy Reviews,* vol. 30, pp. 282-289, 2014.

[134] S. Munir and Y. W. Li, "Residential distribution system harmonic compensation using PV interfacing inverter," *IEEE Transactions on Smart Grid,* vol. 4, *(2),* pp. 816-827, 2013.

[135] C. Sintamarean *et al*, "Real field mission profile oriented design of a SiC-based PV-inverter application," in *Energy Conversion Congress and Exposition (ECCE), 2013 IEEE,* 2013.

[136] M. H. Rashid, *Power electronics: Circuits, devices, and applications.* 4th ed. Pearson Education, 2014.

[137] M. Evan *et al*, *Statistical distributions.* 4th ed. Wiley, 2010.

[138] R. Nandhakumar and S. Jeevananthan, "Inverted sine carrier pulse width modulation for fundamental fortification in DC-AC converters," in *Power Electronics and Drive Systems, 2007. PEDS'07. 7th International Conference On,* 2007.

[139] M. Hagiwara and H. Akagi, "Control and experiment of pulsewidth-modulated modular multilevel converters," *IEEE Transactions on Power Electronics,* vol. 24, *(7),* pp. 1737-1746, 2009.

[140] A. Molderink *et al*, "Domestic energy management methodology for optimizing efficiency in smart grids," in *PowerTech, 2009 IEEE Bucharest,* 2009.

[141] United States Department of Energy, 2003, "The Micro-CHP Technologies Roadmap," Proceedings of the 21th Century Residential Energy Needs Meeting: Rep. 2003.

[142] S. Kaluđer, D. Šljivac and S. Miletić, "The optimal placement of distributed generation," *Tehnicki Vjesnik-Technical Gazette,* vol. 3, *(19),* pp. 535-541, 2012.

[143] Z. Klaić, K. Fekete and D. Šljivac, "Demand side management in the distribution system with photovoltaic generation," *Tehnički Vjesnik,* vol. 22, *(4),* pp. 989-995, 2015.

[144] C. W. Gellings, *The smart grid: Enabling energy efficiency and demand response.* The Fairmont Press, Inc., 2009.

[145] "Sensor Monitoring Device,"T. Paraskevakos, 3,842,208T. Paraskevakos, "Sensor Monitoring Device," 3,842,208, 1974.

[146] "Remote Management of Products and Services,"T. G. Paraskevakos and P. Kastrinakis, 4,241,237, 4,455,453 and 7,940,901T. G. Paraskevakos and P. Kastrinakis, "Remote Management of Products and Services," 4,241,237, 4,455,453 and 7,940,901, 2011.

[147] Florida Power & Light Company*, FPL Files Proposal to Enhance Energy Conservation Programs; Customers To Directly Benefit and Save More Money Through Higher Incentives and New Programs*, 2006. [Online]. Available: http://www.businesswire.com/news/home/20060523005791/en/FPL-Files-Proposal-Enhance-Energy-Conservation-Programs.

[148] J. Khoury *et al*, "Predictive demand side management of a residential house under intermittent primary energy source conditions," *Energy and Buildings,* vol. 112, pp. 110-120, 2016.

[149] S. Janocha, S. Baum and I. Stadler, "Cost minimization by optimization of electricity generation and demand side management," in *Energy and Sustainability Conference (IESC), 2016 International,* 2016.

[150] A. Arteconi *et al*, "Thermal energy storage coupled with PV panels for demand side management of industrial building cooling loads," *Applied Energy,* vol. 185, pp. 1984-1993, 2017.

[151] D. Parra *et al*, "Optimum community energy storage for renewable energy and demand load management," *Applied Energy,* vol. 200, pp. 358-369, 2017.

[152] Thermo Dynamics Ltd Company, "Solar Water Heating System," Rep. 2013.

[153] Thermo Dynamics Ltd Company, "Web Energy Logger," Rep. 2013.

[154] World Weather Online*, HALIFAX WEATHER FORECAST*, 2017. [Online]. Available: https://www.worldweatheronline.com/halifax-weather/nova-scotia/ca.aspx.

[155] K. Sukhatme and S. P. Sukhatme, *Solar energy: Principles of thermal collection and storage.* Tata McGraw-Hill Education, 1996.

[156] Alliance for Water Efficiency, *Clothes Washer*, 2017. [Online]. Available: https://www.home-water-works.org/indoor-use/clothes-washer.

[157] The Spruce, *Laundry and Water Temperature*. [Online]. Available: https://www.washlaundry.com/residents/laundry-tips/temperature/.

[158] A. Shukla, D. Buddhi and R. L. Sawhney, "Solar water heaters with phase change material thermal energy storage medium: a review," *Renewable and Sustainable Energy Reviews,* vol. 13, *(8),* pp. 2119-2125, 2009.

[159] 2017 Alliance for Water Efficiency and NFP, *Dish Washer*. [Online]. Available: https://www.home-water-works.org/indoor-use/dishwasher.

[160] Bosch, *Which Wash Cycle Should I Use?*, 2012. [Online]. Available: https://free-info-pages.com/bosch-300-series-dishwasher/miscellaneous-faq/which-wash-cycle-should-i-use.html.

[161] 2017 Alliance for Water Efficiency, *Shower*. [Online]. Available: https://www.home-water-works.org/indoor-use/showers.

APPENDIX

Copyright Permission

On We, Nov 8, 2017 at 10:16 AM, Krista Thom <k.thom@ieee.org> wrote:

Dear Mr. Shehadeh,

Thank you for reaching out to us. **The IEEE does not require individuals working on a thesis to obtain a formal reuse license** however, you must follow the requirements listed below:

November 8, 2017 10:16 AM

Textual Material

Using short quotes or referring to the work within these papers, users must give full credit to the original source (author, paper, publication) followed by the IEEE copyright line © **[Year of publication] IEEE**.

In the case of illustrations or tabular material, we require that the copyright line © **[Year of original publication] IEEE** appear prominently with each reprinted figure and/or table.

If a substantial portion of the original paper is to be used, and if you are not the senior author, you must also obtain the senior author's approval.

Full-Text Article

If you are using the entire IEEE copyright owned article, the following IEEE copyright/credit notice should be placed prominently in the references: © **[year of original publication] IEEE. Reprinted, with permission, from [author names, paper title, IEEE publication title, and month/year of publication]**

Only the **accepted** version of an IEEE copyrighted paper can be used when posting the paper or your thesis on-line. **You may not use the final published version.**

In placing the thesis on the author's university website, please display the following message in a prominent place on the website: **In reference to IEEE copyrighted material which is used with permission in this thesis, the IEEE does not endorse any of [university/educational entity's name goes here]'s products or services. Internal or personal use of this material is permitted. If interested in reprinting/republishing IEEE copyrighted material for advertising or promotional purposes or for creating new collective works for resale or redistribution, please go to**

http://www.ieee.org/publications_standards/publications/rights/rights_link.html

to learn how to obtain a License from Rights Link.

If applicable, University Microfilms and/or ProQuest Library, or the Archives of Canada may supply single copies of the dissertation.

Good luck on your thesis!

Cheers,

Krista

On Tue, Nov 7, 2017 at 10:47 PM, shadi shehadeh <sh790078@dal.ca> wrote:

Dear Sir/Madam

I am the first author of the following papers, while I was working toward my PhD. degree. Now, I am preparing my PhD. thesis for submission to the Faculty of Graduate Studies at Dalhousie University, Halifax, Nova Scotia, Canada.

I am seeking your permission to include a manuscript version of the following papers in the thesis:

S.H. Shehadeh, H. H. Aly and M. E. El-Hawary, "Minimizing CO_2e emissions of Photovoltaic Thermal model in North America", *30th annual IEEE Canadian Conference on Electrical and Computer Engineering (CCECE'2017), Windsor, Canada, May 3, 2017.*

S.H. Shehadeh, H. H. Aly and M. E. El-Hawary, "PV Harmonic Distribution Analysis for Various Conditions", *29th annual IEEE Canadian Conference on Electrical and Computer Engineering (CCECE'2016), Vancouver, Canada, May15, 2016.*

S.H. Shehadeh, H. H. Aly and M. E. El-Hawary, "Photovoltaic Multi-Level Inverter Technology", *28th annual IEEE Canadian Conference on Electrical and Computer Engineering (CCECE'2015), Halifax, Canada, May 3, 2015.*

S.H. Shehadeh, H. H. Aly and M. E. El-Hawary, "Photovoltaic Inverter Technology", *28th annual IEEE Canadian Conference on Electrical and Computer Engineering (CCECE'2015), Halifax, Canada, May 3, 2015.*

S.H. Shehadeh, H. H. Aly and M. E. El-Hawary, "An overview of inverter topologies for photovoltaic electrical energy", *Electrical Power and Energy Conference (EPEC), Halifax, Canada, Aug 21, 2013.*

Full publication details and a copy of this permission letter will be included in the thesis.

Best Regards,

Shadi H. Shehadeh